POLITECNICO
MILANO 1863

SCUOLA DI INGEGNERIA INDUSTRIALE
E DELL'INFORMAZIONE

Synthesis and Characterization of Zinc Manganite Thin Films for Zinc-Ion Battery Applications

Tesi di Laurea Magistrale in
Nuclear Engineering - Ingegneria Nucleare

Author: **Marco Olivieri**

Student ID: 928175
Advisor: Prof. Andrea Li Bassi
Co-advisors: Dr. Andrea Macrelli
Academic Year: 2021-22

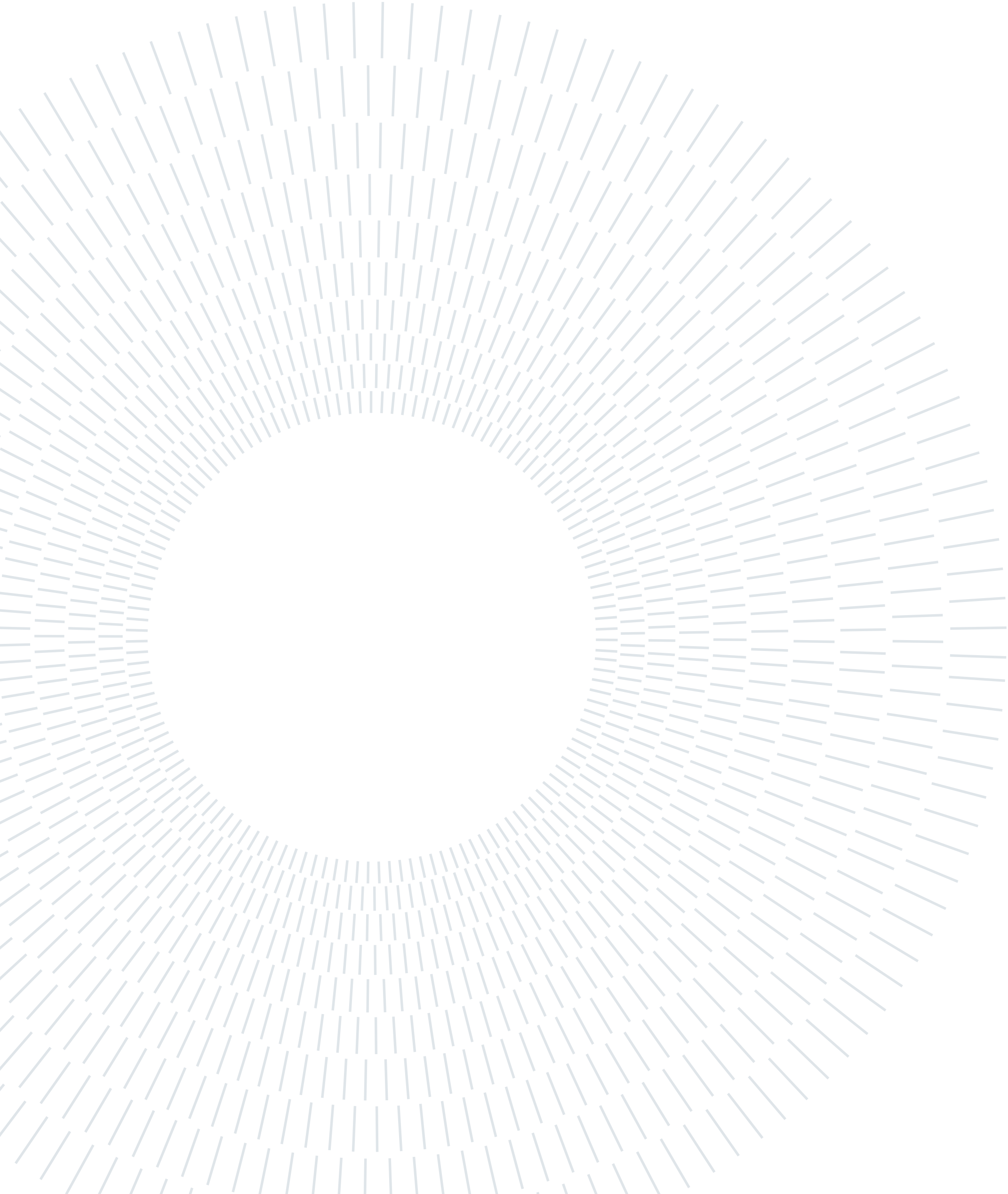

Abstract

Batteries are, and will increasingly be, an essential technology. Society wants to progress toward an increasingly sustainable future, and this drives the battery market; on the other hand, it also requires batteries to be more sustainable, safe, and disposed of in an environmentally friendly manner. Current lithium-ion batteries are struggling to keep up with these demands. One of the developing fronts is the zinc-ion battery, which can implement non-organic, and non-flammable aqueous electrolytes that are more easily managed during disposal. In addition, zinc-ion batteries can also avoid employing cobalt, which is rare, expensive, and toxic to humans and to the environment, and can directly rely on Zn metal as the anode. One of the challenges in bringing such batteries to adequate performance is the cathode design. Common cathode materials are Mn and V oxides, metal vanadates, and Prussian blue analogues; another possible cathode candidate is spinel $ZnMn_2O_4$ (ZMO). ZMO is composed of common and abundant elements in the Earth's crust: zinc and manganese. While the bulk material does not seem to show sufficient electrochemical performance, if properly prepared (by acting on its composition and morphology at the nanoscale), ZMO becomes a good cathode candidate for zinc-ion batteries. Although there are several studies on the material in the literature, its main electrochemical mechanisms are still not fully understood.

In my work, thin films of ZMO were produced by Pulsed Laser Deposition (PLD). Deposition conditions were optimized in vacuum and oxygen atmospheres at different pressures (1-150 Pa). Samples were characterized after deposition by Scanning Electron Microscopy (SEM) to evaluate their morphology, and by Energy Dispersive X-Ray Spectroscopy (EDXS) for initial stoichiometric analyses. At high oxygen pressures (100 and 150 Pa), low-density porous films formed by forest-like nanostructures were obtained. It was also determined using Raman spectroscopy that the as-deposited films are amorphous. To achieve crystallization of the material, annealing was performed on the samples. The lower temperature limits (500°C) for crystallization of the material in air and vacuum were identified. Raman spectroscopy was employed to evaluate the crystallization of the ZMO films to the expected spinel phase by comparing the acquired spectra with those reported in the literature. I also studied how different annealing temperatures in air affect the morphology and the Raman spectrum of the sample, concluding that a higher annealing temperature increases the crystal grain size and improves the crystalline quality. In my work, I present an extensive discussion about how oxygen deposition pressure affects the annealed samples. I verified by Raman spectroscopy that crystallized samples deposited in vacuum or at 1 Pa of oxygen have Raman spectra with distinct differences from those of films deposited at higher oxygen pressures. The morphology of the films was analysed and compared before and after annealing, showing how porosity tends to increase and ZMO nanocrystals form after heat treatment. Samples deposited at high oxygen pressures (100-150 Pa) maintain the nanostructured crystalline forest, which is a favorable condition for the electrochemistry of ZMO. Finally, some optical measurements were conducted on ZMO films deposited at different oxygen pressures on glass substrates. The last part of the experimentation focused on preliminary electrochemical tests on the crystallized ZMO films deposited at different oxygen pressures (1 Pa, 50 Pa, and 100 Pa) on FTO-coated glass substrates. The electrochemical tests have proved promising as not only did they show the expected electrochemical activity but the films remained intact during the treatments. Specifically, cyclic voltammetry (CV) was performed on the samples in the range of -0.75 V to +0.75 V vs. Pt-QRef. in an aqueous electrolyte consisting of $ZnSO_44$ 2 M + $MnSO_4$ 0.1 M (ZMS electrolyte). CVs were different for each sample, thus demonstrating the effect of film morphology and surface area on electrochemical performances. In order to identify the possible electrochemical mechanisms, some potentiostatic (PS) measurements were performed, in ZMS electrolyte, on the sample deposited at 100 Pa of oxygen, followed by Raman and SEM investigation. The main result was the pronounced reduction of the Raman peaks associated with ZMO. I ascribed the reason for this reduction and reactivation of the ZMO-attributed peaks to three simultaneous mechanisms: 1) the intercalation/deintercalation of zinc/protons from ZMO; 2) the dissolution and electrodeposition of MnO_2; 3) the intercalation of zinc in the electrodeposited MnO_2.

Concluding, PLD has proven to be a suitable method for the production of ZMO films both for the characterization of the material itself and for electrochemical developments and research. Research on these films requires further investigation on both fronts mentioned. Future developments of this research may focus on the characterization of the material with complementary techniques (XRD, XPS, XAS) and the production of films using different deposition parameters, or on the electrochemical side where only preliminary tests have been completed.

Keywords: ZMO, $ZnMn_2O_4$, Zinc-ion batteries, Raman spectroscopy, PLD, Thin-films

Abstract in lingua italiana

Le batterie sono, e saranno sempre di più, una tecnologia essenziale. La società vuole avanzare verso un futuro sempre più sostenibile, e ciò da un lato traina il mercato delle batterie, dall'altro richiede anche a queste ultime una maggiore sostenibilità, sicurezza e uno smaltimento a basso impianto ambientale. Le attuali batterie agli ioni di litio faticano a tenere il passo con queste richieste. Uno dei fronti in sviluppo sono le batterie agli ioni di zinco, che possono implementare elettroliti non organici, non infiammabili, più facilmente gestibili durante lo smaltimento. Inoltre, le batterie allo zinco possono anche evitare l'impiego di cobalto, che è raro, costoso e tossico per l'uomo e l'ambiente. Una delle sfide nel portare tali batterie a performance adeguate è la progettazione del catodo. Uno dei possibili materiali per questa componente delle batterie agli ioni di zinco è lo $ZnMn_{2]O_4}$ (ZMO). Lo ZMO è composto da elementi comuni e abbondanti nella crosta terrestre: lo zinco e il manganese. Sebbene il materiale compatto allo stato puro non sembri mostrare prestazioni elettrochimiche sufficienti, se propriamente preparato, andando ad agire sulla sua composizione e sulla morfologia a livello nanostrutturale, lo ZMO diventa un buon candidato come catodo per le batterie agli ioni di zinco. Nonostante siano presenti in letteratura diversi studi sul materiale, ancora non si sono compresi appieno i suoi meccanismi elettrochimici principali.

Nel mio lavoro sono stati prodotti film sottili di ZMO tramite l'uso della Pulsed Laser Deposition (PLD). Sono state ottimizzate le condizioni di deposizione in vuoto e atmosfere di ossigeno a diverse pressioni (1-150 Pa). I campioni sono stati caratterizzati dopo la deposizione mediante lo Scanning Electron Microscope (SEM) per valutarne la morfologia, e con la Energy Dispersive X-ray Spectroscopy (EDXS) per le prime analisi stechiometriche. A pressioni di ossigeno elevate (100 e 150 Pa) si ottengono film porosi con nanostrutture a foresta. Si è determinato inoltre, usando la spettroscopia Raman, che i film depositati sono amorfi. Per ottenere la cristallizzazione del materiale sono stati eseguiti trattamenti termici (annealing) sui campioni. Sono stati identificati i limiti inferiori di temperatura (500°C) per la cristallizzazione del materiale in aria e in vuoto. La spettroscopia Raman è stata utilizzata per valutare la cristallizzazione del film di ZMO, comparando gli spettri acquisiti con quelli riportati in letteratura. Si è inoltre studiato come diverse temperature di annealing in aria modifichino la morfologia e lo spettro Raman del campione, concludendo che una temperatura di annealing maggiore aumenta le dimensioni della grana cristallina. Nel mio lavoro presento una trattazione estensiva di come la pressione di deposizione di ossigeno influenzi i campioni trattati termicamente. Si è verificato tramite spettroscopia Raman che i campioni, dopo la ricottura, depositati in vuoto o a 1 Pa di ossigeno hanno degli spettri Raman con differenze marcate rispetto a quelli dei film depositati a più alte pressioni di ossigeno. La morfologia dei film è stata analizzata e comparata prima e dopo l'annealing, mostrando come la porosità tenda ad aumentare e si formino nanocristalli di ZMO dopo il trattamento termico. I campioni depositati ad alte pressioni di ossigeno (100-150 Pa) mantengono la nanostruttuta a foresta cristallina, che è una condizione favorevole per l'elettrochimica dello ZMO. Infine, alcune misure ottiche sono state effettuate su film cristallizzati di ZMO depositati a diverse pressioni di ossigeno su substrati di vetro. L'ultima parte della sperimentazione sono stati i primi test elettrochimici sui film cristallizzati depositati a diverse pressioni di ossigeno (1 Pa, 50 Pa e 100 Pa) su substrato di vetro coperto da FTO. I test elettrochimici si sono dimostrati promettenti, in quanto, non solo hanno mostrato l'attività elettrochimica aspettata, ma i film si sono mantenuti intatti durante i trattamenti. In particolare, le ciclovoltammetrie (CV) sono state eseguite sui campioni con range da -0.75 V a +0.75 V vs. Pt-QRefe e velocità di scansione pari a 20 mV/s per 8 cicli. Le CV sono state condotte in una cella con elettrolita acquoso con disciolti $ZnSO_4$ 2 M + $MnSO_4$ 0.1 M (elettrolita ZMS). Le CV sono risultate diverse per ogni campione. Al fine di individuare i possibili meccanismi elettrochimici dei film, sono state eseguite alcune misure potenziostatiche (PS), con elettrolita ZMS, sul campione depositato a 100 Pa di ossigeno. Dopo ogni misura PS ho misurato lo spettro Raman del campione elettrochimicamente trattato. Il risultato principale è stata la riduzione evidente dei picchi Raman associati allo ZMO. La ragione di tale riduzione e riattivazione dei picchi attribuiti allo ZMO è stata associata a tre meccanismi simultanei: 1) la intercalazione/deintercalazione dello zinco dallo ZMO, 2) la dissoluzione ed elettrodeposizione di MnO_2, 3) la intercalazione di zinco nel MnO_2 elettrodeposiato. Concludendo, la PLD si è rivelata un metodo adeguato alla produzione di film di ZMO sia per la caratterizzazione del materiale in sé, sia ai fini di sviluppi e ricerca elettrochimica. La ricerca su questi film richiede ulteriori indagini su entrambi i fronti menzionati. Futuri sviluppi di questa ricerca possono vertere sulla caratterizzazione del materiale e la produzione di film usando diversi parametri di deposizione, oppure sulla parte elettrochimica dove solo i test preliminari sono stati effettuati.

Parole chiave: ZMO, $ZnMn_2O_4$, Batterie agli ioni di zinco, Spettroscopia Raman, PLD, Film sottili

Contents

Introduction

The interest in energy storage systems has been growing. Energy needs to be stored: for small and portable devices, such as medical or communication ones; for medium-sized applications, like the transportation sector; and even for large systems, in the energy storage sector. Batteries are the most widely adopted system for electrical energy storage, and lithium-ion batteries dominate the market.[1] Managing massive energy production from renewable sources will require storage systems able to accumulate energy peaks and fill energy gaps. For this purpose, lithium-ion batteries prove unsuitable. Sustainability is not the strength of lithium-ion batteries, and the large power stations needed will require huge amounts of batteries. Small devices and transportation markets will also increasingly drive the demand for sustainable batteries. This is where the research for new types of batteries, more sustainable, but with good performance, fits in. One of the technologies studied today is zinc-ion batteries. This thesis focuses on the material $ZnMn_2O_4$ (ZMO) and its synthesis and characterization for future use as a cathode in zinc-ion batteries. ZMO, when properly prepared, possesses good electrochemical performance, but its redox mechanisms are still unclear. It is useful to focus on this material precisely to try to clarify its mechanisms and potential. In this work, ZMO is produced by pulsed laser deposition (PLD) in the form of a thin film. The material is studied and characterized by also varying its morphology and composition. The film is also thermally processed to control crystallinity and recharacterized. At the end of the work, early electrochemical tests are performed on the samples, both to verify the electrochemical response of the material and to assess the experimental setup. Analyses performed on the material are exploratory, intending to optimize processes, understand the potential of the material, and reveal possible future study paths that are more focused on individual aspects of the material. This thesis is organized into six chapters, outlined as follows:

- Chapter 1 describes the operation of batteries in general and their components. Before discussing zinc-ion batteries, it introduces primary alkaline and lithium-ion batteries by attempting to show how the two designs are merged in the zinc-ion battery idea. Then, the issues of lithium batteries and how some of these are overcome by zinc-ion batteries are presented. Next, it focuses on describing the possible materials for the zinc-ion cell cathode. The sequent section analyses the material chosen for this thesis: ZMO. It describes the material from a crystallographic point of view, then the properties as a cathode and the critical points for its electrochemistry reported in the literature. The last section of Chapter 1 is a brief presentation of the thesis objectives.

- Chapter 2 describes the experimental techniques used, starting with pulsed laser deposition (PLD) employed for the material synthesis. Then, the characterization techniques are presented: Scanning Electron Microscope, Energy Dispersive X-ray Spectroscopy, Raman Spectroscopy, and UV/Vis/NIR Spectrophotometry, employed to study film morphology, stoichiometry, structural/vibrational, and optical properties, respectively. Finally, the two electrochemical techniques used in the work are presented: cyclic voltammetry and potentiostatic measurements.
- Chapter 3 describes the synthesis of ZMO films. In particular, the target used in PLD for sample production is characterized and the PLD parameters employed for film synthesis are described. Next, the as-deposited films are characterized by evaluating the influence of the deposition parameters on the morphology, stoichiometry, and Raman spectra of the produced samples.
- Chapter 4, on the other hand, analyses samples subjected to annealing. First, the state of the art of Raman spectra of ZMO material is discussed in this chapter, and it is pointed out how it is debated and lacks a purely theoretical study for assignments of active Raman modes. Next, the effects of annealing temperature and atmosphere on film crystallization is discussed. An analysis is presented by comparing annealed films deposited at different oxygen pressures, looking at their stoichiometry, morphology, and Raman spectra. The last section of the chapter deals instead with optical measurements made on the samples.
- Chapter 5 discusses the first electrochemical tests to which some samples were subjected and describes the experimental setup. It also presents the cyclic voltammetries and the reasoning behind testing a sample with potentiostatic measurements, in order to compare the Raman spectra after polarization at selected potential values. It also shows the cyclovoltammetries performed on the bare substrate, following the logical path pursued during the experimental part. Finally, the results of the electrochemical measurements and their possible interpretation are discussed.
- Chapter 6 concludes by summarizing the results of the work and proposing future developments and perspectives.

1 | Zinc manganite as cathode material for zinc-ion batteries

Nowadays, electrochemical storage systems are gaining more and more importance. In everyday life, we rely on devices for every field, just think of smartphones that we always carry in our pockets, medical devices ... technologies of all kinds that do not require to be constantly connected to a power outlet. In addition, these technologies require to be smaller and lighter, while maintaining or exceeding the performance of previous models. In conjunction with these portable devices, transportation is another fundamental sector increasingly making its way into the battery industry. In recent years, the market has grown in the production of all types of hybrid or electric vehicles. From an environmental point of view, to achieve climate neutrality it is necessary to use non-emitting sources of greenhouse gases, such as nuclear energy and renewables, and massive electrification of all services. However, even massive electrification cannot solve the great weakness of solar and wind sources: they are aleatory, the sun does not shine all the time, and the wind does not always blow. Therefore, a solution for the energy crisis that does not emit greenhouse gases will also require electric energy storage systems for a good power management strategy.[2–5] To summarize, the focus on storage systems for devices, the transportation sector, and finally the energy management is extremely high.[6] In this context, the research on new technologies, alternatives to today's ones, is on its way to meet the increasing demand.

1.1. General principles of batteries

An electric battery is a storage system of electric energy consisting of one or more electrochemical cells with external connections for powering electrical devices. Considering one electrochemical cell, its main components are three: the anode, the cathode, and the electrolyte. When a battery is supplying power (discharge phase), its positive terminal/electrode is the cathode and its negative terminal/electrode is the anode. The anode is the source of electrons that will flow through an external electrical circuit to the cathode. When a battery is in the discharging, redox reactions at the electrode-electrolyte interface convert high-energy reactants into lower-energy products, the energy difference is the gained electrical energy. Important practical parameters for an electrode material and for the batteries are capacity, energy and power density, conversion efficiency, and calendar lifespan (or calendar aging). The battery capacity is the amount of electrical charge deliverable under specific discharge conditions, and its unit is Ah.[7] Energy and power densities are a measure of how much energy the battery contains and how quickly it can deliver that energy. Battery energy is the product of capacity and average discharge voltage (expressed in Wh), while the power is the product between current and voltage (expressed in W). Often the specific values of these quantities (specific energy, in Wh/kg and specific power in W/kg, normalized to the mass of the active material/ battery) are used.[8] Conversion efficiency or energy efficiency (ϵ_E), instead, measures the amount of losses between charging and discharging due to chemical reactions, heat release, current/voltage loss, and self-discharge, as shown in:

$$\epsilon_E = \frac{Energy_{Discharge}}{Energy_{Charge}} \tag{1.1}$$

where Energy discharge and Energy charge are the energies delivered by the battery during discharge and provided to it during recharge, respectively. In the end, calendar lifespan is the time for which the battery, in an inactive or minimal use state, can hold its capacity above 80% of its initial one. These parameters can be related to measurable electrochemical parameters such as current, voltage, capacity, and testing duration.

The electrode's intrinsic properties are the voltage and its faradaic capacity.[7] A typical battery reaction for an electrode material A is:

$$A + nM \rightarrow M_nA \tag{1.2}$$

Where A is the electrode material, M denotes the charge-transport ion, and n is the number of ions per reaction. Voltage is strictly correlated to the Gibbs free energy change between reactants and products, as shown in Equation (1.3). Faradic capacity is determined by the number of transferable charges per unit mass of the active electrode material, in Equation (1.4).

$$E = -\Delta G/nF \tag{1.3}$$

$$Q_F = nF/M \tag{1.4}$$

Where E is the voltage, ΔG is the Gibbs free energy change of the reaction, Q_F is the faradic capacity, M is the molar weight of the electrode material A, and F is the Faraday's constant (96485 C/mol). Another important concept is the energy capacity ($\mathcal{E}_C$) of the electrode, which is defined as the product between the voltage and the faradic capacity. As neither the voltage nor the faradic capacity is constant over time, the product is performed under integral as shown in Equation (1.5). [7]

$$\mathcal{E}_C = EQ_F = \int EdQ_F \tag{1.5}$$

In electrochemical processes, energy and charge are conserved, but side reactions can consume some charges, and energy can dissipate as heat. These losses in charge and energy are not negligible factors in the overall problem. The Coulombic efficiency (ϵ_C) of a battery is the ratio between charge and discharge capacity and determines if the electrode material is good or not since in a battery charges are limited and cannot go to waste. The voltage efficiency (ϵ_V) is determined by the voltage ratio (i.e., the potential gap) between the charge and discharge processes.[9] The energy efficiency (ϵ_E) (even called Round Trip efficiency) is the product of the Coulombic efficiency and the voltage efficiency, and is both an economic and a safety issue due to dangerous intense heat generation.
Batteries are divided into two categories: primary systems and secondary systems (rechargeable). [10] Primary systems are cells that, in general, cannot be recharged. They were the first type of batteries and, in particular, the first cell of technical importance was the Leclanché cell. It consists of a zinc anode and a carbon rod or graphite cathode. The advantages of zinc, as negative electrode, are its high specific capacity (820 Ah/kg), the possibility to use an aqueous electrolyte, and the low negative potential compared to the standard hydrogen electrode (-0.76 V vs. SHE).[10] This cell, however, is not rechargeable due to the dendritic precipitation of zinc on the anode itself. Manganese dioxide was also commonly used as a cathode for this type of primary system. Dendritic growth can cause short circuits and subsequent fires, thus making charging impossible.[10]

Secondary systems are rechargeable batteries. The most common and widely used is the lithium-ion battery. Lithium metal is an ideal anode material: it has a high specific capacity (3862 Ah/kg), it is a light element, and has an extremely low redox potential value (-3.05 vs. SHE). It can thus achieve specific energy values over 600 Wh/kg.[10] However, it cannot be used with aqueous electrolytes, it is extremely unstable in contact with liquid organic electrolytes, and it must be handled in inert environment. As a result, other compounds are used as the anode, which can be intercalated and deintercalated, and the lithium ion itself is the charge carrier in the system. Being a small ion, Li^+ ion can be accommodated easily, thus it is compatible with several intercalation compounds.

One of the most commonly used compounds for the anode is graphite (LiC_6), with specific capacity of 372 Ah/kg and voltage of -2.9 V vs. SHE.[10] However, since the anode is not metallic lithium, lithium ions must be already present in the cathode, such as $LiCoO_2$ with 137 Ah/kg and 0.8 V vs. SHE.[10] As with the primary lithium metal system, an organic electrolyte must be used. Lithium-ion batteries with high energy densities (250 Wh/kg), can sustain several hundreds cycles.[10]

1.2. Lithium-ion batteries and their limitations

The history of lithium-ion batteries started in 1962. The first battery was a primary system (non-rechargeable). Then in 1985, the first rechargeable battery was developed by Moli Energy, and Sony introduced it on the market in 1991. The one introduced by Sony was composed of a carbon anode and a $LiCoO_2$ cathode, which are the active materials used in most of modern Li-ion batteries. They began to dominate the market, and in 2000, almost all notebooks were equipped with Li-ion batteries.[1] The Li-ion batteries' advantages are their enormous specific energy, which today exceeds 240 Wh/kg and has the theoretical potential to reach 500 Wh/kg.[11–13]. Thus, they can be implemented in small devices (such as smartphones and notebooks) using 3 to 12 cells connected in series. Their usage in the transport sector is growing more and more as hybrid and electric vehicles are produced. In stationary applications as storage devices, they can span between 2 KWh to 40 MWh. [8]

The working principles of Li-ion batteries are presented in Figure 1.1. An ion-conducting electrolyte is placed in between the positive and negative electrodes. A separator is placed in the electrolyte to electrically isolate the two electrodes from each other. It is a porous membrane that allows the passage of single lithium ions. The lithium ions migrate back and forth during charging and discharging and are intercalated into the active materials. Between the active material and the external circuit, a current collector is present. The active materials of the negative electrode (anode) are mainly graphite or amorphous carbon compounds. Those of the positive electrodes (cathodes) are mixed oxides with some lithium percentage. Let's analyze the main processes during the discharge. Lithium ions are deintercalated from the negative electrode, and to preserve the charge, electrons flow in the opposite direction in the external circuit. When lithium moves inside the cell, the electrons move in the external circuit. The lithium ions migrate in the electrolyte through the separator and in the positive electrode's active material, where they are intercalated and virtually recombine with the electrons. During charging, the process is reversed: lithium ions exit from the cathode and migrate through the electrolyte and the separator

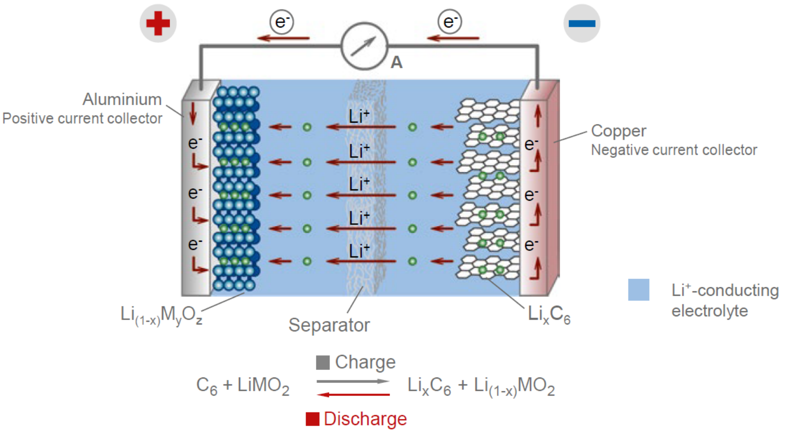

Figure 1.1: Set-up of a lithium-ion battery (shown is the discharging process). Taken from [8]

into the anode, where they are intercalated.[8]

Depending on the application, single cells or cells connected in series as a module, are implemented. If the total capacity is the factor that one wants to increase, then the cells are connected in parallel. Nowadays the battery is integrated with a battery management system for voltage monitor and temperature control.[8]

One of the fundamental criteria for a rechargeable battery is certainly the lifetime, that is, the performance and longevity of the system. During several cycles, the capacity of the battery decreases, and the internal resistance increases over time. Several factors contribute to this performance drop; specifically for lithium batteries (and not only), three main factors can be identified:[8]

1. A protective layer is placed during production on the active material of the negative electrode called the “solid electrolyte interphase” (SEI). This layer prevents direct contact between the electrolyte and the anode’s active material, thus avoiding partial decomposition of the anode. During cycling, though, additional layers form, trapping lithium ions into inactive compounds. These ions are no longer available in the electrolyte for charge transport, and thus the battery capacity is reduced. In addition, the layer that the ions must pass through increases in thickness, which causes a larger resistance to mass transfer and, consequently, a higher internal resistance.

2. Mechanical loading, due to intercalation and deintercalation, can lead to cracks in the active material. These cracks may pulverize the active material particles and electrically insulate them (see Figure 1.2a).

3. Another aging process is related to the expansion of the active material due to intercalation. As the material particles change in volume, they may become dislodged from the electrically conductive paths to the current collectors, as shown in Figure 1.2b.

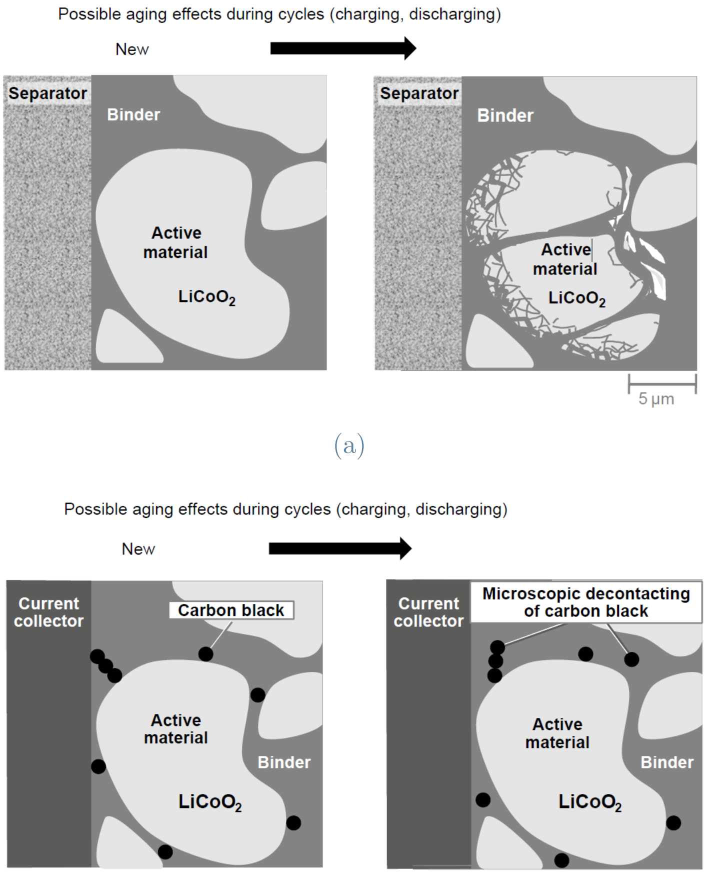

(a)

(b)

Figure 1.2: Aging processes in the active material of the positive electrode during cycling: Pulverization (a), separation of electrical conduction paths (b). Taken from [14]

Finally, in addition to lifetime, which is common to all batteries, the limitations to lithium-ion batteries promote alternative solutions. In lithium-ion batteries, typical cathode materials contain cobalt, which is one of the critical steps in the supply chain. Cobalt is rare, expensive, and toxic. Waste generated from mining cobalt can pollute water, air, and soil, leading to decreased crop yields, contaminated food and water, and health issues.[15, 16] Another major limitation is the organic electrolyte, which is difficult to recycle and flammable.[17] Both limitations can be overcome by secondary zinc-ion systems, which this thesis focuses on.

1.3. Zinc-ion batteries

As mentioned above, lithium-ion batteries benefit from high specific energy, long cycle life, and they are lightweight. This has allowed them to be the most attractive electrical energy storage (EES) systems in the communication and transportation industries.[11, 18–20] On the other hand, lithium-ion batteries as large-scale energy storage devices are limited by high costs, safety and environmental issues. Organic electrolytes are highly toxic and flammable, in addition, side reactions with electrodes increase the risk.[21] There is no doubt that lithium-ion technology will improve and such systems will achieve better performance, however, there is an increased focus on secondary systems of other designs.

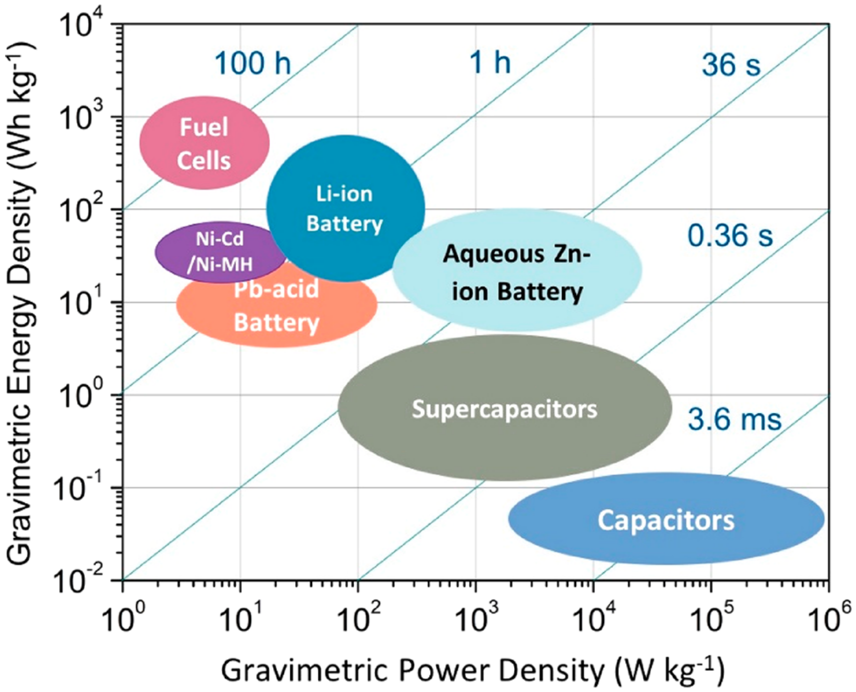

Figure 1.3: Ragone plot of several EES systems. Taken from [22].

Zinc-ion batteries (ZIBs) are a promising technology, particularly for stationary storage applications. Non-toxic and abundant materials are used, and these batteries can provide more specific power than lithium-ion batteries.[23–25] A comparative Ragone plot is presented in the Figure 1.3. The key advantages of zinc-ion batteries are:

1. The availability of zinc: it is among the most common elements in the earth's crust and it is present on all continents and it is produced worldwide at affordable prices. In addition, the recycling technology for Zn is well-established;
2. The use of an aqueous electrolyte that is low cost, non-flammable, non-toxic, safe and versatile for design modifications;

3. The stability of metallic zinc in the aqueous electrolyte, which allows its use in the battery without resorting to zinc compounds and thus leading to a higher theoretical capacity.

Rechargeable ZIBs are the evolution of primary non-rechargeable zinc systems. They use a metallic zinc anode and the cathode can be manganese oxide. However, the aqueous electrolyte, in this case, is slightly acidic instead of that of alkaline primary systems.[6] The development of aqueous ZIBs is nowadays mainly aimed at finding compatible cathodes and studying the associated electrochemical mechanisms.[22]

The zinc metal anode is versatile, provides high energy, low cost, and large capacity. In the battery, divalent zinc ions are the charge carriers and must migrate from the zinc electrode to the cathode through the electrolyte. This is the reason why ZnO or other zinc precipitates on the anode are undesirable. To avoid precipitates, the electrolyte design, architecture and surface properties of the anode must be addressed. The reactions and mechanisms involving the zinc anode in the aqueous electrolyte depend on the pH and composition of the solution. Traditional (primary) zinc batteries use highly concentrated alkaline solutions (e.g., KOH), while the electrolyte for secondary systems is a near-neutral solution (e.g., $ZnSO_4$). The reaction at the anode for acidic and near-neutral solutions is:

$$Zn \leftrightharpoons Zn^{2+} + 2e^{-}, -0.762 V vs SHE \tag{1.6}$$

The main challenges faced by the negative electrode are corrosion in acidic electrolyte and subsequent hydrogen production; surface passivation, especially for near-neutral electrolyte; and shape change and dendritic growth, due to dissolution and re-precipitation of zinc from solution to the electrode and vice versa.[6] Regarding the aqueous electrolyte of the ZIB, its high ionic conductivity, low price, non-flammability, and environmental safety should be highlighted. The kinetics of reactions and the electrochemical stability of the electrolyte are still under study. The most common salt is $ZnSO_4$ for near-neutral solutions. For charge transport, it is preferable to have non-complexed zinc, however, in zinc sulfate-based electrolytes, neutral or negatively charged zinc sulfate or hydroxide complexes make up most of the electrolyte. This affects charge transport, zinc dendritic growth, and cathode reaction mechanisms.[26] The last important electrolyte criticality is that zinc operates outside the theoretical electrochemical stability window of water, which leads to hydrogen gas evolution for acidic/near-neutral solutions. One proposed fix is to use super-concentrated solutions of zinc salts and water to widen the stability window. As can be seen in Figure 1.4a, primary alkaline batteries have two distinct redox processes, occurring one at the cathode and the other at the anode, causing non-direct charge transfer. In the Figure 1.4b, instead, we see the shuttle mechanism for a zinc-ion

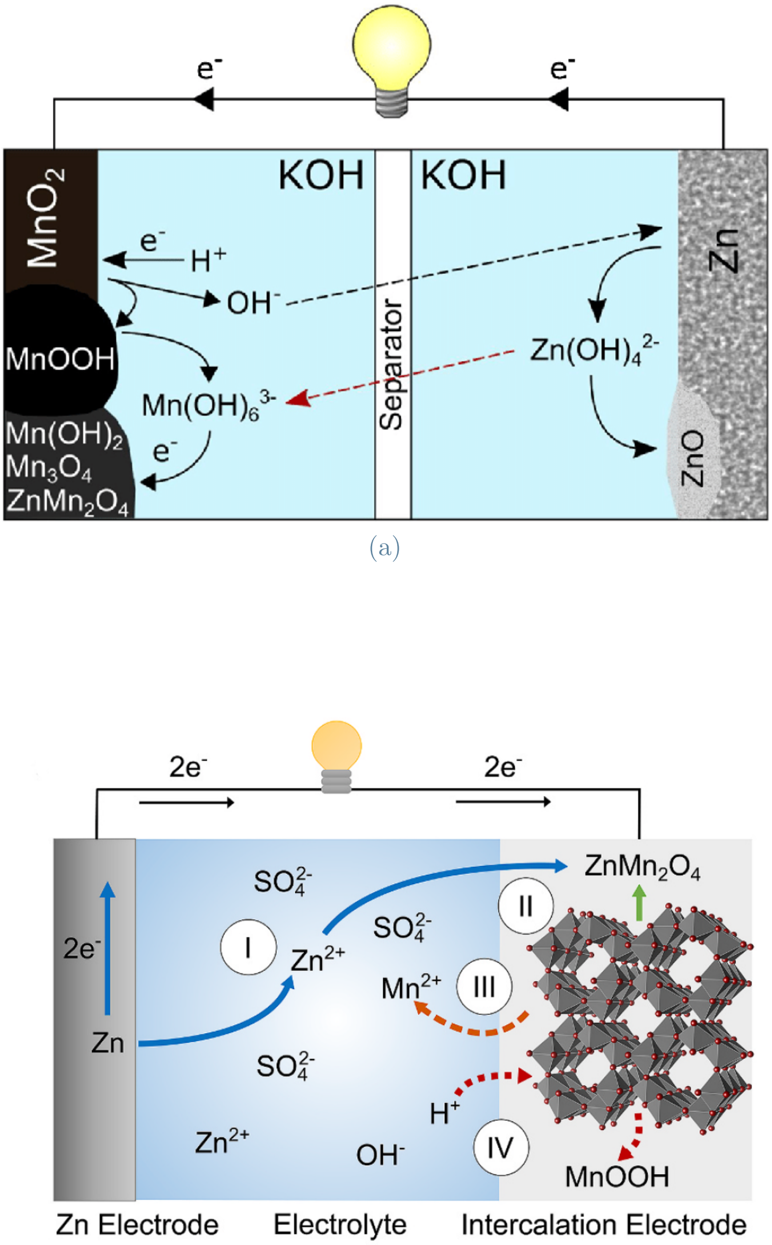

(a)

(b)

Figure 1.4: Comparison between battery reaction scheme: Primary alkaline battery (a) vs. Zinc-ion battery (b). Taken respectively from [27] and [6]

rechargeable battery, where the charge passage is due to the migration of Zn^{2+} from the anode to the cathode. During discharge, when the zinc-ion reaches the cathode, it intercalates, accompanied by the reduction reaction of the host cations. Below, one of the possible occurring reaction is reported:

$$Zn^{2+} + 2MnO_2 + 2e^- \rightarrow ZnMn_2O_4 \tag{1.7}$$

This work focuses on one candidate cathode material for zinc-ion batteries and a more detailed description of the cathode active material is presented in the following paragraph.

1.4. Cathode materials for zinc-ion batteries

One of the major challenges of zinc-ion batteries (ZIBs) is finding the best cathode material. Assuming zinc metallic as the anode, the open-circuit voltage and the zinc-ion storage capacity of a ZIB are almost up to those of the cathode. Electronic and ionic transport properties and reaction kinetics of the cathode affect the specific energy and power of the ZIB. In the end, cathode stability and integrity over the cycles are major factors in the cycling stability of the battery itself.[22] Hence, cathode materials with high voltage, fast kinetics, good specific capacity, and long cycling stability are evaluated. Moreover, the requirements of a ZIB's good cathode active material are the possibility to reversibly host a divalent charge carrier, remaining intact during intercalation/deintercalation reactions.[6] The layered, tunnelled, or spinel structures in metal oxides may comply with these requirements. However, the drawbacks of these materials are: 1) phase transformation that induces mechanical stress, limits ion diffusion, and alter the electrolyte pH through the release or insertion of H^+; 2) loss of capacity due to dissolution of the host metal cations in the electrolyte.[6]

For ZIBs, the feasible cathode materials are manganese-based compounds, vanadium-based materials, Prussian blue-like structures, and some organic redox-active compounds. A detailed analysis of recent studies on these materials as cathodes is found in Jia et al. [22], Borchers et al. [6], Song et al. [28], Blanc et al. [29], and Li et al. [30]. In this text, the main concepts of vanadium oxides and the Prussian blue analogues (PBAs) are mentioned, and a more detailed discussion is given for manganese oxides.

Vanadium-based materials have a large theoretical capacity, a versatile crystalline structure, resource abundance, and low cost. Moreover, the multiple oxidation states of vanadium allow a variety of vanadium oxides. However, these oxides often suffer from low operating voltage (∼ 0.75 V), which results in a large volume of the battery.[31] Vanadium compounds different from oxides have also been studied, such as metal vanadates and vanadium phosphates.

Prussian blue and its analogues (i.e., the mixed-valence hexacyanoferrate family) have some structural advantages as cathode materials:[31]

1. Their structure has large channels that favor rapid ion migration with less volume variation.
2. The multitude of transition-metal and alkali-metal ion combinations allows tailoring the electrochemical properties of the PBAs.
3. The PBAs have two redox-active centers, which means a higher theoretical capacity.

These merits have driven the interest in this family of materials as cathodes for lithium- and sodium-ion batteries, while further study is needed to implement them in ZIBs. Moreover, the actual capacity ($\sim$ 70 mAh/g) in ZIBs is still lower than other materials.[22, 31]

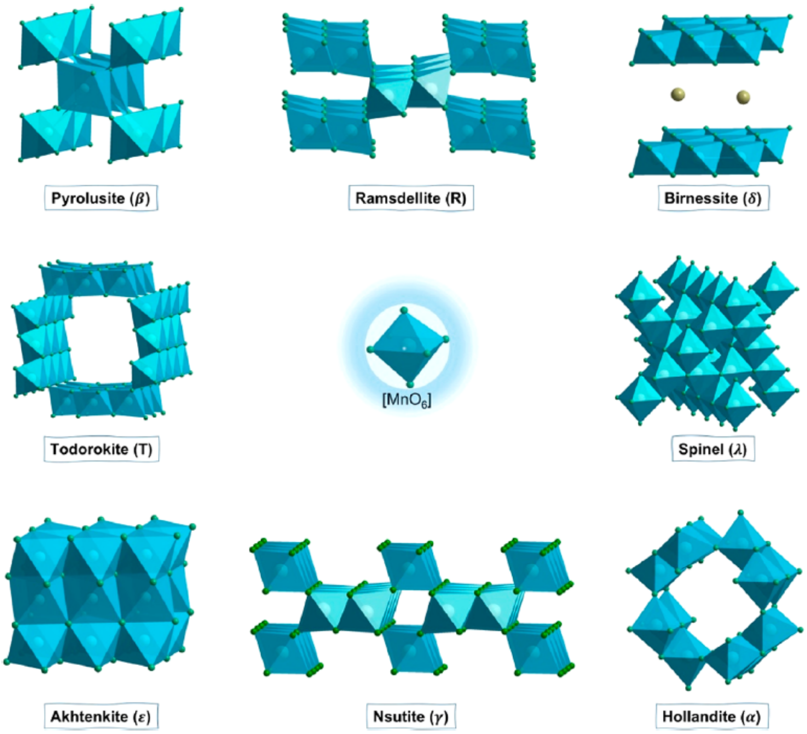

Figure 1.5: Representation of different MnO_2 polymorphs and their basic unit. Taken from [22].

Manganese dioxide (MnO_2) materials are particularly desirable candidates for large-scale systems due to their abundance (Mn is the 10th most abundant element in the Earth's crust[28]), easy processing, eco-friendly nature, and low cost.[29] The theoretical specific capacity for manganese oxide is 308 Ah/kg, with one electron transfer per formula unit. The basic unit of the various Mn-oxide structures is one Mn^{4+} ion coordinated with six hexagonally close-packed O^{2-} ions, as the one in the middle of the Figure 1.5. By connecting these units in different ways, sharing corners or edges, tunnelled or layered polymorphs are formed. The Figure 1.5 shows some possible configurations. As cathode materials for ZIBs, each of the polymorphs has its own merits and issues. For example, the α-MnO_2 material has large tunnels (4.6 Å) for Zn^{2+} ions accommodation, thus high specific capacity with moderate discharge voltage. However, this polymorph suffers from rapid capacity fading and poor rate performance (it provides a considerable specific capacity at low current rates, but only for a few dozens of repeated cycles).[24, 32] On the contrary, considering the δ-MnO_2, which possesses a layered-like structure, the accommodation space between two layers of the crystal is even larger (7 Å), yet leading to rapid capacity fading upon long-term cycling. Moreover, the formation of inactive compounds and the loss of active species (as in Equations (1.8), (1.9)) threaten the cathode stability.[33]

$$MnO_{2(s)} + H^+ + e^- \rightarrow MnOOH_{(s)} \tag{1.8}$$

$$MnOOH_{(s)} + 3H^+ + e^- \rightarrow Mn^{2+}_{(aq)} + 2H_2O \tag{1.9}$$

One possible strategy to avoid the Mn dissolution (also adopted in this work) is the addition of Mn salts into the electrolyte.[33] However, electrolytes containing Mn^{2+} allow the electrodeposition of MnO_2 onto the electrode surface[34], which may reduce the cathode quality and/or passivate the electrode-electrolyte interface.[29]

The last structure of interest in this work is the λ-MnO_2, which crystallizes in a spinel structure as shown in Figure 1.6. The structure is composed of octahedral units and tetrahedral voids (further details are treated in the section 1.5). The λ-MnO_2 is not suited for the insertion of the Zn^{2+} ions, since the structure is too compact, however, a similar spinel structure with mixed Zn^{2+} and Mn^{3+} cations is the cathode material studied in this thesis.

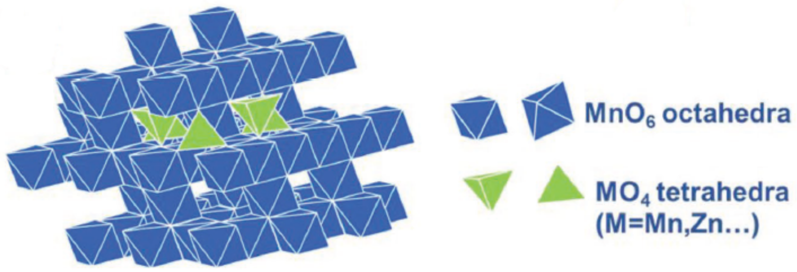

Figure 1.6: λ-MnO_2 structure and its basic units. Taken from [28]

Notably, Mn oxide polymorphs can transform mutually during electrochemical cycling. These transformations are accompanied by the insertion/extraction of water molecules and/or cations. Since the mechanism behind the electrochemical processes of these materials is rather complex and still unclear, considering that these transformations contribute to the overall process allows a better understanding of the ZIBs' mechanisms.[28] In general, the manganese oxide active materials undergo complex structural transformations from tunnel-like to spinel-like and layered phases on discharging.[35] These transitions of structure and phase, along with Mn dissolution, lead to poor cyclability.[36] Indeed, the energy storage mechanism of the ZIBs, according to the current research, can involve one or a combination of the following:

1. Zn^{2+} insertion/extraction[37];
2. H^+/Zn^{2+} co-insertion/extraction[38];
3. H_2O and Zn^{2+} co-insertion/extraction[39];
4. conversion reaction[40];
5. dissolution and deposition reaction[41].

These mechanisms are schematized in Figure 1.7. All the mechanisms listed can contribute, alone or even more than one at a time, to energy storage. However, it is necessary to understand which is the main one for the material optimization purpose.

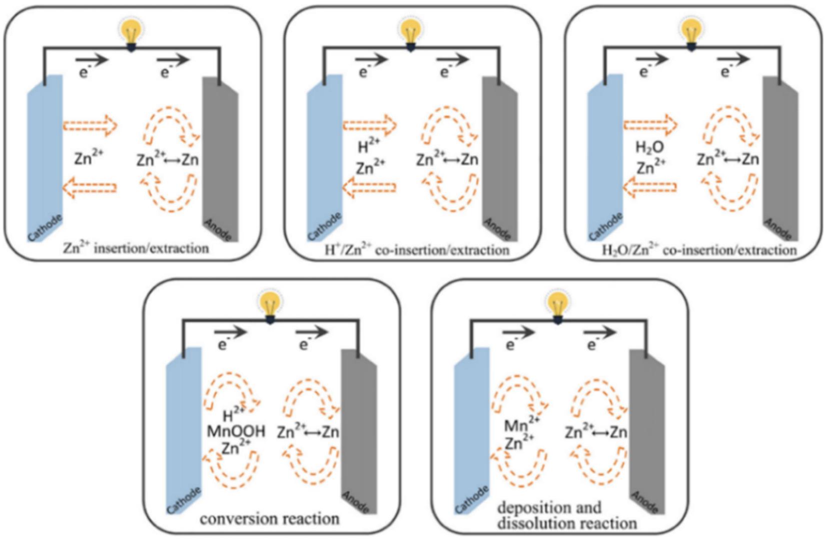

Figure 1.7: Scheme of possible ZIBs energy storage mechanisms. Taken from [31]

The open key points of the Mn oxide cathodes are: (i) competition between Mn^{2+}

dissolution and MnO_2 deposition, (ii) appropriate characterization of the cation insertion/deinsertion mechanisms, and (iii) performance optimization of the materials.[29]

1.5. Zinc manganite $ZnMn_2O_4$ (ZMO)

It appears that most of MnO_x undergo irreversible phase transformation into $ZnMn_2O_4$ spinel after multiple charge/discharge cycles.[42] The $ZnMn_2O_4$ (ZMO) material has been recently studied as one of the possible cathodes for ZIBs. By acting on the stoichiometry and morphology of the material, good electrochemical performances can be obtained. Research on this material is ongoing and the ZMO production for electrochemical purposes by Pulsed Laser Deposition (PLD) technique is quite unexplored.

1.5.1. ZMO general material properties

$ZnMn_2O_4$ (ZMO), also known as hetaerolite, is a normal spinel structure. ZMO belongs to the zinc manganites family ($Zn_xMn_{3-x}O_4$). Its structure is composed of tetrahedral and octahedral sites, occupied by divalent cations and trivalent cations, respectively. In ZMO, Zn^{2+} ions occupy 1/8 of the tetrahedral sites (ZnO_4), while Mn^{3+} ions reside in 1/2 of the octahedral sites (MnO_6).[36] ZMO has a tetragonal distortion of the spinel lattice due to a strong Jahn-Teller distortion effect on the octahedral coordinated Mn^{3+}. The high-spin Mn^{3+} cation in octahedral coordination has an electron configuration that leads to the distortion, which results in the elongation of one of the Mn-O bonds and, hence, to a distortion from a cubic spinel to a tetragonal spinel ($I4_1$/amd).[43–45]

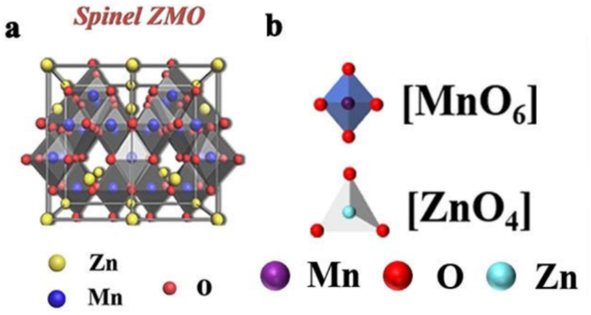

Figure 1.8: Schematic representation of the ZMO crystal (a) and the occupied tetrahedral and octahedral sites (b). Taken from [31]

1.5.2. ZMO as cathode material

A similar structure, the $LiMn_2O_4$ (LMO), was studied for lithium-ion battery implementation (for cost, environmental, and energy issues), and it has proved that it can intercalate Li^+ reversibly. Since the lithium and zinc ionic radii are comparable, indicating that the transport kinetics of the two ions may be similar, $ZnMn_2O_4$ became a candidate active material for the ZIBs.[31, 36] Unfortunately, although ZMO as cathode material has a theoretical specific capacity of 224 Ah/kg[46], experiments show that pure ZMO is unfit for Zn^{2+} insertion due to the high electrostatic repulsion among Zn ions with the lattice.[31, 36, 47]

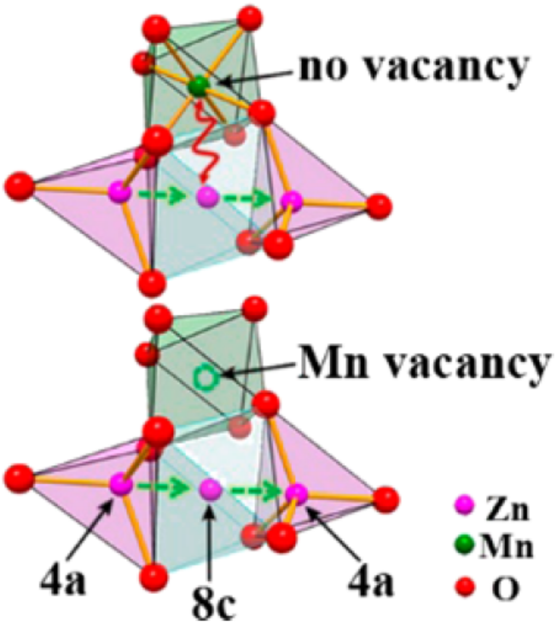

Figure 1.9: Schematic representation of the Zn^{2+} ion diffusion in a pure ZMO structure (above) and in a ZMO structure with defects (below). Taken from [36].

One of the reasons behind the poor electrochemical performance of the pure ZMO is schematized in Figure 1.9. The Zn ion, with a high valency state (2+), moves from a tetrahedral site (4a) to another tetrahedral site. By making this passage, it crosses an unoccupied octahedral site (8c), but the repulsion from the adjacent octahedral site occupied by the Mn^{3+} is very strong and obstacles the ion diffusion. So the Zn ions cannot diffuse quickly in the spinel, resulting in poor battery performance.[31, 36] Moreover, the Jahn-Teller effect, due to the Mn^{3+}, induces distortion in the lattice, which shifts from a cubic spinel (with Mn^{4+}) to a tetragonal spinel. During charging/discharging processes, Mn^{3+} undergoes disproportion, leading to the dissolution of Mn^{2+}. Other issues of ZMO are low electrical conductivity, volumetric expansion, and phase transformation during cycling, and the electrochemical mechanism is unclear and little studied.

1.5.3. ZMO critical aspects as cathode material

There are different strategies to enhance the ZMO electrochemical performance:

1. Introduction of vacancies in the structure.
   The introduction of vacancies removing some cations (i.e. Mn^{3+}) relaxes the electrostatic condition of the structure. In the presence of a vacancy, the electrostatic repulsion is reduced and the ions conductivity in the crystal increases. The Zn-ion during diffusion, as shown in the bottom part of the Figure 1.9, travels from a tetrahedral site (4a) to another tetrahedral site, and when crosses the unoccupied octahedral site (8c), it does not feel the electrostatic repulsion because of the Mn^{3+} absence.[47] To measure the actual presence of vacancies in the ZMO, since the valence number for oxygen and zinc is fixed, it is enough to check the average valence number of manganese. If this is greater than +3 it means that there are vacancies.

2. Heteroatom doping engineering.
   Metal atom doping can change the electronic structure of the material by generating excessive or insufficient valence electrons. It is proved that the metal ions embedded in the crystal structure can expand the lattice spacing. At the same time, they can prevent the crystal structure collapse after repeated Zn^{2+} insertion/extraction, improving the cycle stability.[31]

3. ZMO/Carbon compound engineered materials.
   Some studies have improved the ZMO performance by combining nanostructured ZMO sustained by carbon structures, which improved the material durability and provided a conductive path. This technique was used in the article by Yang et al. [46].

4. Nanostructured ZMO and morphology modifications.
   Changing the morphology allows having more active sites in the material, increasing the conductivity (due to shorter path) and the diffusion. Moreover, reducing the crystal size or developing some peculiar morphologies can alleviate the strain on the structure due to volume change.[31, 36, 42]

A summary of the different strategies adopted in the recent articles is presented in the Table 1.1. The ZMO electrochemical mechanism is not yet clear. Some of the mechanisms hypothesized for Mn oxides, reported above in Section 1.4, are found in research articles dealing with ZMO. Although the insertion/extraction of zinc ions is one of the most accredited mechanisms[36, 46], there are also studies reporting on the mechanism of H^{+}/Zn^{2+} co-insertion/extraction[60], intercalation of H^{+} only[61], and dissolution/deposition reac-

Cathode	Morphology	Average size (nm)	Electrolyte	Cycling behaviors	Potential window	Ref.
ZMO	submicron spheres	~500	1 M $ZnSO_4$+ 0.05 M $MnSO_4$	~189.5 $mAhg^{-1}$ at 0.2 Ag^{-1} (500 cycles)	0.4–1.4 V	[48]
ZMO@PCPs	Cubic-like	~500	1 M $ZnSO_4$+ 0.05 M $MnSO_4$	~125.6 $mAhg^{-1}$ at 1 Ag^{-1} (2000 cycles)	0.8–1.8 V	[46]
ZMO NDs/rGO	nanodots	5–10	1 M $ZnSO_4$+ 0.1 M $MnSO_4$	~207.6 $mAhg^{-1}$ at 0.2 Ag^{-1} (100 cycles)	1.0–1.8 V	[49]
HP-ZMO	microspheres	~300	1 M $ZnSO_4$+ 0.05 M $MnSO_4$	~106.5 $mAhg^{-1}$ at 0.1 Ag^{-1} (300 cycles)	0.8–1.9 V	[50]
Porous ZMO	Rod-like	2000	1 M $ZnSO_4$+ 0.1 M $MnSO_4$	~225 $mAhg^{-1}$ at 0.1 Ag^{-1} (200 cycles)	0.6–1.9 V	[51]
ZMO@Ti3C2Tx	3D layered structure		1 M $ZnSO_4$+ 0.05 M $MnSO_4$	~120 $mAhg^{-1}$ at 1 Ag^{-1} (5000 cycles)	0.8–1.5 V	[52]
ZMO@N-graphene	nanoparticles	21	1 M $ZnSO_4$+ 0.05 M $MnSO_4$	~74 $mAhg^{-1}$ 1 at 1 Ag^{-1} (2500 cycles)	0.8–1.8 V	[53]
ZMO@C	nanoparticles	~15	3 M $Zn(CF_3SO_3)_2$	~150 $mAhg^{-1}$ at 0.5 Ag^{-1} (500 cycles)	0.8–1.9 V	[36]
ZMO@C	3D structure		2 M $ZnSO_4$+ 0.1 M $MnSO_4$	~481 $mAhg^{-1}$ at 0.2 Ag^{-1} (110 cycles)	1.0–1.8 V	[54]
OD-ZMO@PEDOT	Fiber-like	~10000	1 M $ZnSO_4$	Capacity retention 93.8% (300 cycles)	0.8–1.9 V	[55]
HM-ZMO@rGO	Hollow microspheres	~1000	1 M $ZnSO_4$+ 0.05 M $MnSO_4$	~146.9 $mAhg^{-1}$ at 0.3 Ag^{-1} (100 cycles)	0.8–1.8 V	[56]
MD-ZMO@C	nanoparticles	9.55	2 M $ZnSO_4$+ 0.2 M $MnSO_4$	~98 $mAhg^{-1}$ at 3 Ag^{-1} (2000 cycles)	0.8–1.9 V	[57]
ZMO/Mn2O3	microspheres	5000–7000	1 M $ZnSO_4$	~111.9 $mAhg^{-1}$ at 0.5 Ag^{-1} (300 cycles)	0.8–1.9 V	[58]
ZNCMO@N-rGO	nanoparticles	~50		~95.4 $mAhg^{-1}$ at 1 Ag^{-1} (900 cycles)	0.7–1.7 V	[59]

Table 1.1: A summary of recent studies on $ZnMn_2O_4$ electrode materials for ZIBs.

tions [42, 51]. Soundharrajan et al. [51] and Wu et al. [42], for example, proposed that the MnO_x electrodeposited from the Mn^{2+}-containing electrolyte on the pristine ZMO during charge interacts with the ions of the electrolyte ($ZnSO_4$, $MnSO_4$) and undergoes Zn insertion, transforming itself reversibly in ZMO. In the end, it is worth mentioning that in the $ZnSO_4$ electrolyte large flakes can be observed on the surface of the electrode at the discharged state.[42] They correspond to the formation of basic Zn precipitates, like the zinc hydroxy sulphate hydrate phase $ZnSO_4[Zn(OH)_2]_3 \bullet xH_2O$ (ZHS). These precipitates can reversibly form and dissolve upon electrolyte pH increase, and are accompanied by proton insertion/extraction into the cathode.

As seen above, there are several ways to increase the electrochemical performance of the ZMO material. One of these is to act on the nanostructure and morphology. In this work, I produced ZMO thin films with different morphologies and stoichiometries through the PLD. The possibility of using thin films for energy storage and conversion has several advantages, including high reproducibility, easy control of the growth rate, and a high film purity with a variety of substrates. Producing a thin film electrode for an electrochemical cell offers other advantages: first of all, it is self-supported, without the aid of polymeric binders and carbonaceous additives; secondly, thin films are well suited for the design of devices (such as microbatteries); and thirdly, decreasing the thickness and increasing the available surface area leads to increased conductivity of the material and better electrode-electrolyte charge exchange.[62]

1.6. Thesis objectives

This work fits into the context of zinc-ion batteries and, in particular, focuses on the ZMO material. The ZMO is produced in the form of a thin film controlling its morphology and thickness by pulsed laser deposition (PLD). Although this thesis considers the electrochemical application of the material as a long-term objective, the characterizations carried out concern the material per se in general, beyond the possible future application. It is true, indeed, that the literature on the material for characterization purposes alone is scarce and, in some cases, controversial.

This work also serves as exploratory work for future developments of ZMO. Most of the thesis focused on characterizing the material, which is not only useful in at the research level, as mentioned above, but it also allows us to optimize processes for a certain application.

To summarize, the objectives of this thesis are:

1. The production of ZMO thin films using PLD, the optimization of parameters to produce films with certain properties (thickness, morphology, porosity, and density) and stoichiometry, with the aid of different gas atmospheres during deposition.
2. The characterization of the produced materials by Raman spectroscopy, scanning electron microscopy (SEM), Energy Dispersive X-ray Spectroscopy (EDXS), and UV-VIS optical spectroscopy, and the correlation of the material properties to the parameters used in the synthesis process.
3. The conducting of some preliminary electrochemical tests aimed at observing the material response and at characterizing the material changes in the aged samples. Such tests were also used to assess and optimize a proper cell setup suitable for the electrochemical characterization of thin films.

2 | Experimental Techniques

In the previous chapter, we discussed the state of the art in zinc-ion batteries and the peculiarities of the ZMO material. In the following, I present the synthesis and characterization methods adopted in this work. In the end, a brief presentation on the electrochemical techniques adopted is offered.

2.1. Pulsed Laser Deposition

Pulsed Laser Deposition (PLD) is a thin films deposition technique onto a substrate. It is a very versatile method and metallic, semiconductor, oxide, ceramic, or polymeric materials can be deposited. The deposited films can also be nanostructured, the thickness can be properly controlled, and the stoichiometry of the material can be complex. PLD belongs to Physical Vapour Deposition (PVD) techniques and it is based on the plasma produced by the target material ablated by intense laser pulses.[63]

The versatility of PLD is based on the number of parameters that can be set. The plasma plume originates from the laser impinging on the target and it is influenced by the energy of the laser itself, the background gas in the chamber (reactive or non-reactive), the pressure in the chamber, and the materials that make up the target. This whole variety of parameters allows control over the thickness, density, stoichiometry, and morphology of the produced sample. Consequently, this wide range of possibilities is well suited for experimental and research activities: indeed, this flexibility allows tuning the sample properties, studying the behavior of the deposited material under different conditions, and optimizing it for the final application.

The PLD apparatus scheme is presented in Figure 2.1 .

Firstly, both the target and the substrate are in a stainless-steel vacuum chamber to avoid interaction with the ambient atmosphere and to control the deposition pressure. The chamber's pressure is controlled by a primary vacuum pump and a turbomolecular pump connected in series. The latter is used to evacuate the chamber down to the high vacuum regime ($\sim 10^{-3}$ Pa). For depositions in gas atmosphere, a gas pressure system with an inlet is present. The pulsed laser is focused following an optical path consisting of

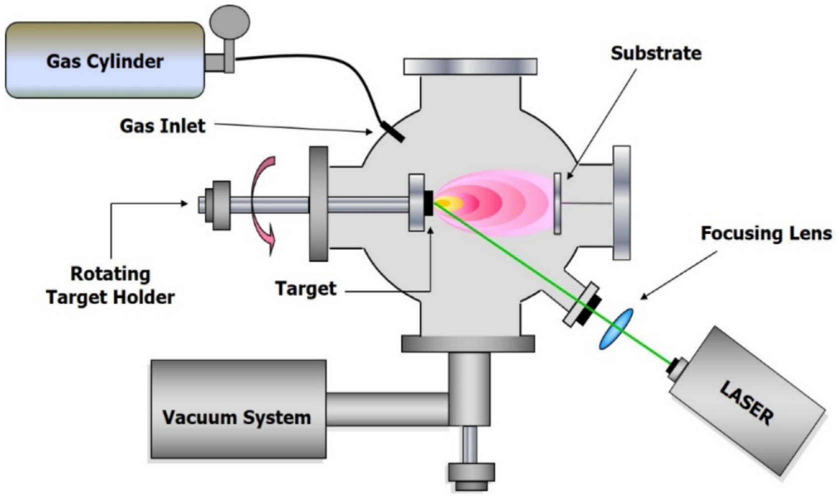

Figure 2.1: Pulsed Laser Deposition schematic apparatus. Taken from [64].

lenses, mirrors, and driven through a final window to the vacuum chamber. The laser hits the target at a 45° angle with respect to the target surface, thus avoiding irradiating other components such as the substrate. The substrate is placed in front of the target since the plasma plume is forward directed. The holders of both the target and the substrate can be controlled by motors that can set the relative positions and govern translations and rotations.[63]

The target is thus irradiated by the pulsed laser and, above a certain fluence, which depends on the target material, it begins to ablate. The vaporized particles (ions) are ejected from the target, they can have different sizes, and form the plasma plume. This plume is aimed at the substrate, so when the particles reach the solid substrate they aggregate and grow as a thin film.

The parameters that can be tuned in this process allow one to control the morphology and the thickness of the film, the most relevant of these being the background pressure, the distance between the target and the substrate d_{ts}, the laser fluence, and the type of gas used during deposition (for example, if it is reactive or not). With respect to deposition and background gases, there are three distinct possible conditions:

- When deposition is in vacuum, the ablated species leave the target and on their way to the substrate they do not interact with the environment. As a result, deposition occurs atom by atom without aggregation until they arrive on the substrate. The ablated species arrive with high kinetic energy and are well directed, forming a compact film with good adhesion. In this situation, the plasma plume is not visible.
- In the case of inert background gas being present, a compression zone between the ablated species and the gas is present. The plume is confined by the gas and a shock

wave originates. The luminescence of the plume is higher and it becomes visible, as can be seen in Figure 2.2. The ablated species are confined in the plume, thus they tend to nucleate and to reach the substrate as clusters, especially during depositions at high gas pressure. The kinetic energy is partially dispersed during the collisions. Since the plume itself is more confined in the space, it is less long and broader. The porosity of the film increases with the gas pressure.

- In a reactive gas atmosphere, the mechanism is similar to the one above; furthermore, the clusters stoichiometry can be modified by the presence of the gas according to its pressure.

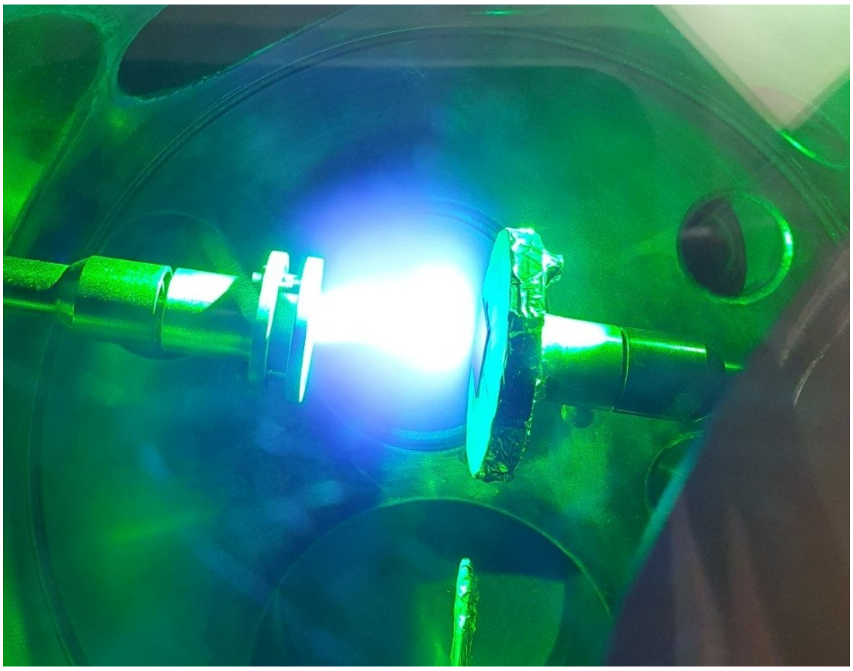

Figure 2.2: Picture of the PLD plasma plume during operation in argon (100 Pa).

In this work, the depositions were performed mainly in oxygen atmosphere and vacuum. Oxygen is a reactive element for ZMO films deposition, so some initial tests for comparison were performed in argon, that in contrast is inert being a noble gas. The laser fluence influences the deposition rate above all. Obviously, with higher fluence the deposition rate increases, but at the same time the deposition rate also depends on the target material and on the relative positions of target and substrate.

The morphology of the final film depends on all these parameters. One way to take into account the target-substrate distance and the impact of the gas pressure is the following. Firstly, it has to be underlined that the background gas molecules or atoms obstacle the ablated particles travel, thus the length of the visible plasma plume (l_p) shortens. The higher the mass of the background gas is, the more the scattering will be effective and will slow down the ablated particles. In addition, scattering will be more likely as the gas pressure increases. Secondly, making this logical connection between l_p and gas pressure, a dimensionless parameter L can be introduced.[65] For a well-defined shock front of the plasma plume (P>10Pa), L is defined as the ratio between d_{ts} and l_p. Using this parameter, three different deposition regimes can be identified, summarized in Figure 2.3:

- when L<1, the substrate is inside the plume, the particles arrive with high kinetic energy and the porosity is reduced, so a very compact film is obtained with a smooth surface;
- for L∼1, the edge of the plume is in contact with the substrate. The ablated species have less kinetic energy due to interaction with the background gas. When oxides are involved, vertically structured and porous films are produced, and peculiar nanostructured tree-like films can be obtained. This kind of "nanoforest" features a high specific surface and high porosity;
- when L>1, the plume is distant from the substrate. The kinetic energy of the ablated particles is lost during scattering and collisions and the deposition of clusters on the substrate is expected. The adhesion is lower and the film is usually nanoporous.

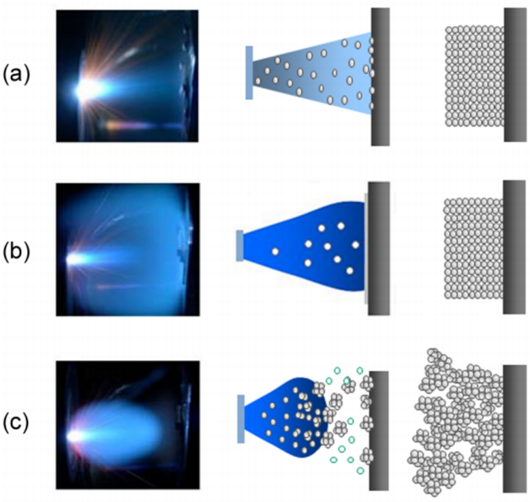

Figure 2.3: Scheme of the three different deposition regimes.[66]

PLD has some drawbacks.[63] All these tuneable parameters allow the production of a plethora of different films, but at the same time they strongly affect the reproducibility. Another issue is the difficulty of maintaining thickness uniformity on the sample over a few cm^2 due to the gaussian shape of the ablated species emission. Even deposition on a not-planar sample is not always possible with PLD as a shadowing effect takes place.

The uniformity can be extended by misaligning the roto-translation of the substrate with respect to the target, though limitations on some cm^2 thickness uniformity remain. The quality of the film itself can suffer due to the so-called droplets, which are micro-sized particles detached from the target that deposit on the substrate and are embedded in the nanostructured architecture of the film. This is the reason way PLD technique does not fit well for industrial processes; however, concerning research purposes, PLD finds its place as a valuable and useful technique thanks to its versatility, simplicity, and feasibility. Focusing on this work merits, PLD is a successful technique for multicomponent oxide films, whose growth rate can be easily controlled and which can be deposited on any substrate, including silicon, FTO-coated glass, and bare glass.
In the end, the PLD's advantageous aspects for this work are:

1. the possibility of obtaining stoichiometries different from that of the target by depositing in oxygen atmosphere at diverse pressures;
2. the possibility of obtaining various morphologies (hence porosity, density, and specific surface area) acting mainly on gas pressure and fluence;
3. the possibility of decoupling the two by depositing in inert gas or mixture.

Moreover, concerning electrochemical applications, as seen in Chapter 1, there are three important aspects that our work with PLD can explore[62]:

1. Maximize the surface area of the film to have the best contact between electrode and electrolyte;
2. Exploring the effect of a nanostructured film to reduce the electron and ions diffusion path, and consequently, reduce the charge-transfer resistance;
3. Having a self-supported material without the need for conductive additives and polymeric binders.

The ablation laser used in this project is a solid state Q-switched Nd:YAG laser providing pulses in the visible (second harmonic, 532 nm wavelength, 10 Hz repetition rate, pulse duration 5-7 ns). All films were grown at room temperature on Si (100) (Siegert Wafer), soda-lime glass (Marienfeld), FTO-coated glass (Sigma-Aldrich) by ablating a $ZnO : Mn_2O_3$ (1:1 mol%), hot pressed, 99.99% purity target, supplied by Testbourne B.V. The target-to-substrate distance was kept constant at $d_{ts} = 5$ cm, while the fluence was varied between 2.15 and 9 J/cm^2. The films were deposited in vacuum and at a background pressure varied between 1 Pa to 150 Pa in O_2, Ar or Ar/O_2 atmosphere.

2.2. SEM and EDXS

2.2.1. Scanning Electron Microscopy

Scanning Electron Microscope (SEM) is a non-destructive investigation tool for sub-micrometric morphology and structure. An energetic electron beam is focused on the sample and several signals are emitted, among them secondary electrons. These electrons are collected by a detector, converted into electrical signals, and sent in real-time to the screen. The result is a grayscale image with high resolution (about of some nanometers).[63] Therefore, SEM provides information about the sample such as morphology, topography, and orientation of the material.

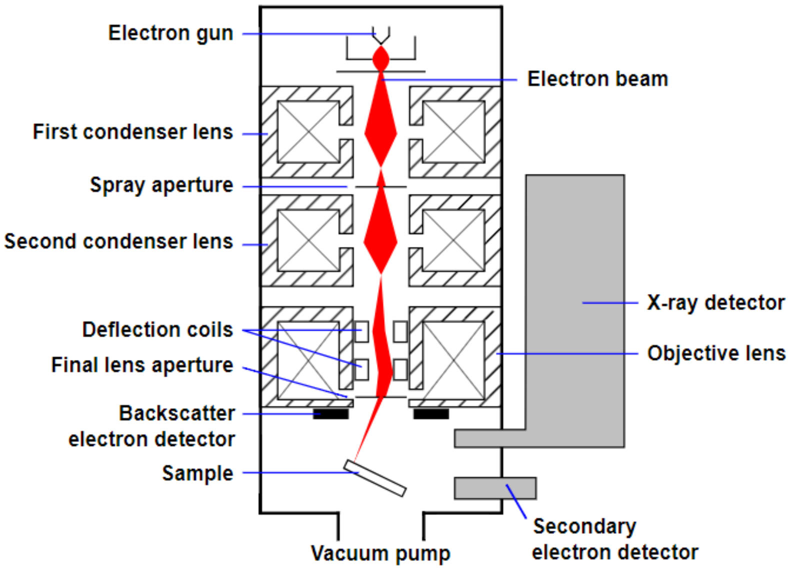

Figure 2.4: SEM apparatus schematic representation. Taken from [63]

The working principle of SEM follows. A monochromatic electron beam is produced by thermionic effect or field emission. These electrons are accelerated to a range from 0 to 30 keV, then they are collimated and deflected via electromagnetic fields, and scanned over a rectangular area of the sample. The collimated beam on the sample origins elastic and inelastic collisions that emit respectively backscattered and secondary electrons. Finally, secondary electrons emitted by the sample are collected by a detector. The scheme of the SEM apparatus is shown in Figure 2.4. The entire procedure requires vacuum (about 10^{-5} mbar) in order to avoid air interference in the process, thus increasing the electron's mean free path and avoiding diffusion phenomena. In conclusion, SEM requires conductive samples such that they can release the charge due to the electron beam.[67]

In this work, two types of detectors were used: the first one is the In-lens detector that is placed in the upper part of the electromagnetic collimator. This detector can achieve higher resolution images since favors the secondary electrons from the upper range of the interaction volume (SE1) and contains direct information on the surface of the sample. On the other hand, the electrons (SE2) collected by the traditional SE detector undergo a longer path. The image acquired using SE2 has less resolution, but it carries more information about the three-dimensionality of the surface.[68] A scheme of this principle is shown in Figure 2.5.

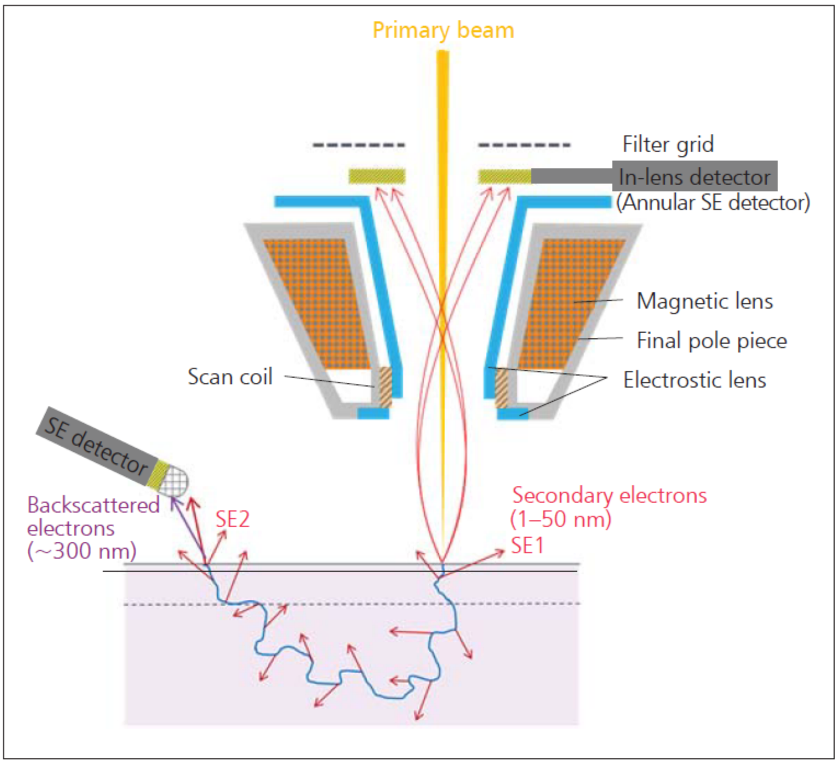

Figure 2.5: Principle of SE signal detection. Taken from [68].

During the process, the impinging beam undergoes many interactions with the material: besides secondary electrons, other signals are produced, such as backscattered electrons, X-Rays, Auger electrons, and Bremsstrahlung emission. These signals can be collected by specific detectors and can be used in different measurement techniques. Collecting the X-Ray radiation, for instance, is the basis of the Energy Dispersive X-Ray Spectroscopy (EDXS) presented below.

In this work a Field Emission Zeiss SEM SUPRA 40 based on a GEMINI column was used to obtain the top surface and cross-section images of the samples. The maximum resolution of the instrument is in the order of some nanometers.

2.2.2. Energy Dispersive X-Ray Spectroscopy

Energy Dispersive X-Ray Spectroscopy exploits the X-Rays emitted by the interaction between the electron beam and the sample. The X-Rays carry qualitative and quantitative information about the elemental composition of the sample. With EDXS, even a micrometric resolution image can be obtained.
The SEM needs an appropriate detector that converts X-Rays into voltage signals. When high-energy electrons collide with an atom, they can tear an inner shell electron from the atom. This missing electron thus leaves a vacancy, and one of the external shell electrons can fill the empty orbital releasing a characteristic X-Ray. The difference between the higher energy level and the initial one is peculiar for each atom, thus it is a footprint for the element itself.[69] It must be specified that the accuracy of the composition measurements is of some percent ($\sim 1\%$), specifically for the low atomic number ($Z<10$) atoms.
For the EDXS in this project, an apparatus for EDS elemental microanalysis (Oxford Instruments) in combination with the AZtec software tool was used.

2.3. Raman Spectroscopy

Raman Spectroscopy is a characterization technique that - using the Raman scattering - gains information about the chemical structures, phases, crystallinity, and molecular interactions of samples.[70] Raman Spectroscopy relies on the inelastic scattering between a monochromatic light beam and the sample. In particular, when a photon interacts with a sample, it can exchange energy with the sample vibrational phonons, so the initial energy of the photon will change and this shift is named as the Raman shift. Since this energy shift originates from the vibrational modes of the sample, it is a unique marker of the chemical and molecular structure.[71] The monochromatic light source is usually a laser in the range of visible, near-infrared, or near-UV. Raman spectroscopy is very versatile and can be used on a variety of samples such as solids, liquids, gases, gels, and powders.

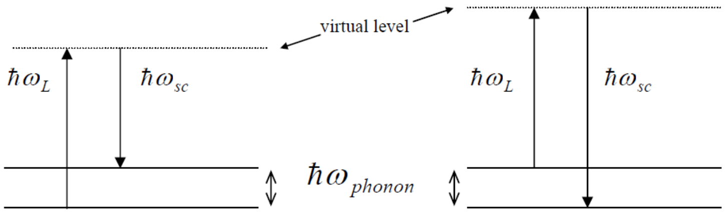

Figure 2.6: Schematic representation of Stokes (left) and anti-Stokes (right) Raman scattering. Taken from [71]

The theory of the Raman effect can be simplified as follow. Suppose that the frequency of the incident light beam is ω_L and that of the reference vibrational mode is ω_j. When the monochromatic light interacts with the target, the most probable event is elastic (Rayleigh) scattering, so most of the photons will maintain constant energy $\hbar\omega_L$. On the other hand, when inelastic scattering occurs, the photon energy is not constant and, after the interaction with the sample phonons, its frequency will be $\omega_{sc} = \omega_L \pm \omega_j$. These frequency shifts are called the Raman shifts.[71]

A simplified quantum theory follows. The energy of the incident photon is $\hbar\omega_L$, and the quantum of energy (phonon) of the vibrational mode is $\hbar\omega_j$. When inelastic scattering occurs, the photon can acquire or lose the vibrational energy $\hbar\omega_j$, so the scattered photon will have energy:

$$\hbar\omega_{sc} = \hbar\omega_L \pm \hbar\omega_j \tag{2.1}$$

A scheme of the process is presented in Figure 2.2. When the energy is lost from the original photon, a Raman Stokes process occurs; on the contrary, when the energy is withdrawn from the sample, a Raman anti-Stokes process takes place. Anti-Stokes lines are always weaker than Stokes ones due to the Bose-Einstein distribution: the vibrational ground state is always more populated than high-energy vibrational states.[72] The population of the energy levels depends on temperature and determines the intensity of Stokes and Anti-Stokes bands, as it is shown in Equation (2.2):

$$\frac{I_{Stokes}}{I_{Anti-Stokes}} = \frac{(\omega_L - \omega_j)^4}{(\omega_L + \omega_j)^4} exp(\frac{\hbar\omega_j}{k_B T}) \tag{2.2}$$

Raman spectroscopy yields results even with crystals, as the scattering occurs with some phonons of the vibrational modes (the optical zone-centered modes) of the crystal itself. Raman spectra of crystals are usually characterized by narrow peaks, however, when the crystallinity is reduced or the material is amorphous, the peaks tend to broaden until they become large bands. This effect is related to the uncertainty of the wave vector of the phonons in the non-infinite crystal size.[71]
In this work, different Raman spectrometers were used:

1. Renishaw InVia micro-Raman spectrometer, equipped with optical microscope. An argon ion source emitting green (514 nm) and blue (457 nm) lasers was used as the excitation source and the laser power at the sample was kept below 2 mW, to avoid laser-induced modifications. The Raman spectra were collected using the 1800 l/mm and 2400 l/mm gratings, respectively, for the green and blue lasers, and with the 50x optical objective.

2. Renishaw InVia micro-Raman spectrometer equipped with a remote Raman probe and optical microscope (50x objective). Two diode-pumped solid-state lasers were employed: 532 nm (green) and 660 nm (red), with 1800 l/mm grating.
3. Some Raman measurements were carried out at the Solid-Liquid Interface Nanomicroscopy and Spectroscopy Lab (SoLINano-Σ) using Sol Confotec NR 500 spectrometer, equipped with a 532 nm solid-state laser, and grating 1800 l/mm.

2.4. UV/Vis/NIR Spectrophotometry

For the characterization of the optical properties of ZMO films, a spectrophotometer was used. A spectrophotometer is an instrument able to measure the intensity of light at different wavelengths. After the light reaches the sample, four components can be distinguished: the fraction of the electromagnetic wave that is diffused reflected R, the fraction transmitted beyond the sample itself T, the fraction absorbed A, and the lost fraction due to scattering phenomena D (diffuse transmittance). These contributions add together to the total radiation:

$$R + T + A + D = 1 \tag{2.3}$$

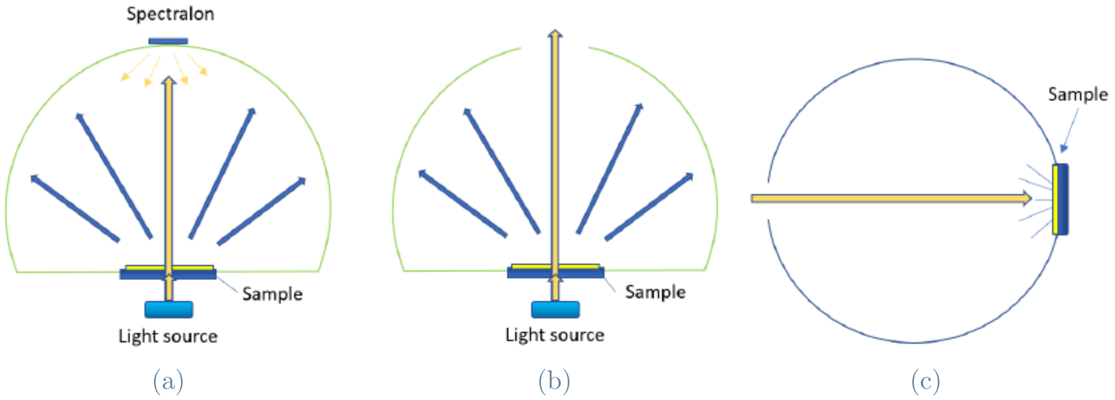

(a) (b) (c)

Figure 2.7: Total transmittance (a), diffused transmittance (b) and diffuse reflectance (c) measurements schemes. Taken from [65].

A scheme for this type of measurement can be described as follows. Three different setups -as schematized in Figure 2.7 - can be used to measure the total and diffused transmittance and the diffuse reflectance.[65] For all these kinds of measurements, the film must be deposited on a transparent substrate as glass. For transmittance measurements, the sample is placed at the entrance of a device known as the integrating sphere with the film facing inside. On the opposite side of the sphere, there is another hole that can be closed by a Spectralon disk (which is a material with about 100% reflection for every wavelength). If the hole is closed, all the light passing through the sample is collected by the sphere and the total transmittance is measured, Figure 2.7a. If, on the other hand, the hole is left open, only the diffused transmittance is measured, since the radiation that is not diffused goes straight through the hole and is lost, Figure 2.7b. T_{tot} is not the transmittance T in Equation (2.3), T_{tot} is the sum of the direct transmittance and the diffused transmittance. In conclusion, to measure the diffuse reflectance, the same hole is closed by the sample with the film facing the sphere and the radiation impinging on its surface, Figure 2.7c. The effect of the substrate must be taken into account, so the measurements are normalized to obtain the real film information following the relations below.[65]

$$T_{film} = \frac{T_{tot}}{T_{glass}}, \tag{2.4}$$

$$R_{film} = R_{tot} - (R_{glass} * T_{film}^2). \tag{2.5}$$

Most of the transmittance measurements were recorded via a UV-1800 UV-VIS Shimadzu spectrophotometer within the wavelength range 190-1100 nm and with data scanned every 0.2 nm. The absence of the integrating sphere may contribute to an underestimation of transmittance values, since just light reaching the detector placed behind and perpendicular to the sample surface can be collected and the diffused contribution is lost. For more accurate optical measurements, the instrument at the Italian Institute of Technology (CNST-IIT) was used: Lambda 1050 UV/VIS/NIR spectrophotometer with Perkin Elmer 150 mm integrating sphere coated by Spectralon (250-2000 nm range, 2nm interval).

2.5. Electrochemical techniques

In the following sections, electrochemical techniques used in this work will be presented. The following techniques are adopted for the initial study of the ZMO electrodes produced during this work, to try to understand the basic operating principles and the redox mechanism of the material.

2.5.1. Cyclic Voltammetry

The Cyclic Voltammetry technique (CV) records the current response at different applied voltages. In a typical 3-electrode configuration, an external potentiostat imposes the voltage with respect to the reference electrode - which remains at constant potential during measurements - and measures the current circulating between the working electrode (in our case, the ZMO film) and the counter electrode. This technique provides information about the voltage and energy profiles (being the energy the integral product between current and potential) of the tested material. It has to be noticed that this measure is performed in a non-equilibrium state.[7]

CV technique is one of the most relevant techniques for electrochemical measurements. The typical mode used -even in this work- is the linear scan CV, in which the potential goes from one extreme to the other following an increasing/decreasing linear path, as shown in Figure 2.8.a. The physical model of the processes involved is quite complicated, varies from case to case, and falls outside the interests of this thesis. The actual process involves solid-liquid interface phenomena, ion diffusion in the electrolyte and in the electrode, and multiple reactions, which are far beyond the analysis of this technique. Practically, it is important to identify some specific values of relevance in the CV curve.[7]

For the measure, we need to determine the terminal voltages and the scan rate. The terminal voltages are the extremes of the scan in which the potentiostat spans, and, as mentioned before, are set with respect to the reference electrode. Same potential values have different numerical values if related to different reference electrodes, and if the reference changes all the values have to be recalibrated on the new one. The scan rate refers to the velocity of the scan, that is how fast the imposed voltage goes from one extreme to the other. Both the parameters have to be chosen wisely. First, terminal voltages limit the reactions that can occur in the system. If some reactions are expected or want to be measured, the voltage range (electrochemical window) must be properly selected not to exclude them, and to avoid unwanted reactions such as electrolyte decomposition, gas evolution, and electrode side reactions. Secondly, the scan rate cannot be too fast, otherwise the reaction will not occur. The scan rate is usually in the order of 0.1-10 mV/s which is quite slow. However, limited measurement time, equipment detection limit, and the fact that when the scan rate is too slow the limiting factor is not the charge carriers diffusion, they normally make very slow scan rates unfeasible.[7]

To verify that the scan rate is appropriate, one method is to measure how close the experimental integral capacity is to the theoretical one. Once the scan rate and the voltage extremes are set, the CV measurement is ready to start, and the corresponding triangle voltage is applied many times as the cycles wanted. See Figure 2.8.a.

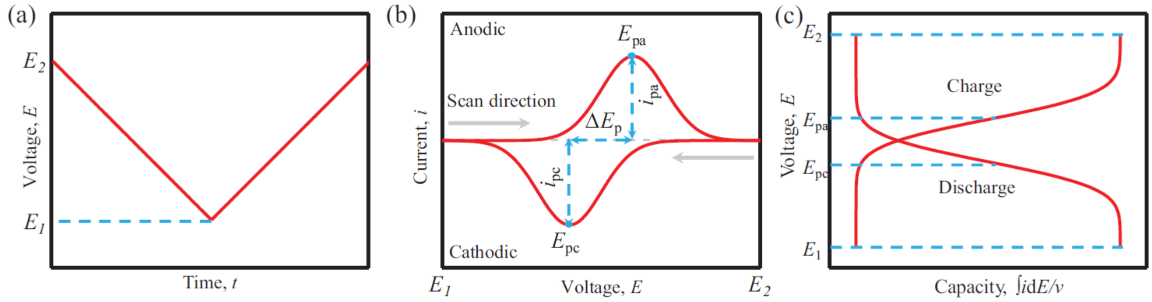

Figure 2.8: a) Voltage profile applied in a CV measurement, b) current response versus voltage curves and c) voltage versus integral current curves. Taken from [7].

In Figure 2.8.b, the typical CV curve for battery electrodes is shown. As can be seen, we obtain one gaussian type peak for each reaction, from which current peak and peak voltage can be identified. The upper part of the CV plot in Figure 2.8.b is called anodic, where the current is positive, and oxidation occurs. The cathodic zone is the bottom part, where the current is negative and reduction occurs. The anodic part of the curve is also associated with charging while the cathodic is associated with discharging, as can be seen in Figure 2.8.c.

Another way to better understand the main mechanisms undergoing during the CV is to divide the measured current into two categories: faradaic current - which is generated from electrochemical reactions - and one associated with the double layer which depends only on capacity and scan rate. The double-layer phenomenon is not related to chemical processes, but just to a physical mechanism. Faradaic current implies an exchange of charges between electrode and electrolyte, while a non-faradaic process is based on the accumulation of ions in the proximity of the electrode to counterbalance the incoming charges, as shown in Figure 2.9. Faradaic current can be further divided into surface and bulk contributions, which have different behaviors. In conclusion, reaction kinetics is another electrode characteristic to be considered. The scan rate, for instance, has to be tuned with respect to the reaction kinetics in a way to let the time for the reactions to occur completely and exchange all the charges. In order to increase the reaction kinetics, nanomaterials are, more and more, exploited as electrodes. Nanomaterials have a large surface area that allows rapid diffusion current response. This is one of the main reasons why this work is focused on morphology analysis and nanostructured thin films as electrodes.

The potentiostat used in the electrochemical measurements in this thesis is the PalmSens4 potentiostat/galvanostat/impedance analyzer, with ±10 V potential range, and a maximum current of 30 mA.

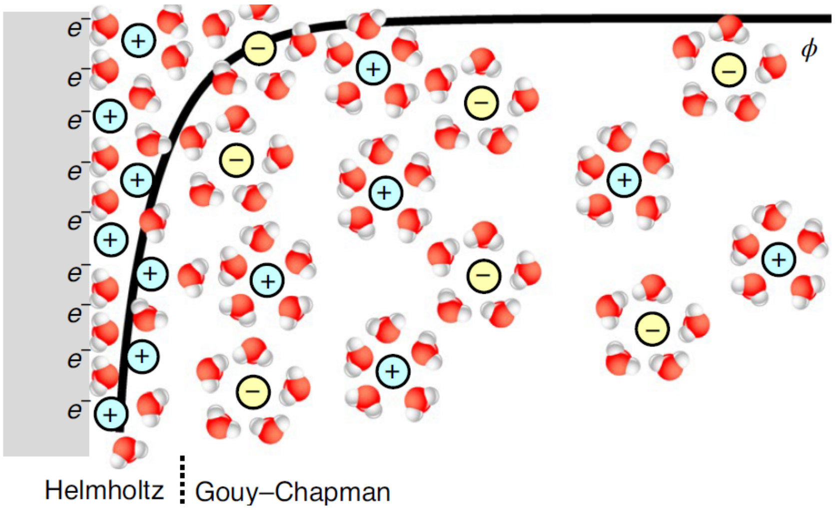

Figure 2.9: Schematic solid–liquid electrochemical interface. At a solid–liquid interface, the double layer is formed when excess electrons on the solid electrode are balanced by an increased density of solvated positive ions in the electrolyte. ϕ is the electrostatic potential. Taken from [73]

2.5.2. Potentiostatic techniques

Thanks to CV, one is able to determine in which range of potentials the main reactions occur and where are the peak voltages. Once the range in which the reaction takes place has been determined, one might want to trigger the reaction and maintain the condition until the reaction ends. Potentiostatic (PS) measurements will be used in this work for this purpose, to promote a reaction and then perform analyses on the sample after the reaction fades.

As we discussed above in Subsection 2.5.1, if the scan rate is not slow enough, some reactants may not undergo electrochemistry, leaving the sample half processed and half pristine. Using PS, we can maintain the voltage until the whole sample is electrochemically processed, so until the current goes to zero. If the current is zero, one can assume that the charges are no longer exchanged, and all the reactions have been completed at that selected potential value.

3 Synthesis and structural characterization of as-deposited ZMO films

This chapter aims to describe the target and the PLD parameters used for the synthesis, then it presents the morphology and stoichiometric properties of the films produced and their relationship with the synthesis parameters adopted. The Raman analysis will show that the produced films are amorphous, thus they will require thermal treatment to crystalize in the ZMO structure discussed in Chapter 1.

3.1. The ZMO target

The material I have used to produce the ZMO films is a $ZnO : Mn_2O_3$ (1:1 mol%), hot-pressed, 99.99% purity, 1" x 6mm cylinder target supplied by Testbourne B.V. Figure 3.1a shows the target before the sessions of deposition. As can be seen, it presents many orange-like particles in a darker matrix. Figure 3.2a presents a SEM characterization of the target morphology. The surface is rough, with different textures and depressions. At higher magnifications, the target assumes a cobbled texture. Figure 3.2b shows the

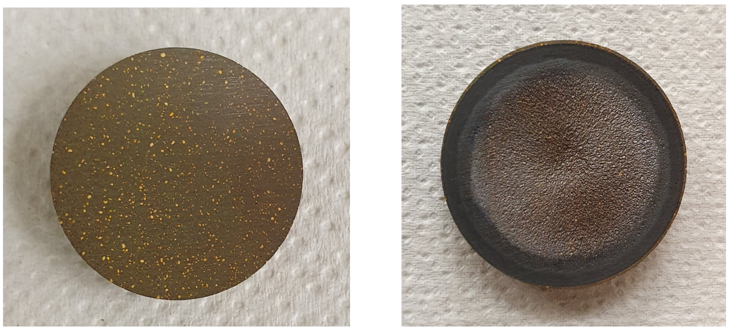
(a) (b)

Figure 3.1: ZMO target before the deposition sessions (a) and after some depositions (b)

edge between the matrix and the particle. It can be seen that the surface of the matrix, on the left, has larger grains compared to the particle, on the right. Relying on EDXS mapping, it is possible to ascertain that those depression spots are ZnO particles, and they are also the orange dots visible in Figure 3.1a on the target. As it can be seen in the map (Figure 3.2d), the depression zones are rich in Zn, while the remaining matrix is rich in Mn (Figure 3.2e). Oxygen is present all across the target (Figure 3.2f). The EDXS spectra output the atomic percentage in different points: the elemental results on the orange particles are 44.56% O, 9.14% Mn, and 46.30% Zn, while on the background matrix are 42.92% O, 40.69% Mn, and 16.40% Zn. The Raman spectra were taken both on the matrix and the orange-like particles, using a 514 nm and a 660 nm laser excitation (0.4 mW), respectively. The last ones present the spectrum shown in Figure 3.2h, which is assigned to ZnO.[74] On the other hand, the matrix spectrum is characterized by a band between 500 and 600 cm^{-1}, typical of the amorphous Mn-oxides or MnO (Figure 3.2g).[75]

3.2. PLD parameters

In this section, I analyze the PLD parameters used in the synthesis of the films and I show qualitatively the dependence of the deposition rate on the deposition pressure and fluence. First of all, by varying the fluence and oxygen pressure, I proceeded to measure their influence on the deposition of ZMO, in order to trace the trends to know how to deal with the subsequent deposition sessions, for example how to obtain a certain morphology and the deposition time necessary to get a certain thickness. Oxygen pressure values equal to "vacuum" ($\sim$3-4x10^{-3}Pa), and 1 Pa, 10 Pa, 50 Pa, and 100 Pa were chosen, with constant deposition time of 15 minutes, and the fluence values were varied between a low value ($\sim$2.2 J/cm^2), a middle one ($\sim$3.8 J/cm^2) and a high one ($\sim$6 J/cm^2) by changing the laser energy at constant laser spot size on the target ($\sim$6 mm^2). Table 3.1 shows the trends divided by oxygen pressures. It can be seen how, increasing the fluence, the deposition rate increases. On the other hand, no clear trend as a function of pressure is observed. Actually, although PLD-deposited films generally expand (due to higher porosity) as gas pressure increases (see Section 2.1), the particles ablated by the target undergo more collisions at higher gas pressure and deviate from the path, thus spreading over a larger substrate area, so the deposition rate does not necessarily increase. Subsequent depositions were conducted not only in vacuum ($\sim$3-5x10^{-3} Pa) and oxygen, but also in argon and mixture of argon-oxygen, at specific conditions (see Section 3.3), to evaluate effect of gas type on morphology and stoichiometry. The target-substrate distance ($d_{ts} = 5$ cm) and the position of the focusing lens of the optical path were kept

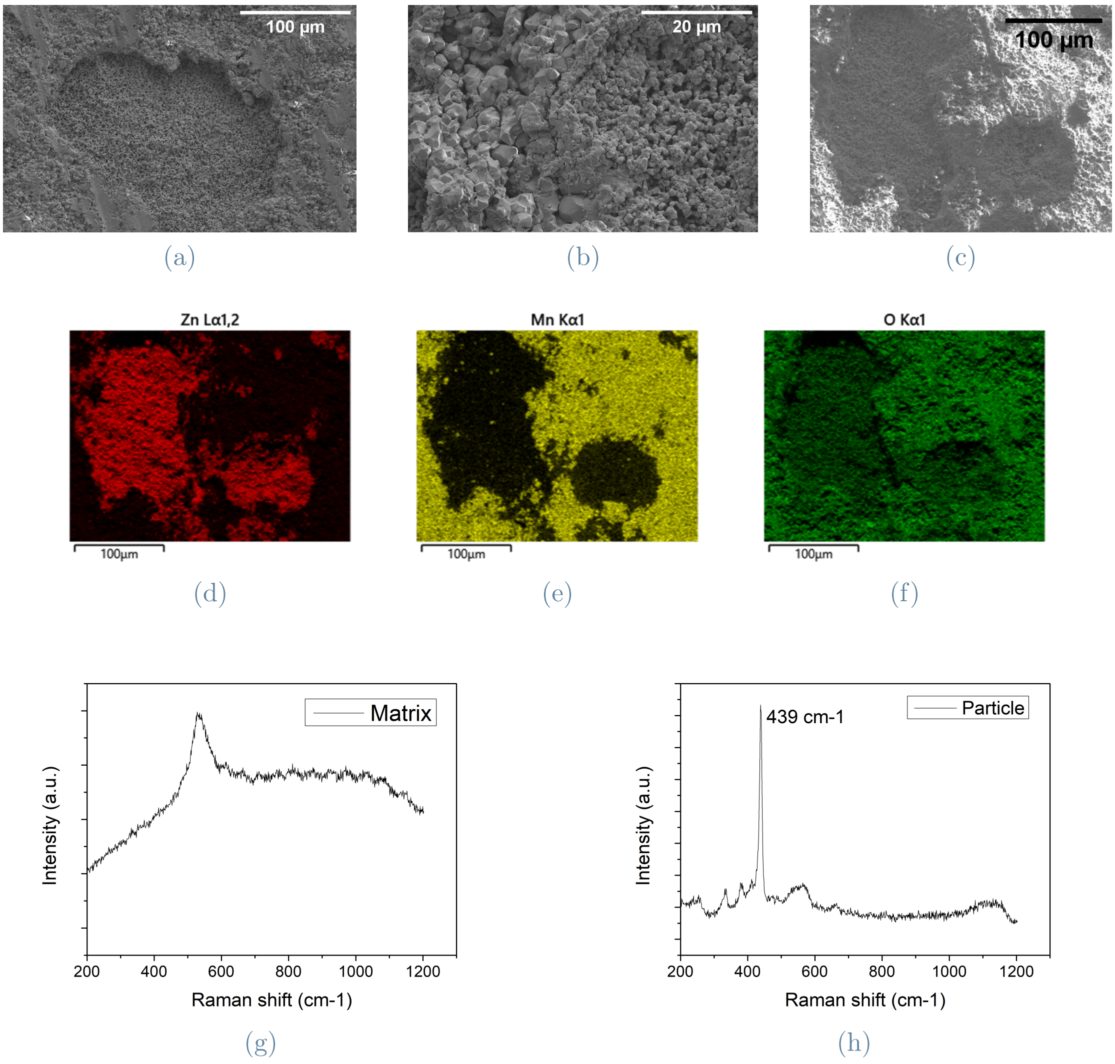

Figure 3.2: ZMO target characterization. (a,b) SEM images; (c,d,e,f) SEM image and further EDXS map characterizations; (g,h) Raman spectra on the matrix and the particle, respectively.

constant for all depositions. An evaluation of how and to what extent the uniformity of the film could be increased was also performed by misaligning the target and the substrate. The deposition time was adjusted depending on the deposition rate at any pressure and fluence to obtain the desired thickness. Finally, it should be emphasized that different types of substrates were used, in fact, for the optical measurements it was necessary to deposit the film on glass, while for the electrochemical measurements, as explained in Chapter 5, it was necessary to deposit on conductive FTO-coated glass. Samples that were characterized only with SEM, EDXS, and Raman spectroscopy were deposited on silicon.

O_2 Pressure [Pa]	Fluence [J/cm^2]	Deposition rate [nm/min]
Vacuum	2.18	33
	3.76	46
	5.87	64
1 Pa	2.17	40
	3.86	67
	6.03	87
10 Pa	2.19	43
	3.78	87
	6.22	187
50 Pa	2.16	100
	3.94	207
	6.1	307
100 Pa	2.22	127
	3.76	173

Table 3.1: Deposition rates for different oxygen pressures (vacuum, 1 Pa, 10 Pa, 50 Pa, and 100 Pa) and different fluences.

3.3. Morphology and stoichiometry characterization

In this section, I present detailed analysis about the effects of the oxygen deposition pressure on film morphology and stoichiometry. Figure 3.3 shows the SEM images of films' cross-sections for the various fluences and oxygen pressures used. In general, the film becomes more compact as the fluence increases. The sample with high fluence and pressure of 100 Pa is missing; in fact, such high fluence for high pressures results in adhesion problems, and crack. This behavior is already noticeable for the sample at 50 Pa and 6 J/cm^2, where the lower part of the image shows the detachment of the film from the silicon substrate and the presence of defects (Figure 3.4). At the end of the analysis concerning the fluence parameter, the fluence was maintained at 3.8 J/cm^2 for the other films' deposition.

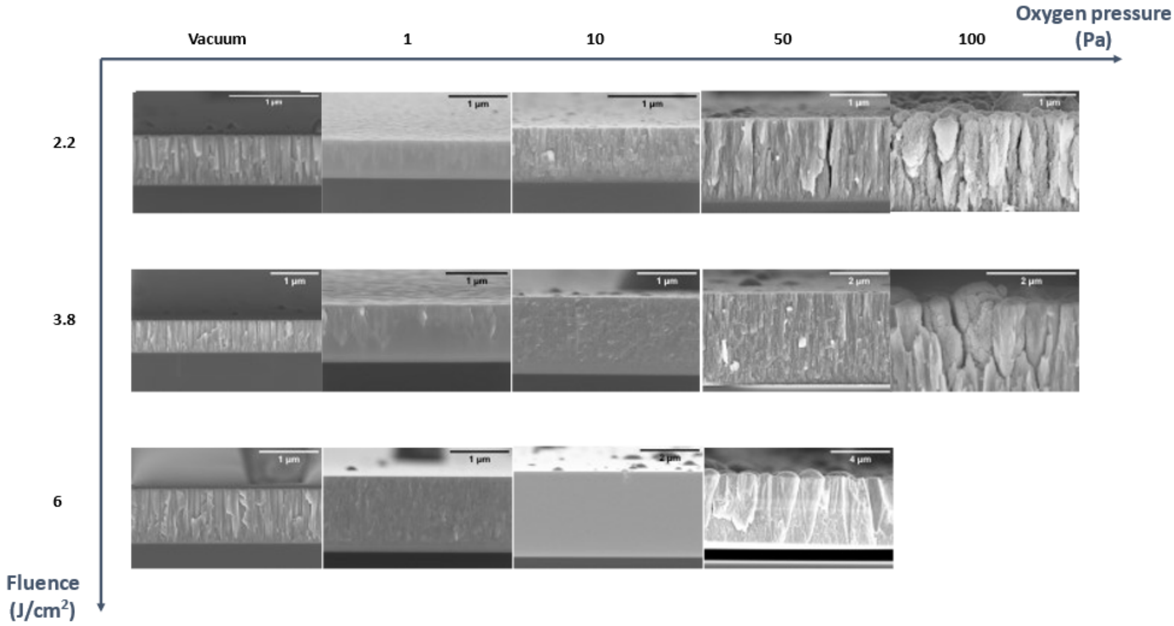

Figure 3.3: Cross-sectional SEM images of films deposited at different oxygen pressures and laser fluences.

Looking at the morphologies of the depositions (fluence set at 3.8 J/cm^2), it can be seen that, as the pressure of O_2 increases (see Figures 3.5 from b to h), the film loses its compactness and the nanoporosity increases, acquiring, for the samples from 70 Pa (Figure 3.5f) onwards, a tendency to develop “tree-like” structures. The higher pressures, therefore, show an overall structure like a "cypress nano-forest", which is typical of PLD-grown oxides (Figure 3.6). The sample deposited in vacuum, in terms of morphology, turns out to be an outlier in the pattern defined above. Interestingly, the sample deposited in vacuum exhibits a columnar structure different from that of films deposited at 1 and 10 Pa and more similar to the one deposited at 30 Pa. However, the film produced in vacuum is denser, since its thickness is reduced at constant deposition time. Probably, this discrepancy is due to a coupling between the effect of the pressure in the chamber and the reactivity of the background gas, altering the stoichiometry. To try to decouple the

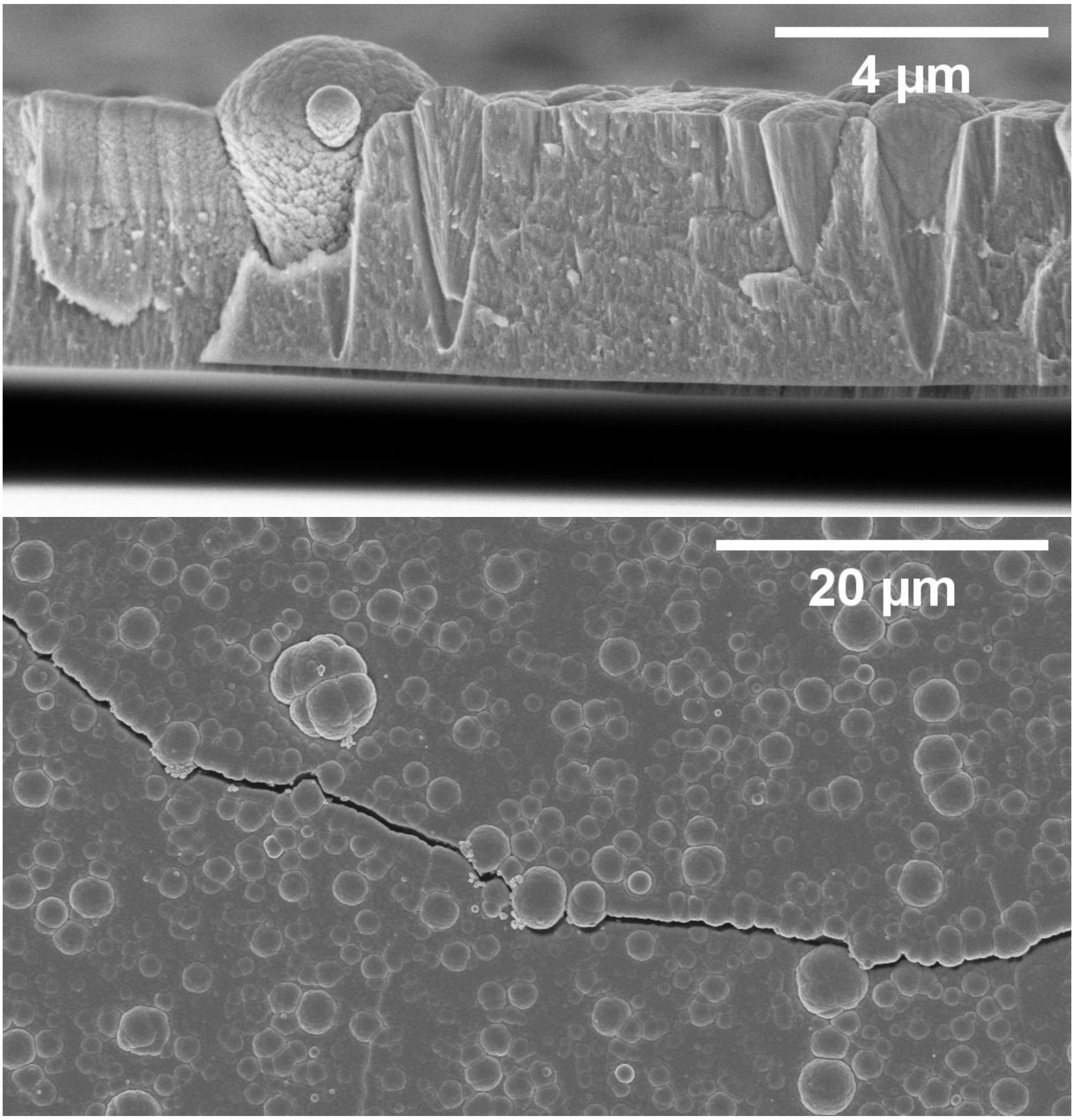

Figure 3.4: Cross sectional and top view SEM images of deposited films at 50 Pa oxygen pressures and 6 J/cm^2 laser fluence.

two effects, some tests of deposition in argon and mixtures of argon and oxygen at 10 Pa and 3.8 J/cm^2 fluence have been conducted and are presented below. The stoichiometry of the samples was measured by EDXS for films deposited at constant fluence of 3.8 J/cm^2 in vacuum and various oxygen pressures (1-150 Pa). It should be considered that the EDX spectra were recorded for each sample over several zones and then averaged between them to get a statistical indication. For the correct quantification of the Zn element, it was necessary to use high-energy electrons (15 keV), thus more penetrating into the sample. In addition, the film thickness is not homogeneous over the whole sample, so in some spectra, the silicon substrate signal was not negligible. It should be kept in mind that the automatic renormalization performed by the EDXS software after the exclusion of an element could lower the accuracy of the measurement, especially for low-Z elements like oxygen. Figure 3.7 shows the percentage trends of the elemental compositions of the films. Films deposited in vacuum or at low O_2 pressures (<10 Pa) are poor in oxygen and have a higher content of Zn and Mn. The trend as a function of the pressure reaches a plateau where the stoichiometry stabilizes and becomes constant irrespective of oxygen pressures. For comparison, dashed lines indicating the theoretical stoichiometry of $ZnMn_2O_4$ (14.29% Zn, 28.57% Mn, 57.14% O) have been inserted in the plot. For the films deposited in vacuum and at 1 Pa, the oxygen is sub-stoichiometric, while the Mn is super-stoichiometric, while at higher pressure the conditions are reversed: this trend could indicate a change of Mn oxidation state towards a more oxidized form as the oxygen pressure increases. The Zn content always remains sub-stoichiometric.

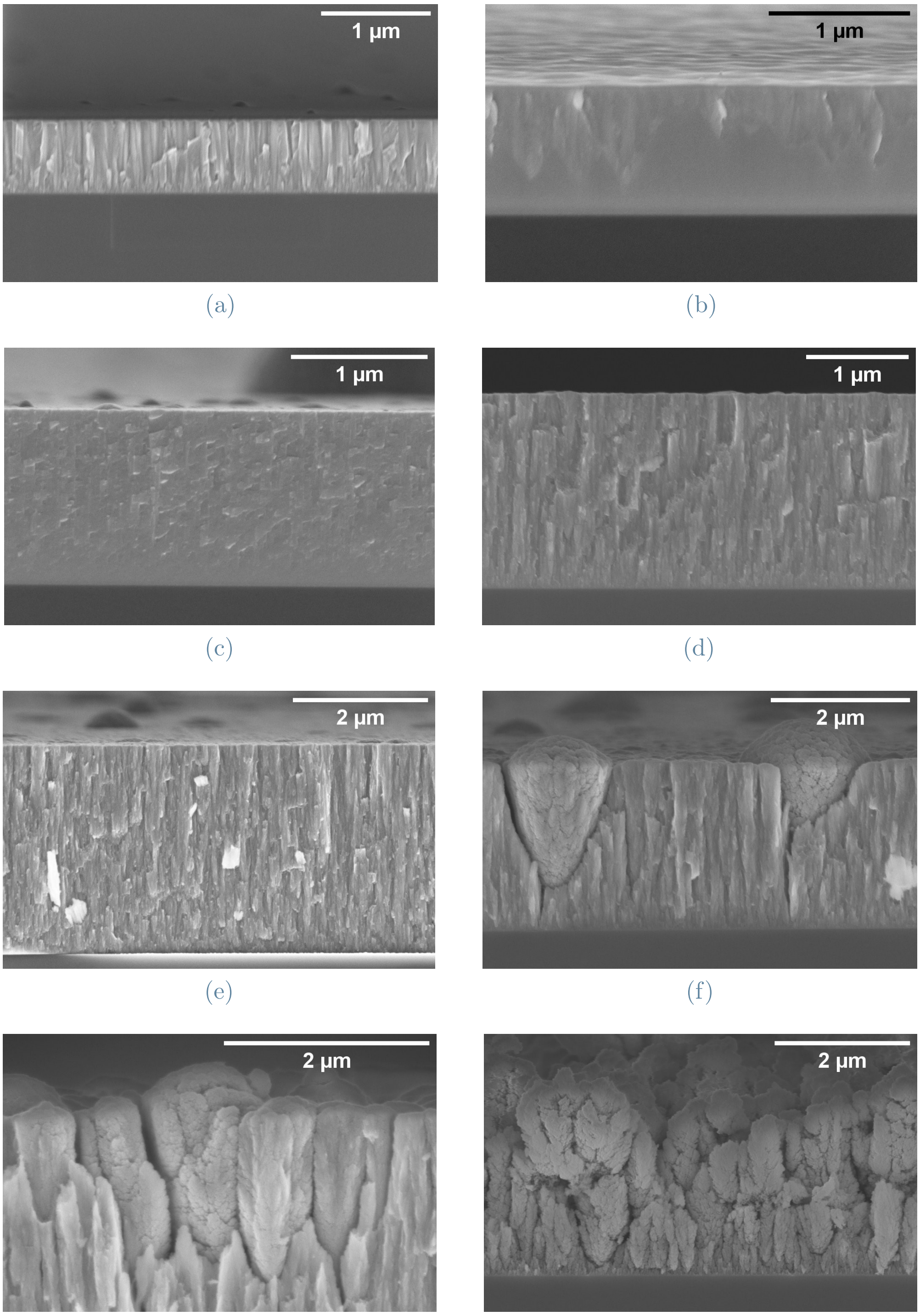

(a) (b) (c) (d) (e) (f) (g) (h)

Figure 3.5: ZMO as-deposited films by increasing background oxygen pressure at 3.8 J/cm^2 fluence. (a) Vacuum, (b) 1 Pa, (c) 10 Pa, (d) 30 Pa, (e) 50 Pa, (f) 70, (g) 100 Pa, and (h) 150 Pa.

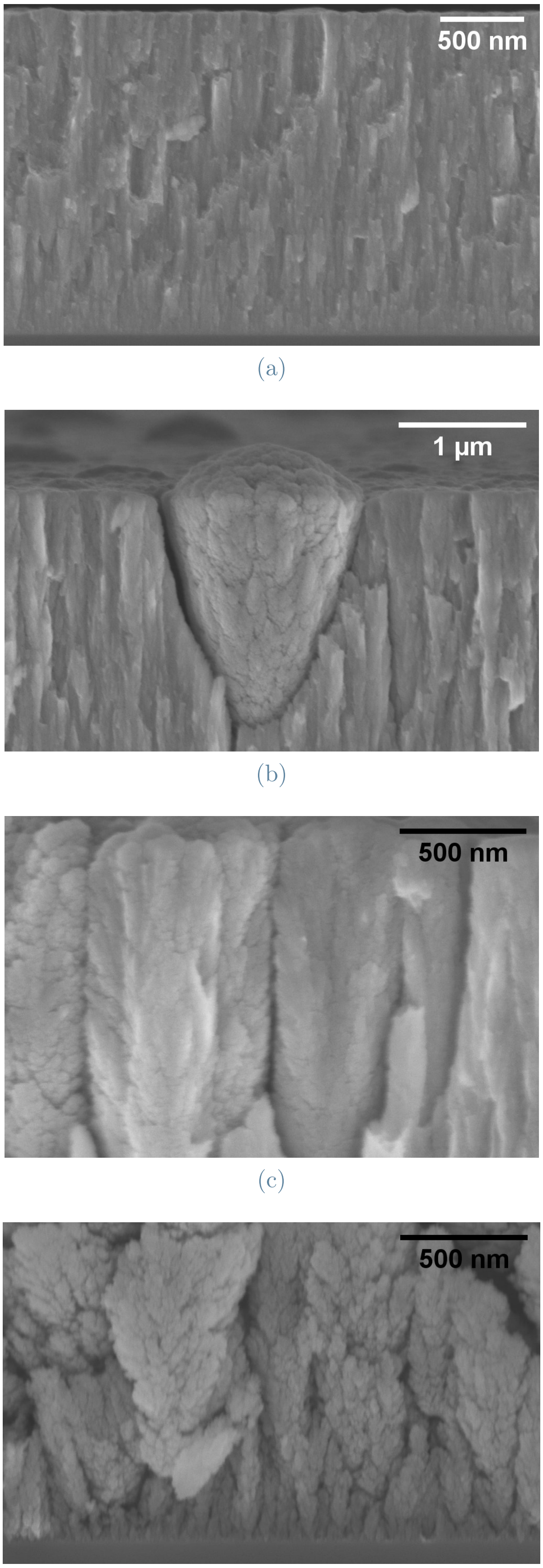

(a)

(b)

(c)

(d)

Figure 3.6: SEM higher magnifications of ZMO films deposited at 30, 70, 100, and 150 Pa of oxygen, respectively, at 3.8 J/cm^2 laser fluence.

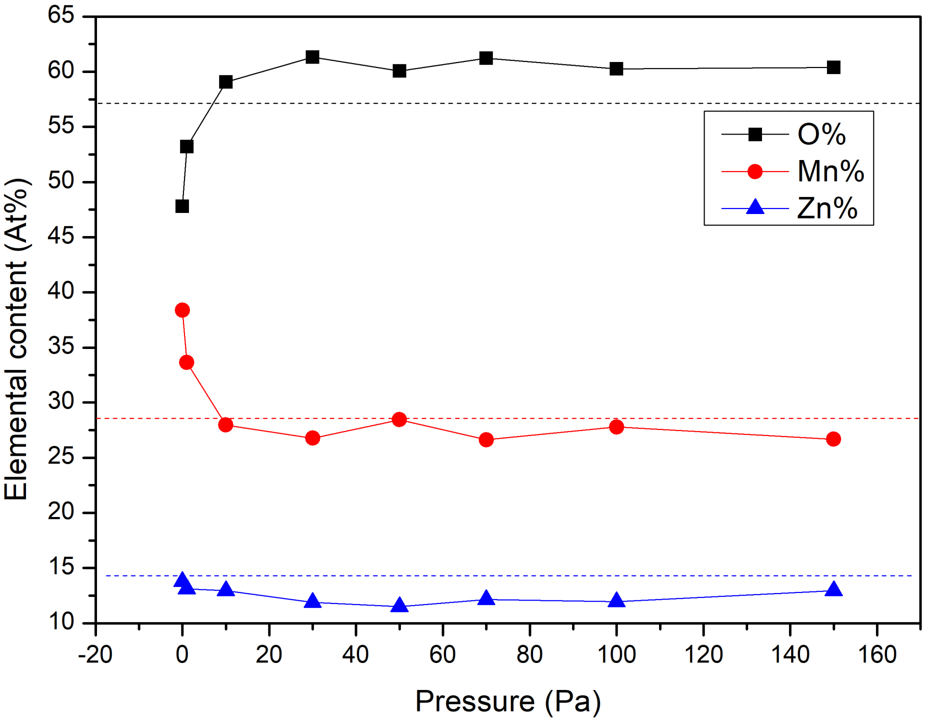

Figure 3.7: Elemental content in atomic percentage of the films at different oxygen deposition pressures, as obtained by EDXS measurements.

In order to evaluate the effect of the type of gas on film morphology and stoichiometry, I fixed the deposition pressure and fluence (10 Pa and 3.8 J/cm^2) and I varied the relative amount of oxygen and argon: 100% O_2, Ar:O_2 2:1, Ar:O_2 5:1, Ar:O_2 9:1, and 100% Ar (Figure 3.8). In particular, the deposition in pure argon atmosphere, an inert gas, shows a columnar morphology similar to the one of the film deposited in vacuum (Figure 3.8e). There can be two explanations:

- It can be assumed that stoichiometry alone influences the morphology, and even with a small amount of oxygen the columnar aspect of the film is reduced. Even looking at the films deposited in the $Ar - O_2$ mixture, it can be seen that, as long as the atmosphere is not totally devoid of oxygen, the morphology is not "columnar-like" and resembles that of pure oxygen (from 3.8a to 3.8d). Furthermore, the stoichiometry of the film deposited in pure argon (for 10 Pa: 51.76% O, 33.61% Mn, and 14.63% Zn) has an oxygen content lower than that at 1 Pa of oxygen and approaches that of the vacuum deposition.
- The other possibility is that it is not directly, or only, stoichiometry that influences

the final morphology and that there are other factors. Actually, the stoichiometry of the sample in Ar has a slightly higher oxygen content compared to the sample deposited in vacuum (so it has some "exceeding oxygen"), despite the similarity in morphology. For example, the difference in the collisional cross-section of Ar and O_2 for the ablated particles could be a determining factor in the process. In addition, the fact that oxygen is reactive and argon is not can change the energy of the ablated species.

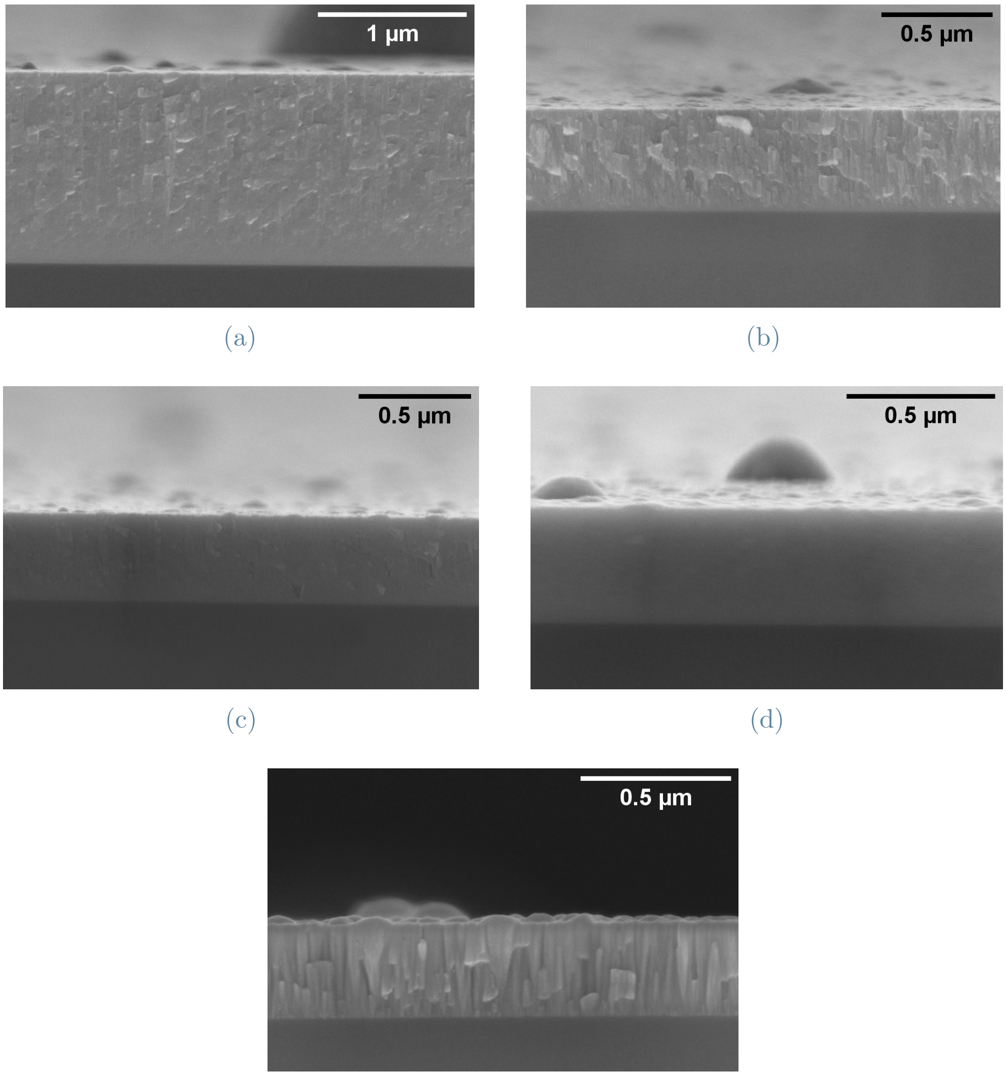

(a) (b) (c) (d) (e)

Figure 3.8: Cross-sectional SEM images of ZMO films deposited in 10 Pa of: (a) 100% O_2, (b) Ar:O_2 2:1, (c) Ar:O_2 5:1, (d) Ar:O_2 9:1, and (e) 100% Ar.

3.4. As-deposited ZMO Raman analysis

Raman spectra of as-deposited ZMO films produced at various oxygen pressures and 3.8 J/cm^2 fluence are shown in Figure 3.9. The spectra shown correspond to the films deposited on silicon and analyzed with a red excitation source laser (660 nm). All the spectra consist of broad bands centered around 600-650 cm^{-1}, similar to those of amorphous manganese oxides. In the case of highly thin films, such as 1 Pa, the characteristic silicon peak (520.7 cm^{-1}) is visible in the spectrum. It can be seen that the band of the film deposited in 1 Pa oxygen differs from the others. Indeed, it is red-shifted, less broad, and the spectra of samples deposited at higher oxygen pressure appear to have a shoulder around 500 cm^{-1} that is missing in the spectrum of the sample deposited at 1 Pa. The vacuum-deposited film's spectrum is not shown in Figure 3.9 because the silicon signal dominates it.

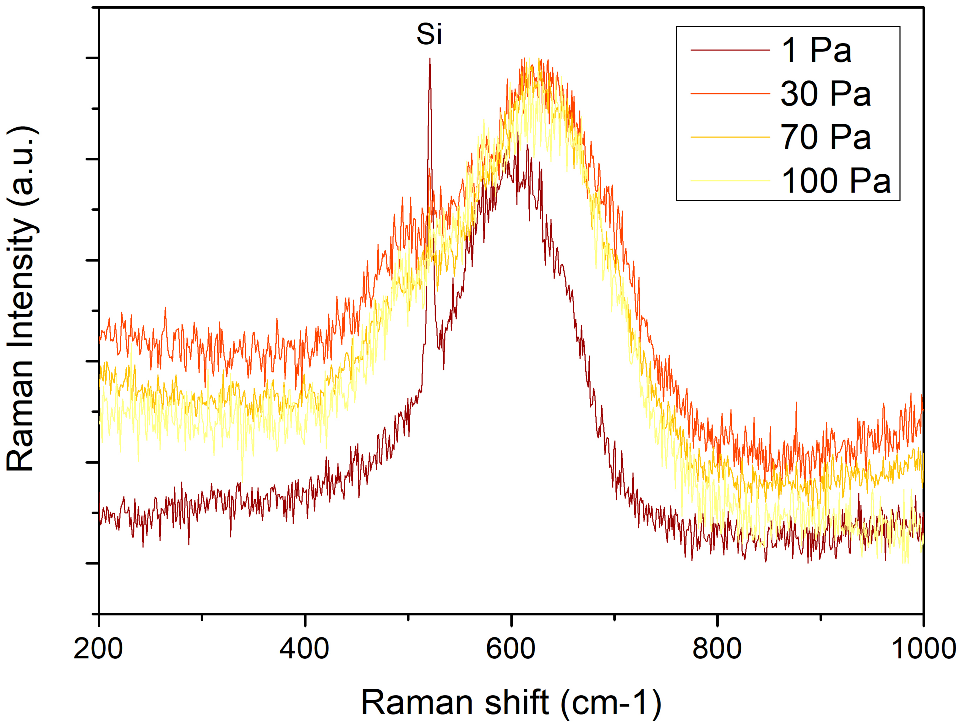

Figure 3.9: Raman spectra of films deposited at 1 Pa, 30 Pa, 70 Pa, and 100 Pa of oxygen on silicon (Laser: wavelength 660 nm, power 0.75 mW).

3.5. Summary

The morphologies of the films deposited in oxygen vary from the most compact to the most porous ones. From the electrochemical point of view, it has been described in Section 1.5.3 how a porous structure, with a nanostructured morphology, can help to alleviate the mechanical stress effects that the crystal undergoes during the intercalation/deintercalation of the zinc and how it can increase the interface area with the electrolyte. The proper balance must be found between a porous and a compact structure; in fact, a structure that is too porous risks having poor mechanical properties and low adhesion. Moreover, concerning stoichiometry, it has been shown how a different pressure can vary the elemental composition of the material; in particular, the manganese in films deposited in oxygen atmospheres $\geq$10 Pa remains slightly sub-stoichiometric, which many articles claim to be a favourable condition [31, 47] (see Section 1.5.3). Finally, the films discussed in this chapter are amorphous (as the Raman spectra confirm) and do not have the crystalline structure described in Section 1.5. The analyses in the following chapter, instead, were performed on samples subjected to heat treatments to promote their crystallization.

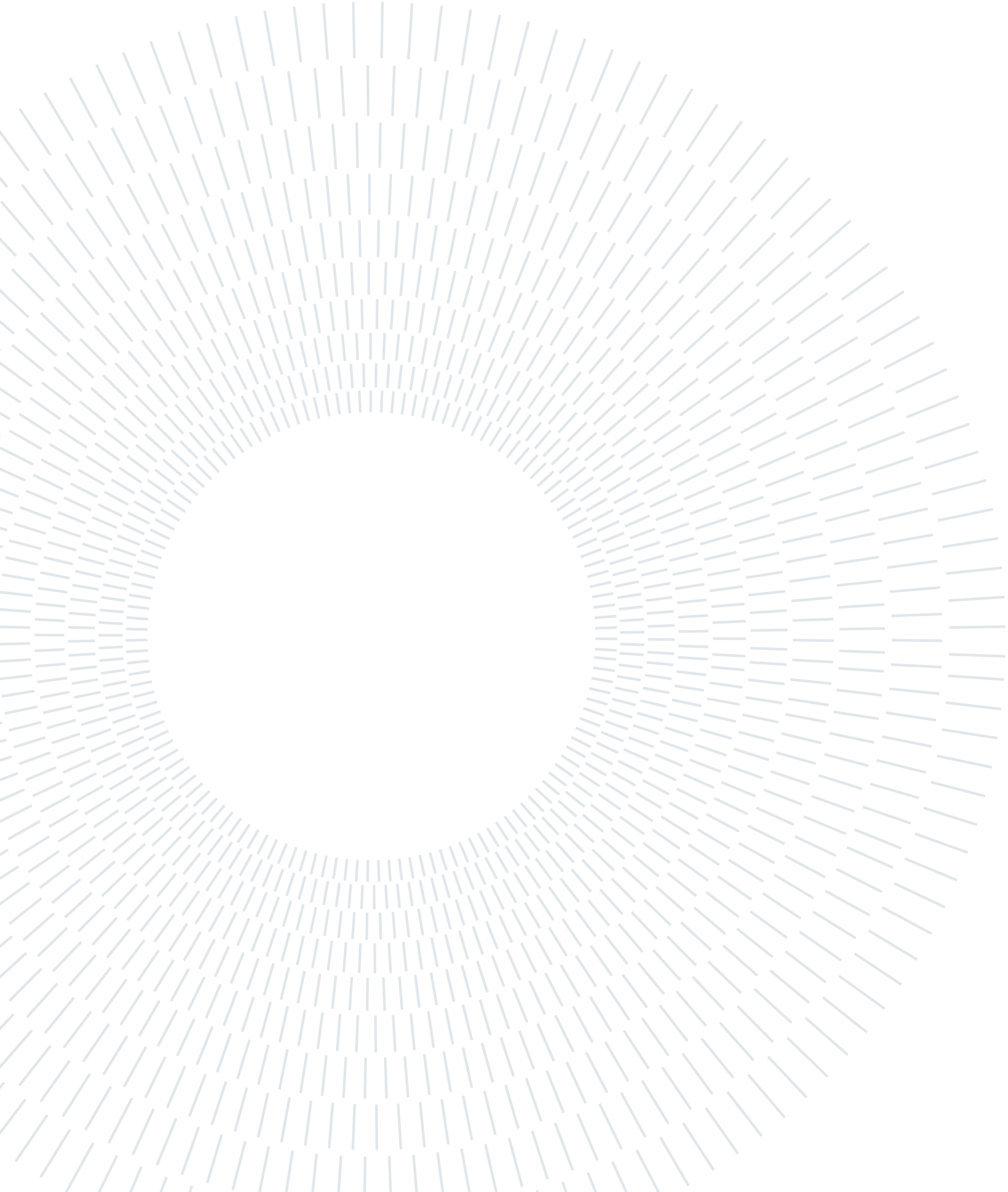

4 | Crystallization of ZMO films by thermal annealing

This chapter presents the study carried out on annealed samples. As mentioned in the previous chapter, the pristine films obtained by PLD are amorphous. Raman spectroscopy was the technique used to check whether the samples, after annealing, crystallized. Therefore, the first section will present the state of the art of Raman spectroscopy of ZMO. The second section will expose annealing parameters and focus on the effect that different temperatures induce on Raman spectra, stoichiometry, and morphology. The third section will again focus on the Raman spectra, stoichiometry, and morphology, but this time will evaluate these aspects in relation to the deposition oxygen pressure, keeping annealing conditions constant. Also in the third section, a comparison between as-deposited and annealed films is presented. Finally, the last section will present optical measurements made on crystalline ZMO films.

4.1. Raman spectroscopy of ZMO: state of the art

In this section, I want to present the state of the art in the analysis of the Raman spectroscopy of ZMO. First of all, it should be clarified that attribution of the Raman peaks is still not unique and conflicting assignations are found in different papers. The group analysis for a crystal belonging to the $I4_1/amd$ space group predicts 10 Raman-active modes as follows:

$$\Gamma = 2A_{1g} + 3B_{1g} + B_{2g} + 4E_g \tag{4.1}$$

Experimentally, 9 modes are visible: 170 cm^{-1}, 300 cm^{-1}, 322 cm^{-1}, 366 cm^{-1}, 377 cm^{-1}, 477 cm^{-1}, 587 cm^{-1}, 630 cm^{-1} and 678 cm^{-1}.[76] Some of these modes are weak and difficult to detect or isolate from background noise. These weak modes are: 170 cm^{-1}, 477 cm^{-1} and 587 cm^{-1}. Moreover, other peaks (300 cm^{-1}, 366 cm^{-1}, and 630 cm^{-1}) approach a nearest intense peak and become shoulders, not being properly distinguishable anymore. Therefore, the main peaks used as a reference, also in my work, remain three: the peak at 322 cm^{-1}, the one at 377 cm^{-1}, and finally the one at 678 cm^{-1}. Figure 4.1a,

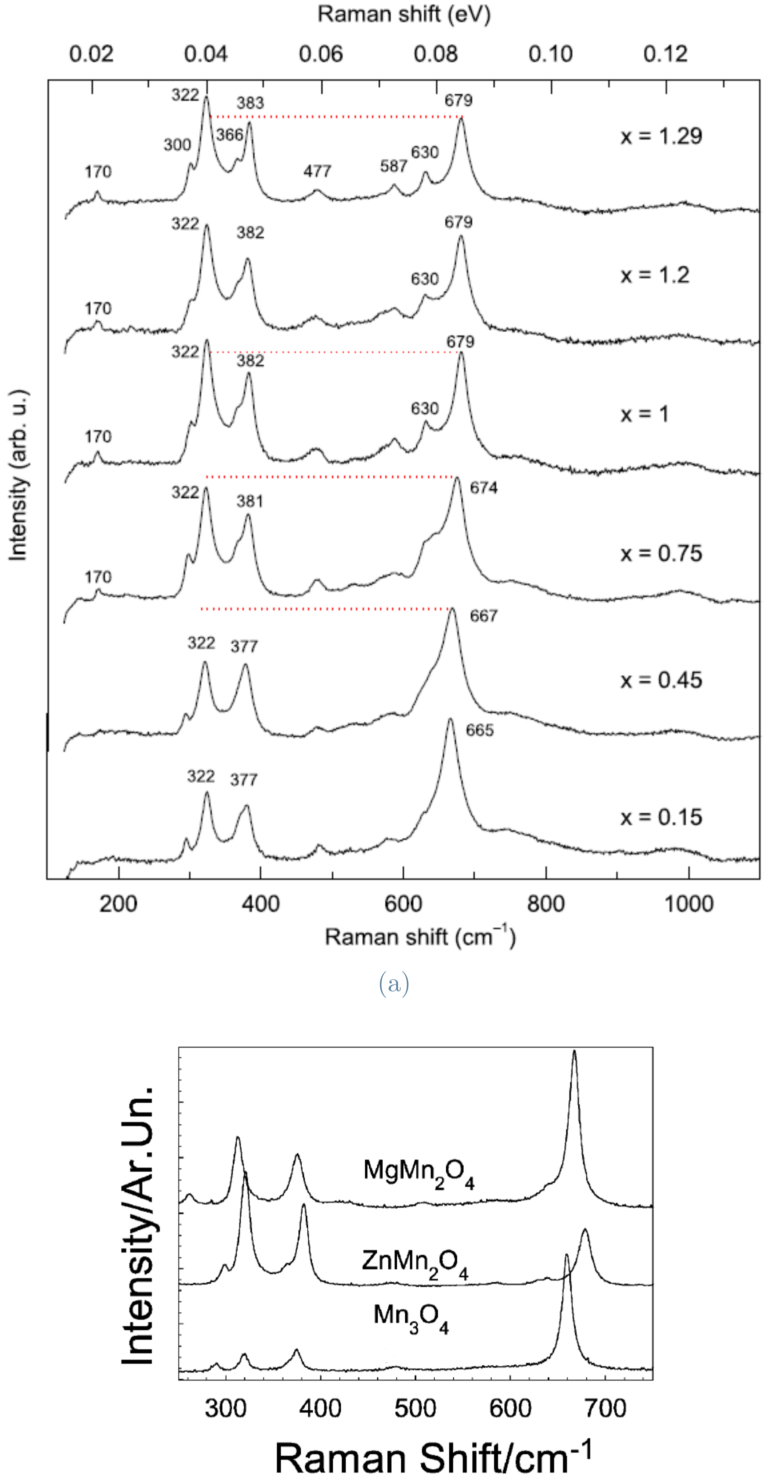

(a)

(b)

Figure 4.1: (a) Raman spectra of $Zn_xMn_{3-x}O_4$ for x=0.15–1.29 taken from [76]. (b) Raman spectra of Mn_3O_4, $ZnMn_2O_4$ and $MgMn_2O_4$, taken from [44].

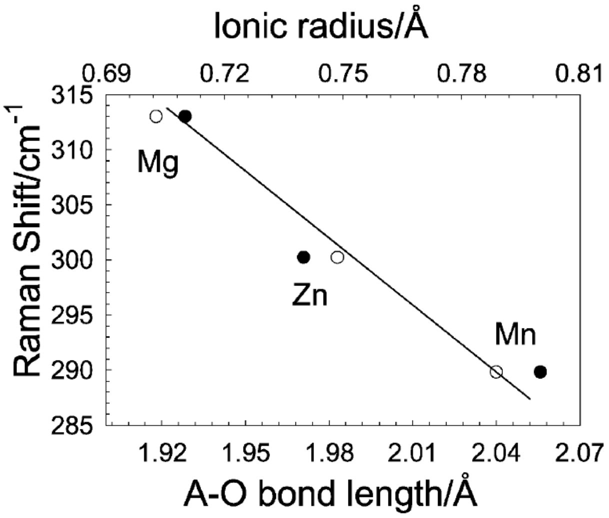

Figure 4.2: Dependence of the Raman shift of mode at ~300 cm^{-1} on the ionic radii (solid circles) and A–O bond lengths (open circles) for AMn_2O_4 (A= Mn, Mg and Zn) spinels, taken from [44].

taken from the article by Nádherný et al. [76], shows the spectra of zinc manganites with the formula $Zn_xMn_{3-x}O_4$ where the x varies from 0.15 to 1.29. The paper by Malavasi et al. [44], also quoted in this text, follows a different approach by comparing materials with the formula AMn_2O_4 with A = Zn, Mn, or Mg (Figure 4.1b). The nine peaks in the figure are analyzed below and the reasoning followed by Nádherný et al. [76] is reported for a possible assignment of the peaks. The position of the peak at 322 cm^{-1} does not change for each value of x examined. Its relative intensity, on the other hand, decreases with the decrease of zinc in stoichiometry. For $x \leq 0.75$ the most intense peak is the high-frequency peak at 678 cm^{-1}, while for x between 1 and 1.29 the most intense peak is the low-frequency peak at 322 cm^{-1}. This may suggest that the intensity ratio between the two peaks it is related to the substitution of Mn/Zn in the octahedra of the material. The small peak at 300 cm^{-1} is almost always visible and distinguishable from the main peak at 322 cm^{-1}. It is reported by Nádherný et al. [76] that the peak moves slightly at lower frequencies as the Zn content decreases. According to Malavasi et al. [44], there is a correlation between the energy of this peak and the length of the A-O bond. These two theses are not in contrast because by lowering the content of Zn some Mn could enter as substitution in Zn positions, hence forming Mn-O bonds substituting the previous Zn-O ones. As reported in Figure 4.2, Mn-O bonds are associated with a longer bond length and therefore lower frequencies. The peak at about 383 cm^{-1}, lowering the Zn content, moves towards lower frequencies (377 cm^{-1}) and broadens.[76] As the peak at ~383 cm^{-1} expands, the peak at 366 cm^{-1} is less identifiable and it is finally no more visible for x

= 0.45. This mode between 377-383 cm^{-1} seems to be related to the cationic exchange between Mn/Zn in the octahedra, too.[76] Finally, the third main peak at 678 cm^{-1} moves towards lower frequencies as the Zn content decreases. When zinc is not present (x = 0) and Mn_3O_4 is obtained (visible in Figure 4.1b), it reaches the minimum frequency of 654 cm^{-1}. This peak at 678 cm^{-1} is assigned by Nádherný et al. [76] to the motion of the oxygen atoms in the $[ZnO_4]$ tetrahedra and possesses A_{1g} symmetry. In contrast to this hypothesis, Malavasi et al. [44] assign this peak to the motion of the oxygen atoms in the $[MnO_6]$ octahedra (always with A_{1g} symmetry). The smaller peak at 630 cm^{-1} is clearly identifiable for x> 1, and it melts into a shoulder as the zinc concentration subsides.[76]

4.2. Annealing effect on ZMO films

In this section, I discuss how the crystalline structure was obtained and what tests and verifications were made. The films were annealed mostly at high temperatures in air using a Lenton muffle furnace. Some annealing tests were also conducted in vacuum using a home-made high-vacuum furnace.

First of all, it was necessary to understand at which temperature the films started to crystallize and to check the temperature compatibility with the substrates. In particular, for optical and electrochemical measurements glass and FTO-coated glass slides were used, and the threshold temperature that these substrates could reach before starting to lose their mechanical properties was around 550°C. The minimum temperature identified for crystallization is 500°C for 2 hours in air and 1 hour in vacuum. In air at 400°C the films remain amorphous and at 450°C crystallize only partially. For some selected samples (deposited at 1 Pa and 50 Pa of oxygen on silicon substrate), annealing tests were performed at 500°C, 600°C, 700°C, 800°C for 2 hours in air, and at 500°C for 1 hour in vacuum. In this section, we will compare the films subjected to these different annealing condition, while the comparison between the annealed films and the as-deposited ones refers to the next section.

After having thermally treated the samples, they were examined with Raman spectroscopy (excitation laser $\lambda = 532$ nm). The spectra obtained are compatible with those reported in the literature discussed in the section, thus demonstrating crystallization (Figure 4.3). Fittings with Lorentzian curves were performed on these spectra to assess whether there were any recognizable trends as the annealing temperature varied. In this section, the main peaks at 322 cm^{-1}, 377 cm^{-1}, and 678 cm^{-1} are referred to as P1, P2, and P3, respectively. First, the position of the peaks has no significant variations or a recognizable trend as a function of the annealing temperature. Since peak positions do not shift significantly as a function of annealing temperature in air, an average of peak

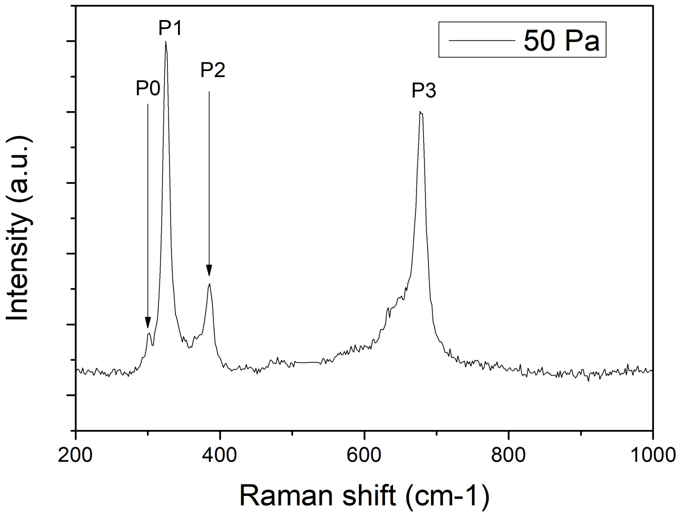

Figure 4.3: Raman spectrum of ZMO film deposited on FTO-coated glass at 50 Pa of oxygen and annealed in air at 500°C for 2 hours.

positions on samples deposited at the same pressure but different annealing temperatures is presented here. The average peak positions for the samples deposited at 1 Pa of oxygen and annealed in air are P1 at 324 cm^{-1}, P2 at 381 cm^{-1}, and P3 at 674 cm^{-1}. On the other hand, the vacuum annealed sample deposited at 1 Pa of oxygen has the following positions: P1 at 323 cm^{-1}, P2 at 379 cm^{-1}, and P3 at 670 cm^{-1}. The samples deposited at 50 Pa of oxygen have the following average positions for annealing in air: P1 at 325 cm^{-1}, P2 at 383 cm^{-1}, and P3 at 678 cm^{-1}. While the one at 50 Pa of oxygen annealed in vacuum shows: P1 at 326 cm^{-1}, P2 at 378 cm^{-1}, and P3 at 675 cm^{-1}. As for the intensity ratios between the main peaks, again (referring to the data presented for samples deposited at 1 Pa and 50 Pa of oxygen) there seems to be no correlation with the annealing treatment received. As reference in Figure 4.4 the spectra acquired for the samples deposited at 1 Pa of oxygen after the diverse air annealings are presented.

On the other hand, the full width at half maximum (FWHM) has a recognizable trend with respect to the annealing temperature. As can be seen in Figure 4.5, the plot shows a decreasing trend of the FWHM of the peaks as a function of the annealing temperature. The FWHMs data for the vacuum-annealed samples are not shown in the plots, but they are larger than all the annealed samples at a temperature $\geq$500°C in air. The sole exception is the P3's FWHM of the sample deposited in 1 Pa of oxygen and vacuum-annealed at 500°C, which is lower than the FWHM of the corresponding annealing at 500°C in air. The explanation for this behavior is that a higher heat treatment temperature leads to better crystalline quality and to larger crystal grains in the material.

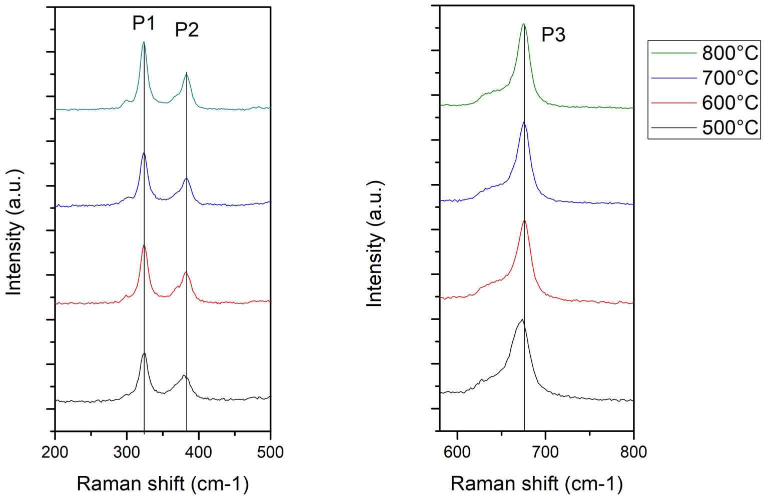

(a) (b)

Figure 4.4: Raman spectra (laser wavelength 532 nm, power 0.7 mW) of samples deposited at 1 Pa of oxygen on silicon and annealed at different temperature for 2 h in air. In (a) P1, P2 are visible; in (b) P3 is presented. All the spectra are normalized after removing the signal of the silicon substrate.

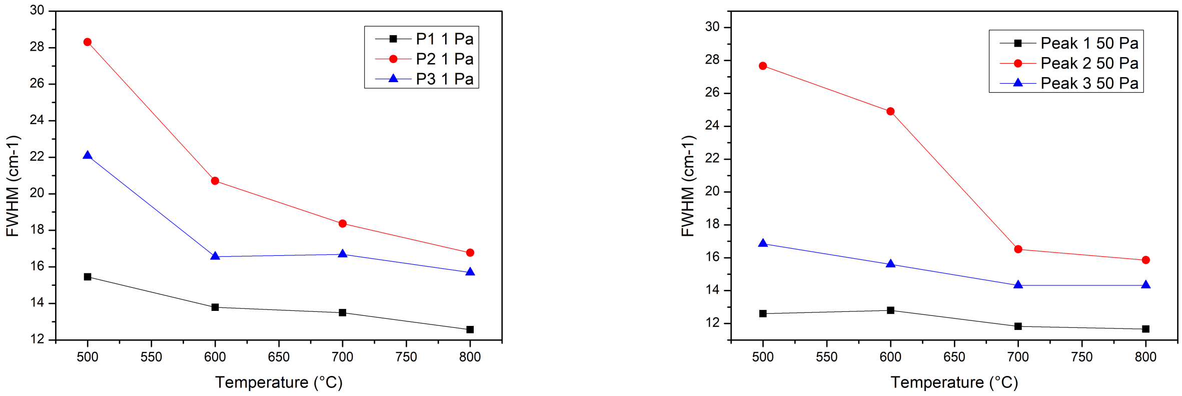

(a) (b)

Figure 4.5: Peaks' FWHM vs. annealing temperature in air for 2 h. (a) Sample deposited in 1 Pa of oxygen. (b) Sample deposited in 50 Pa of oxygen.

The SEM images of the sample top surfaces also clearly show an increase in the grain size of the material as the annealing temperature increases (Figures 4.6 and 4.7). It is positive to note that even between the samples annealed equally at 500°C, larger grains are observed in the ZMO films annealed in air compared to the films annealed in vacuum;

and as mentioned above, this aspect is also well expressed by the Raman FWHM data. The last aspect analyzed concerns stoichiometry, and also in this case it seems that the application of different annealing temperatures in air does not cause a particular variation in the atomic elemental content. The sample annealed in vacuum, on the other hand, differs from those annealed in air, since the oxygen content is reduced by a few percentage points and the zinc content is increased. A more in-depth analysis on the variation of oxygen content between as-deposited an annealed samples is presented in the next section.

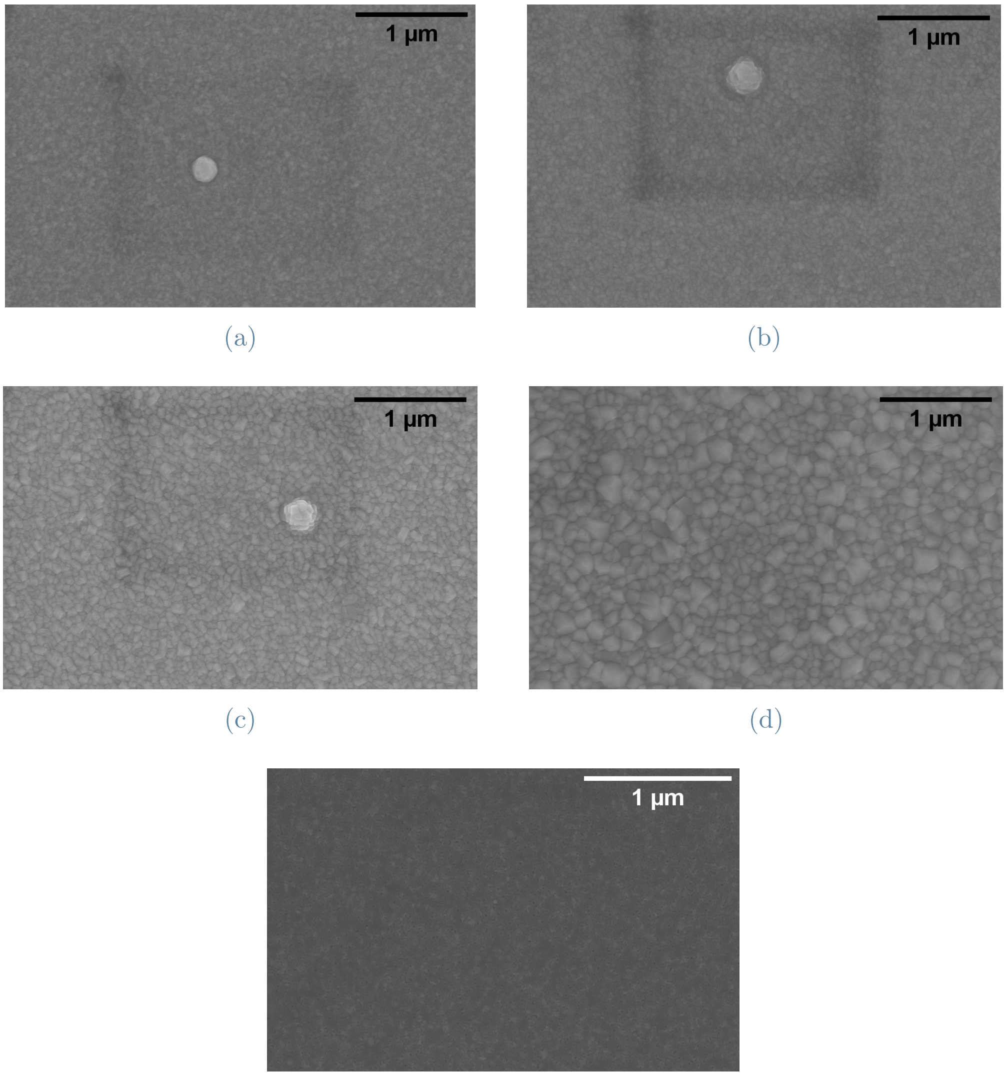

(a) (b)

(c) (d)

(e)

Figure 4.6: Top-view SEM images of samples deposited in 1 Pa of oxygen and annealed at 500 (a), 600 (b), 700 (c), 800°C (d) in air for 2 h and at 500°C in vacuum for 1 h (e).

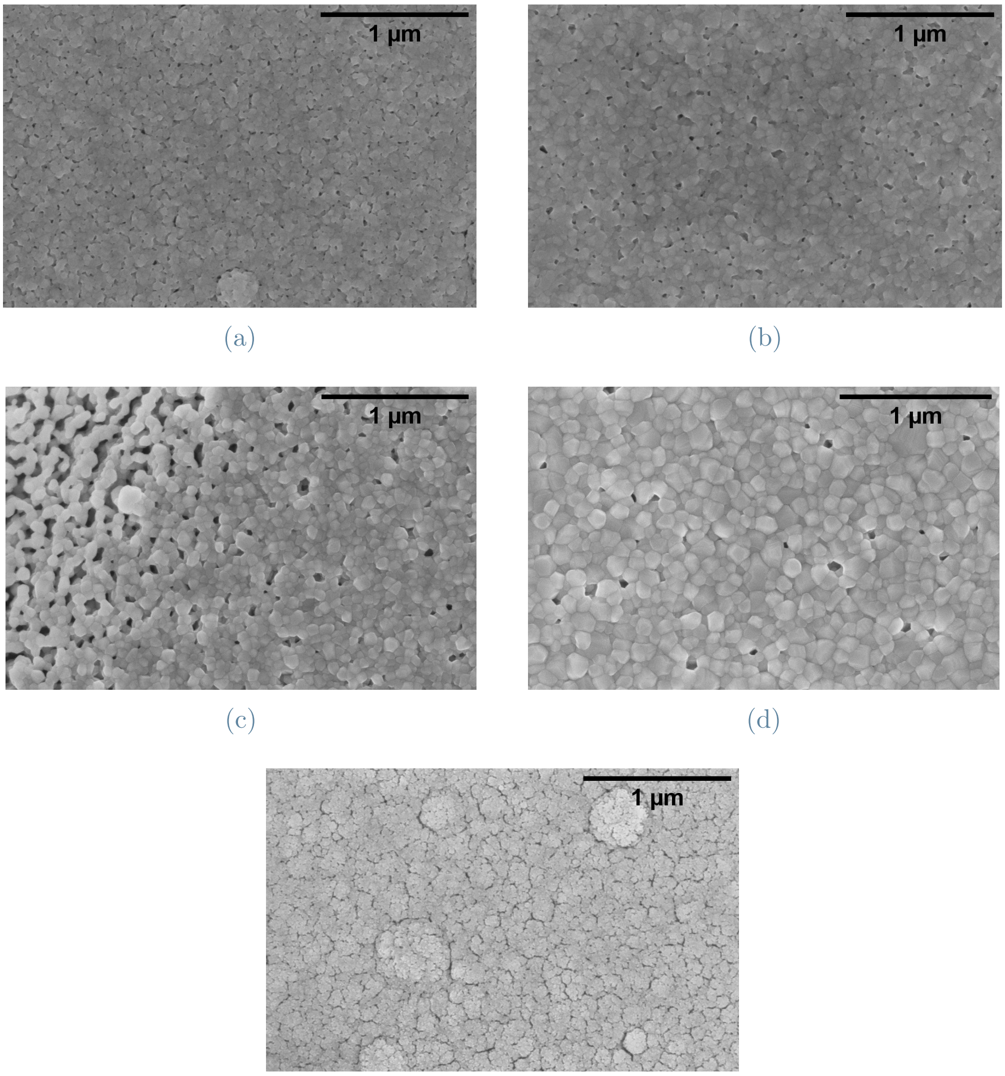

(a) (b)

(c) (d)

(e)

Figure 4.7: Top-view SEM images of samples deposited in 50 Pa of oxygen and annealed at 500 (a), 600 (b), 700 (c), 800°C (d) in air for 2 h and 500°C in vacuum for 1 h (e).

4.3. Deposition pressure effect on the annealed films

In this section, annealed samples are compared to as-deposited ones in term of morphology and stoichiometry; in addition, the effect of deposition conditions on the Raman spectra of crystalline ZMO samples is presented.

4.3.1. Oxygen content

Figure 4.8 shows the oxygen atomic contents, measured by EDXS, of the samples deposited at various pressures of oxygen before and after annealing. All the examined samples underwent annealing in air at 600°C for 3 h, except for the samples denoted as 1v and 50v, which were deposited at 1 Pa and 50 Pa of oxygen, but annealed in vacuum at 500°C for 1 h. The plot (Figure 4.8) clearly shows that regardless of the oxygen content of the pristine sample, the oxygen content settles between 51% and 55% after the annealing. These values are always sub-stoichiometric compared with the oxygen content of stoichiometric $ZnMn_2O_4$ (57.14 %). Also, it is notable that among the films deposited from 10 to 100 Pa of oxygen, the annealed samples exhibit a decreasing trend in the oxygen content with the increasing pressure, with the lowest O contentment in the annealed sample deposited at 100 Pa. Therefore, it could be hypothesized that, given the more porous morphology of the samples produced at higher pressures, they are more likely to lose excess oxygen during annealing. Finally, it is foreseeable that vacuum annealed samples cannot incorporate oxygen during annealing. This seems to be confirmed by the different behaviors of the two samples deposited at 1 Pa. The one annealed in air incorporates oxygen and increases its oxygen content, while the one annealed in vacuum (1v) loses oxygen compared to its initial composition.

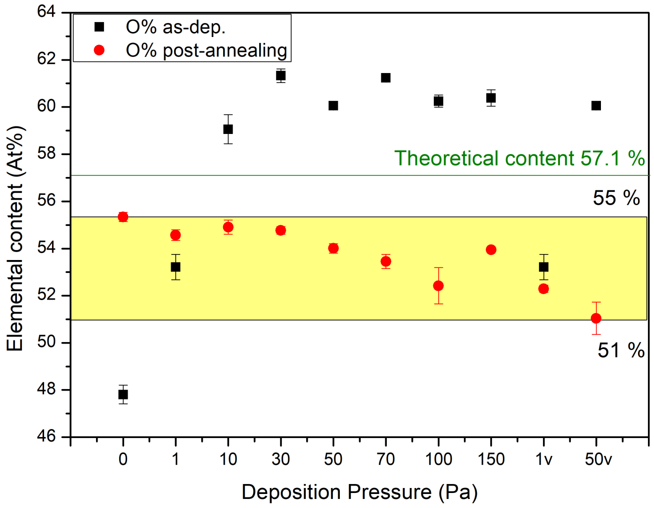

Figure 4.8: Samples' oxygen content before and after annealing in air or vacuum. The green line indicates the oxygen percent in the stoichiometric $ZnMn_2O_4$ as a reference. The error bars are the standard deviations of five measurements taken at different points for each sample.

4.3.2. Morphology comparison

The morphology of the films undergoes changes during the annealing process. For comparison, the morphologies of all the samples produced before and after the annealing were analyzed by SEM. Here (Figure 4.9), the cases of two films are presented, one compact (produced at 1 Pa of oxygen) and one porous (produced at 100 Pa of oxygen); as-deposited films are shown on the left, while annealed films (600°C in air for 3 hours) are on the right. The first noticeable point is the formation of crystalline grains in the films, which further confirms the crystallization of the material. In Figures 4.9b and 4.9d, crystal grains can be observed in both top-view and cross-sectional SEM images of the film deposited at 1 Pa of oxygen. In the film produced at 100 Pa, the cross-sectional SEM images (Figures 4.9h and 4.10) reveal numerous crystals that give rise to a "knotted mesh", where the original tree-like structures are replaced by small crystallites (50-70 nm) arranged into columns. Often, the pre- and post-annealing films varied in thickness as can be seen by comparing the cross-sections of 1 Pa (Figures 4.9c and 4.9d). In general, the morphology of annealed films has a higher porosity and more voids, visible from the comparison of the cross-sectional images. Finally, the film deposited at 100 Pa, which already had an island-like topography when amorphous (Figure 4.9e), tends to accentuate this feature by leaving even more space between one island and another. (Figure 4.9f). These considerations, concerning these two examples, are general for all films deposited at various oxygen pressures and subjected to annealing in air.

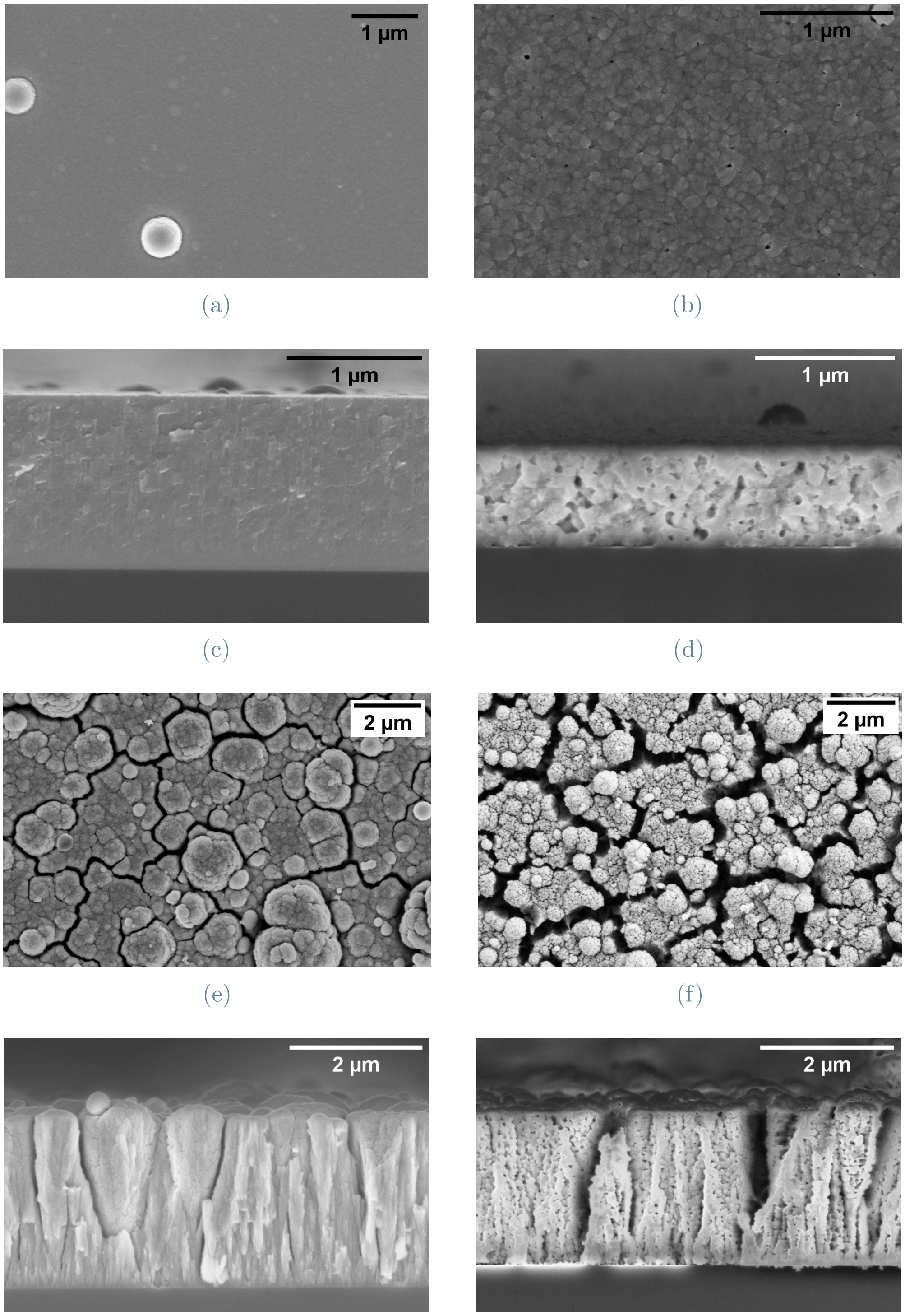

(a) (b) (c) (d) (e) (f) (g) (h)

Figure 4.9: Top-view and cross-sectional SEM images of as-deposited (on the left) and annealed (on the right) ZMO films. (a)-(d) deposited at 1 Pa of oxygen, (e)-(h) deposited at 100 Pa of oxygen.

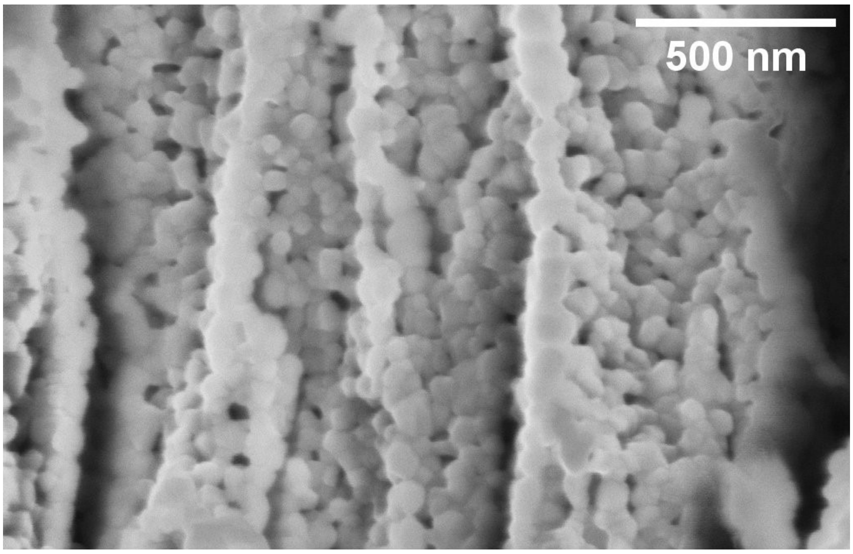

Figure 4.10: SEM cross-sectional image at higher magnification of the film deposited in 100 Pa of oxygen and annealed in air at 600°C for 3 h.

4.3.3. Deposition pressure effect on Raman spectra

A more quantitative analysis of the Raman spectra of annealed samples as a function of the deposition oxygen pressures is presented in this section. All the films were deposited with the same laser fluence of 3.8 J/cm2 and annealed in air at 600°C for 3 h. Raman spectra were analyzed by the multi-peak fitting of the data using Lorentzian curves. The plots representing the Raman shifts of the peaks, the widths of the peaks, and the relative intensities (in the form of peak height ratio) are reported in Figures 4.12, 4.13, and 4.14. The peaks are again indicated with the convention presented above, where P1 is the one at ∼322 cm^{-1}, P2 at ∼377 cm^{-1}, and P3 at ∼678 cm^{-1}. Analyses were also performed on the peak at ∼300 cm^{-1} which was herein referred to as P0 (Figure 4.11). In all the plots, the trend can be divided into two stages. The first stage concerns the samples deposited in vacuum and at 1 Pa of oxygen, while the second one concerns all the other samples at pressures equal to or higher than 10 Pa. The two samples deposited in vacuum and 1 Pa exhibit measured values far from the others in almost all the plots. The samples deposited at 10 Pa or higher seem to feature a slightly increasing plateau in the Raman shift (Figure 4.12) and intensity ratio (Figure 4.14) charts, and a decreasing one in the FWHM charts (Figure 4.13) as the oxygen pressure increases. The first interpretation of these results can be attributed to the effect of crystallinity. Since different deposition pressure gives rise to different crystal sizes and orientations after annealing, the corresponding Raman spectra may reflect this behaviour. However, looking at the obtained trends and comparing them with Nádherný et al. [76]'s work, some similarities can be seen. Firstly, in [76] the relative

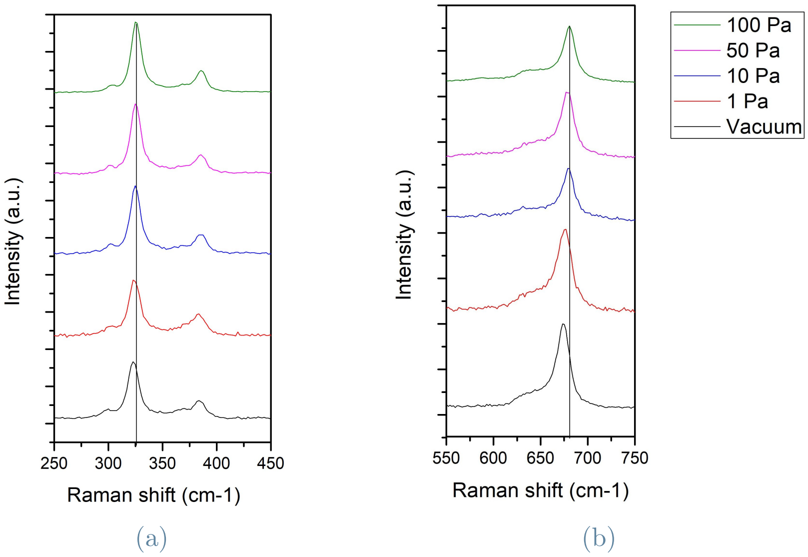

(a) (b)

Figure 4.11: Raman spectra (laser wavelength 532 nm, power 0.7 mW) of samples deposited at different pressures of oxygen on silicon and annealed at 600°C for 3 h in air. In (a) P0, P1, P2 are visible; in (b) P3 is presented. All the spectra are normalized after removing the signal of the silicon substrate.

intensity of P1 with respect to P3 increases with Zn content, and the relative intensity of P1 also increases, non-monotonically, with deposition pressure in my work. Secondly, P0, P2 and P3 move toward higher frequencies with increasing Zn content according to Nádherný et al. [76], and they also shift toward higher frequencies with deposition pressure. Finally, P2 narrows as the Zn percentage increases, and the FWHM of P2 decreases as the pressure increases, so the peak also narrows. These correlations suggest that the effect on the Raman spectrum of the crystalline material of an increase in oxygen deposition pressure and an increase in the Zn content is similar. As a result, one may speculate that, even after annealing in equal conditions, deposition pressure still affects the sample by acting on the relative Zn/Mn content. To further test this hypothesis, zinc content was analyzed by EDXS as a function of deposition pressure. Although it should be stressed that the changes in Zn made by Nádherný et al. [76] are greater than those of our samples noted with EDXS, the trends seem to match. Of course, further studies with other characterization techniques such as X-ray photoelectron spectroscopy (XPS), X-Ray Diffraction (XRD), and X-ray Absorption Spectroscopy (XAS) are needed to validate our interpretation.

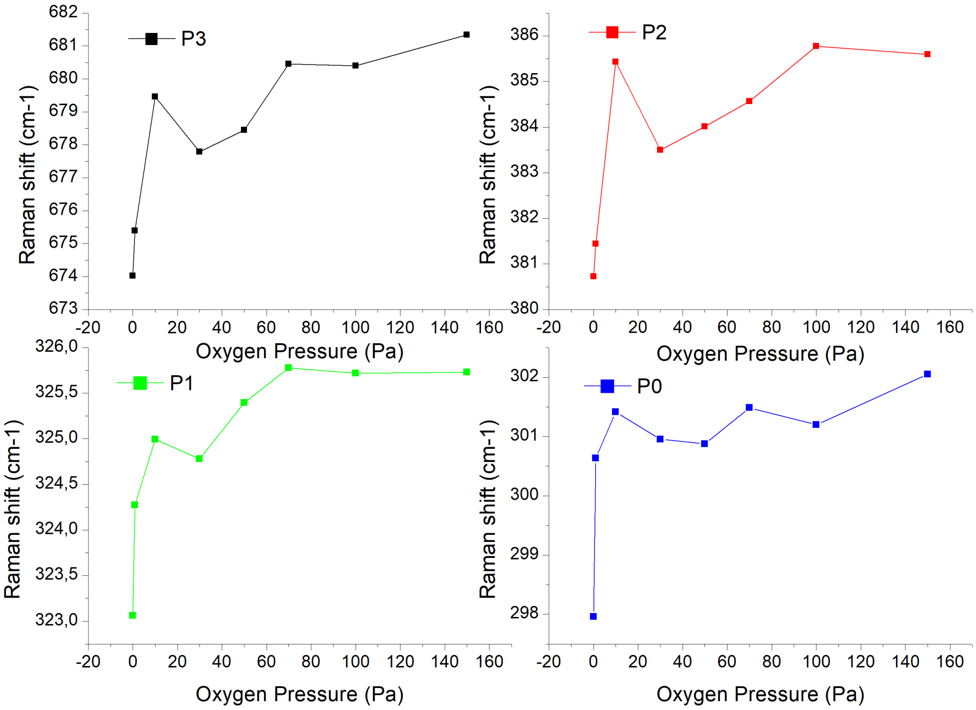

Figure 4.12: Plot of Raman peak shift vs. deposition pressures.

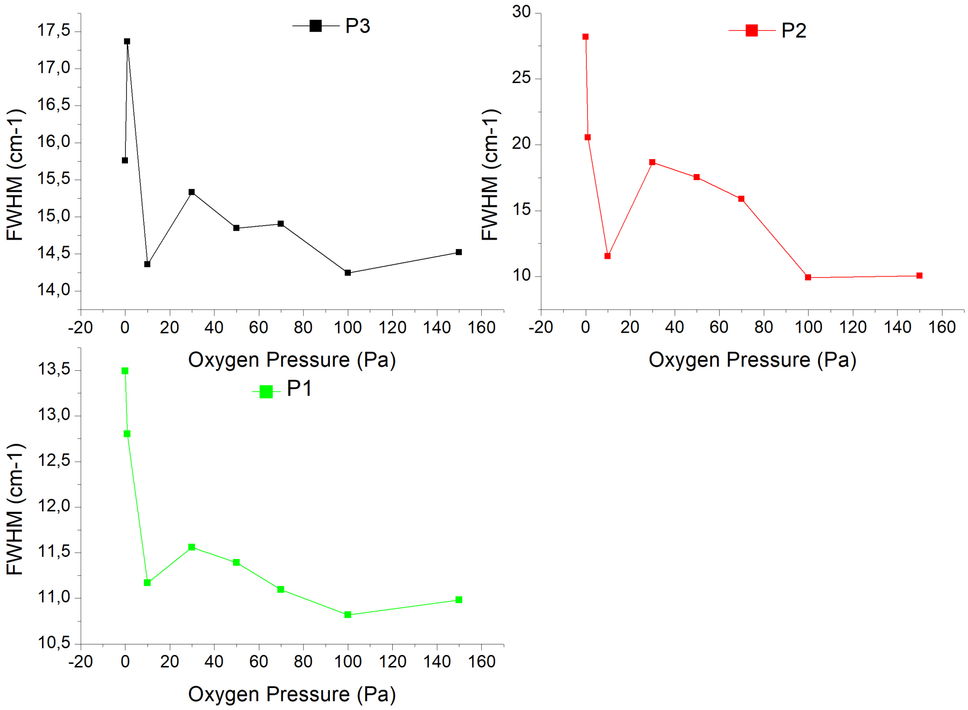

Figure 4.13: Plot of peaks' FWHM vs. deposition pressures.

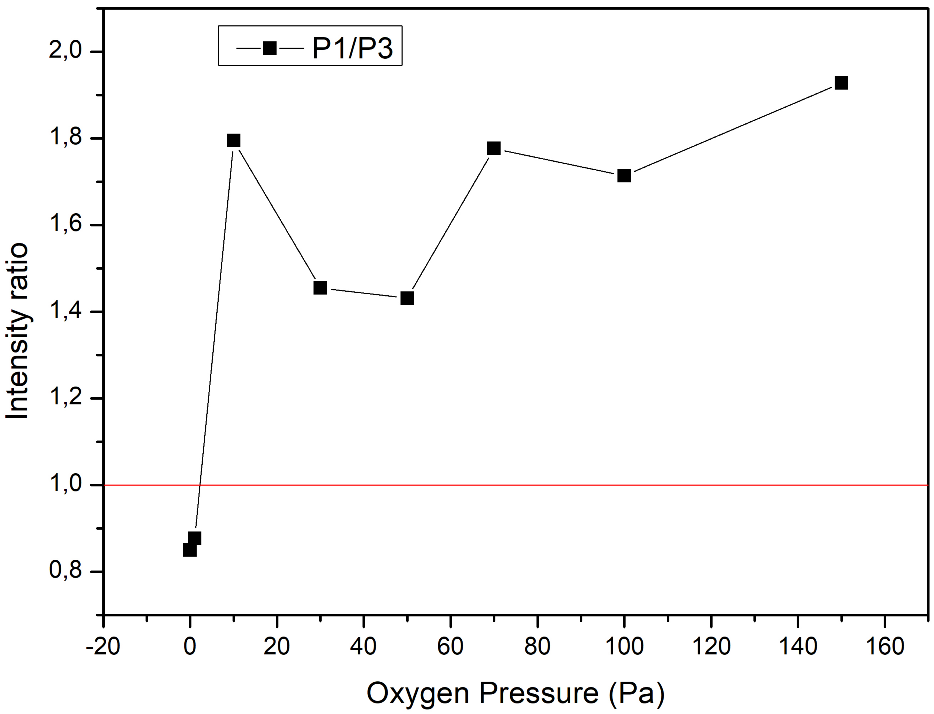

Figure 4.14: Plot of height intensity ratio between P1 and P3 vs. deposition pressures.

4.4. Optical measurements

The optical measurements conducted on samples deposited at different oxygen pressures and over a glass substrate are presented in this section. Deposition time at any oxygen pressure was set in order to obtain a film thickness of ∼500-550 nm. There is no a theoretical study about the optical properties of ZMO to refer to, and a few experimental works exist.[77–79] Usually, ZMO is regarded to as a direct band-gap crystal (∼2.19 eV)[77]. In my work, the transmittance, reflectance, and absorbance curves of crystalline ZMO samples deposited in vacuum and at 1 Pa, 10 Pa, 50 Pa, and 100 Pa of oxygen and annealed in air at 500°C for 2h were measured. Crystallization to the expected ZMO was verified by Raman spectroscopy. Optical curves are presented in Figure 4.15 after normalization with respect to the glass substrate and to instrumental corrections.

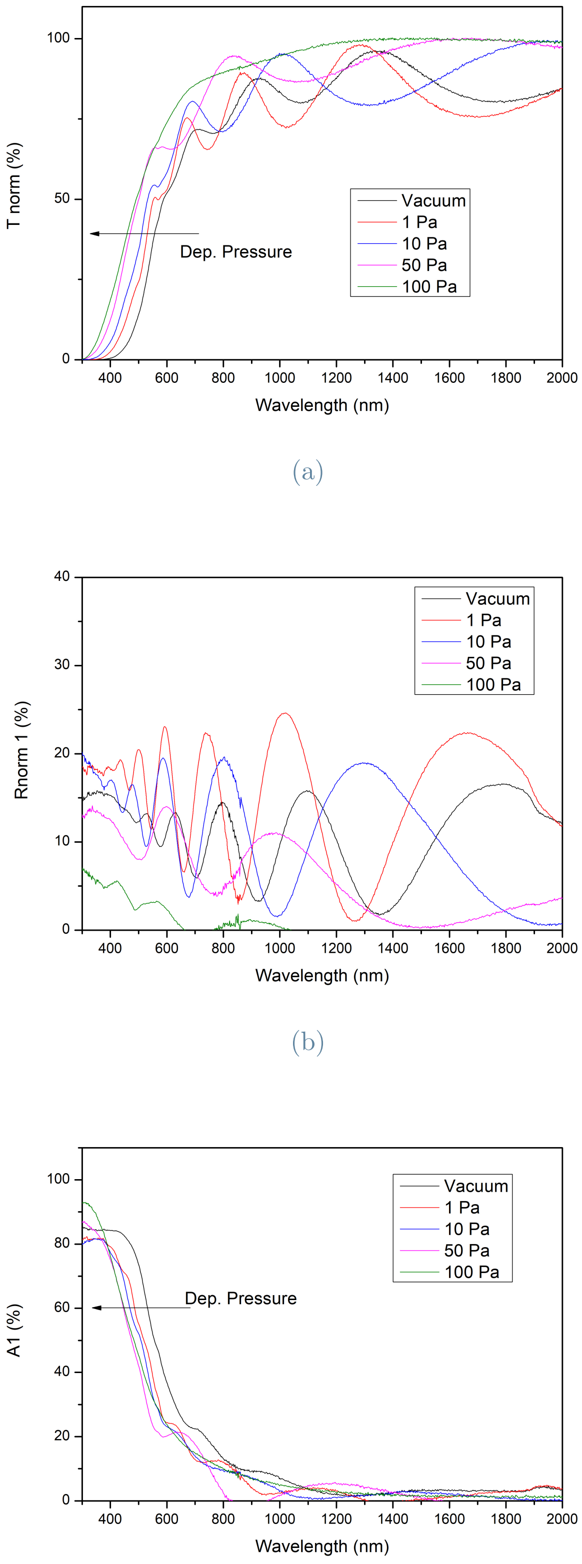

(a)

(b)

(c)

Figure 4.15: Transmittance (a), reflectance (b), and absorbance (c) curves of the crystalline ZMO films deposited at different oxygen pressures.

The arrow in Figures 4.15a and 4.15c highlights the increasing deposition pressure. Looking at Figure 4.15a and fixing a wavelength, such as 400 nm, transmittance increases with increasing deposition oxygen pressure. On the other hand, in Figure 4.15c, fixing the wavelength at 400 nm, the absorbance decreases with increasing deposition oxygen pressure, as expected. Moving to the left on the wavelength axis (Figure 4.15c) the film begins to significantly absorb around the low wavelengths at 700-800 nm. The reflectance (Figure 4.15b) does not have a definite trend, however, always remains below 25 percent. It is important to point out that the curves reported for the vacuum-deposited sample should be taken with caution, as the Raman analysis of vacuum-deposited air-annealed samples on glass reveals a spectrum that differs from that of ZMO (this behaviour does not occur on silicon substrate for vacuum deposition or in any other film deposited on glass).

5 | ZMO electrochemistry

This chapter presents the preliminary electrochemical measurements and post-electrochemistry Raman analysis performed on the samples.

5.1. Electrochemistry setup

The first issue to be addressed was the optimization of the setup. The intention was to obtain an experimental setup that would allow electrochemical measurements simultaneously with in-situ Raman spectroscopy. Measurements, in this thesis, were made quasi-in situ by acquiring the Raman spectra of the sample immediately after electrochemistry; however, for future work, the setup has been refined and in-situ measurements will be possible. The Teflon cell (Figure 5.1), made available by SoLINano-Σ and used in the measurements, allows the working electrode (the ZMO film) to be inserted at the base. An O-ring is inserted on top of the film, covered, and pressed by the cell. Inside the central well, the liquid electrolyte can be inserted (∼1 mL). The cell is equipped with channels, which were used to insert the two platinum wires acting as the counter electrode and the quasi-reference electrode. The electrolytes adopted for the measurements are composed of deionized water with zinc sulfate and/or manganese sulfate dissolved. The chemical products employed for the electrolytes were: Zinc sulphate heptahydrate (Sigma Aldrich, 99.0%) and Manganese(II) sulphate monohydrate (Sigma Aldrich, 98%). The three electrolytes used were: $ZnSO_4$ 2 M (ZS electrolyte), $MnSO_4$ 0.1 M (MS electrolyte) and $ZnSO_4$ 2 M + $MnSO_4$ 0.1 M (ZMS electrolyte). The ZMS electrolyte was used in almost all measurements, where, in addition to the Zn^{2+} ion being present for intercalation, Mn^{2+} ions are also present to alleviate the dissolution problems mentioned in Section 1.4. It was verified that in the potential ranges (listed below for CVs) and in the electrolytes used for the measurements, the platinum quasi-reference remains at nearly constant potential. Specifically, its potential value was measured in a two-electrode configuration to be + 445 mV relative to the Ag/AgCl reference electrode, with a stability within a few mV. Finally, the films used for the electrochemical measurements were all produced by PLD at different oxygen pressures on FTO-coated glass substrates and then subjected to

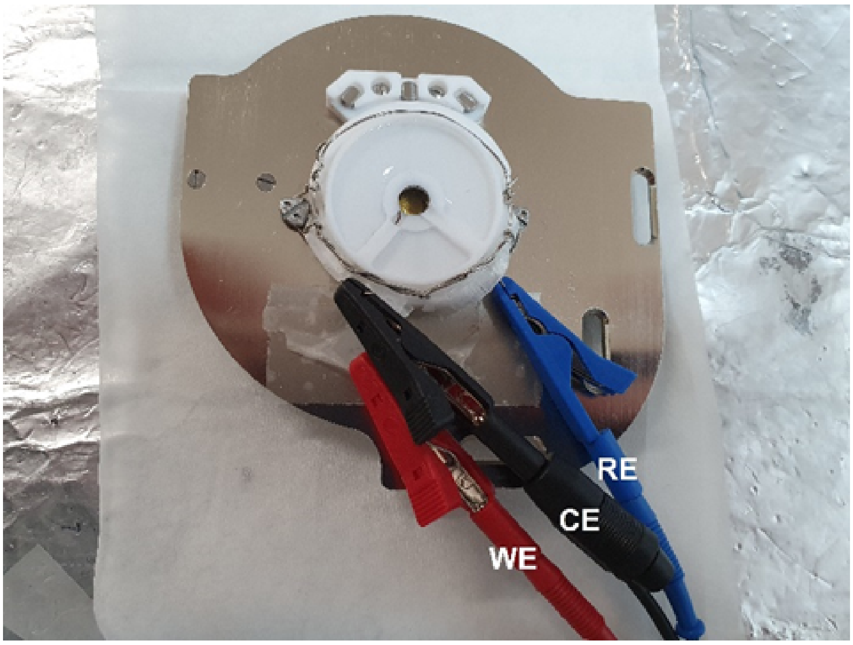

Figure 5.1: Teflon cell used in this work for electrochemical measurements.

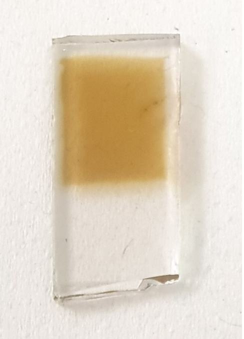

Figure 5.2: ZMO deposited in 50 Pa of oxygen and annealed at 500°C for 2 h on FTO-coated glass.

annealing in air at 500°C for 2 h. Deposition time at any oxygen pressure was set in order to obtain a film thickness of ∼500-600 nm. The films exhibit poor electronic conductivity and require a conductive substrate to be used in electrochemical measurements. The ZMO films were deposited on pre-defined regions of the substrate, by properly masking it during the deposition, so one extremity of the conductive sample could be connected away from the electrolyte via copper tape and copper wire to the potentiostat (Figure 5.2). Commonly used metals, such as copper, are not stable in the potential ranges selected and used in my measurements. On the other hand, conductive carbon substrates, like glassy carbon, are prone to oxidation during the air annealing of the films. Therefore, the choice fell on fluorine-doped tin oxide (FTO) coated on soda-lime glass slides [produced by Sigma-Aldrich, total thickness (2.2 mm), FTO thickness (550 nm), sheet resistance (∼7

Ω/sq), composition ($SnO_2 : F$ ~1.85)]. Noble metals, such as gold or platinum, were also good candidates. Initial evaporation tests of gold on silicon substrates were performed, however, the gold-silicon adhesion was not sufficient to sustain the ZMO PLD deposition. Instead, a platinum film was deposited on silicon by PLD. This route proved to be more promising by withstanding annealing tests and succeeding in obtaining ZMO on top of such substrates. Electrochemical tests on samples deposited on platinum, however, have yet to be carried out. In addition, platinum is expensive and the preparation of samples requires a two-step PLD route.

5.2. Cyclic voltammetry

Cyclic voltammetry (CVs) were performed on selected samples with the potential scanning in a range of -0.75 V to +0.75 V vs. Pt-QRef., starting at 0 V, proceeding in cathodic direction, and adopting a scan rate of 25 mV/s for eight cycles. These values were chosen based on previous tests and agreed with Professor B. Bozzini (Battery Materials Engineering Laboratory (BMEL), Energy Department, Politecnico di Milano), who led the work about the electrochemistry part. The electrolyte used for the CVs presented here is ZMS. The CVs were performed on the samples deposited at 1 Pa, 50 Pa, and 100 Pa oxygen and annealed in air at 500°C for 2 h, in order to test the electrochemical response of films with different porosity. The plot of the sample deposited at 1 Pa of oxygen (Figure 5.3) shows a broad peak in the anodic region (oxidation, upper part of the graph) at potential values that shift as cycles progress to more positive potentials, moving from +0.2 to +0.6 V. In addition, a shoulder to the main oxidation peak (between 0 and +0.2 V) gradually rises during cycles. In cathodic region (reduction, lower part of the plot), there are two peaks: one approximately stable around +0.25 V, and the other moving to more negative potentials between -0.2 and -0.4 V as cycles progress. Both the main anodic and cathodic peaks, in addition to moving towards larger potentials (in absolute values), increase in current intensity exchanged during cycling. This behaviour, which is observed in all the samples but is more relevant for the film deposited at 1 Pa, is related to an increase in the electrode polarization during cycling at high scan rate, which may be due to the formation of insulating/passivating phases at the interface. The CVs of the sample deposited at 50 Pa of oxygen (Figure 5.4) show two close peaks in the anodic region, between +0.3 and +0.6 V, which become more defined and shift as the cycles continue. A shoulder similar to that observed in the CVs for the 1 Pa sample is observed around +0.2 V. In the cathodic region, on the other hand, the reduction peaks are one between +0.4-+0.5 V and the other around 0 V. Finally, the CVs of the sample deposited at 100 Pa of oxygen (Figure 5.5) show two close peaks in the anodic

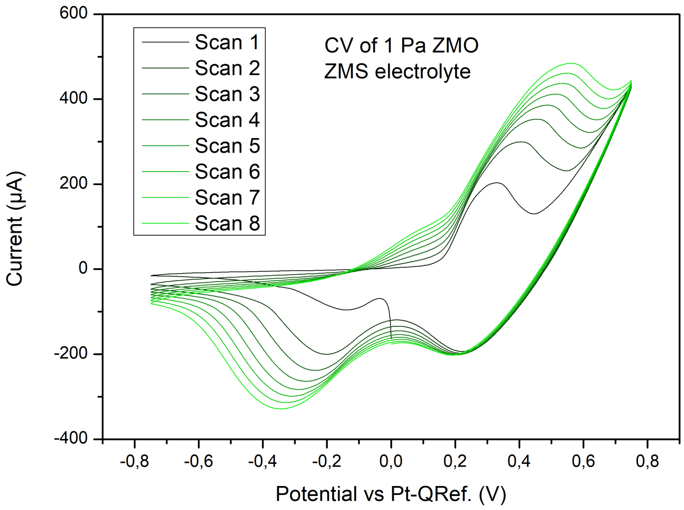

Figure 5.3: CVs performed in ZMS electrolyte on ZMO film deposited in 1 Pa of oxygen and annealed in air at 500°C for 2 h.

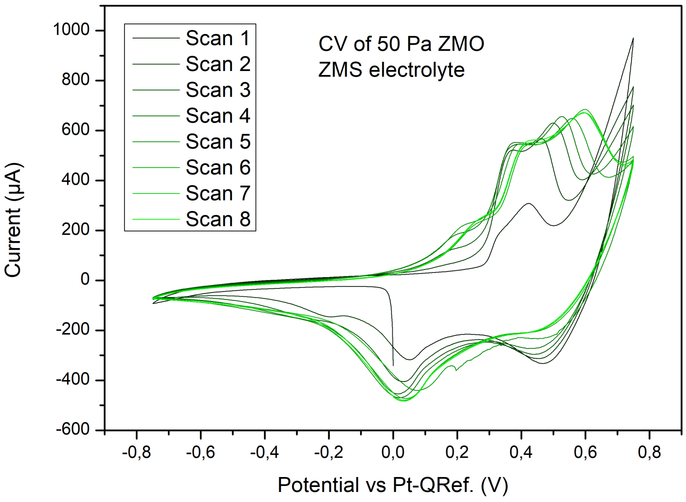

Figure 5.4: CVs performed in ZMS electrolyte on ZMO film deposited in 50 Pa of oxygen and annealed in air at 500°C for 2 h.

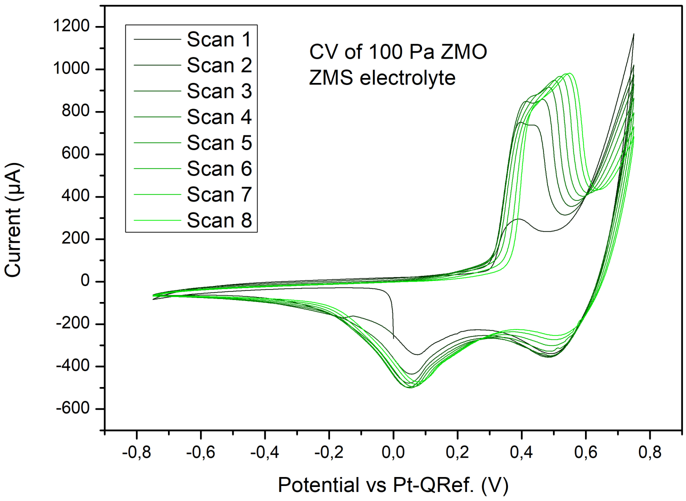

Figure 5.5: CVs performed in ZMS electrolyte on ZMO film deposited in 100 Pa of oxygen and annealed in air at 500°C for 2 h.

region between +0.3 and +0.6 V. The two peaks in the cathodic region are at +0.5 V and between 0 and +0.1 V. After the initial cycles, this cyclovoltammetry appears to be more stable than the previous ones, with the peaks shifting slightly. A comparison of the last cycle for each sample is presented in Figure 5.6. The progression between the three curves is observable with the film deposited at 1 Pa with only one peak in the anodic region, which rises and begins to split at 50 Pa, and, finally, becomes narrower and with two close peaks at 100 Pa. The increase of current before the anodic peak(s) is more gradual for the samples deposited at 1 and 50 Pa of oxygen because of the presence of a shoulder that rises during cycling; instead, a steeper increase is observed for the sample deposited at 100 Pa. Similarly, the cathodic peaks move toward more positive potentials gradually from 1 to 50 to 100 Pa. Morphology (due to different deposition pressures) thus affects charge exchange during electrochemistry, directly influencing the area enclosed in CV curves, peaks height (i.e., current), and reaction kinetics (consequently peaks shape). In conclusion, the CVs obtained from my experiments are consistent with those reported in the literature for ZMO samples[46, 51] (Figure 5.7), especially for the more porous sample deposited at 100 Pa. They thus demonstrate, despite the study being at an early stage, the compatibility of our films, deposited by PLD, with the electrochemical data reported in literature for other ZMO nanostructures. Raman spectra of the samples were acquired with the SoLINano-Σ's Raman spectrometer (excitation laser = 532 nm) before undergoing electrochemical measurements and after CVs (Figure 5.8). The frequencies of the peak centers do not vary significantly, while for all the three samples a new band

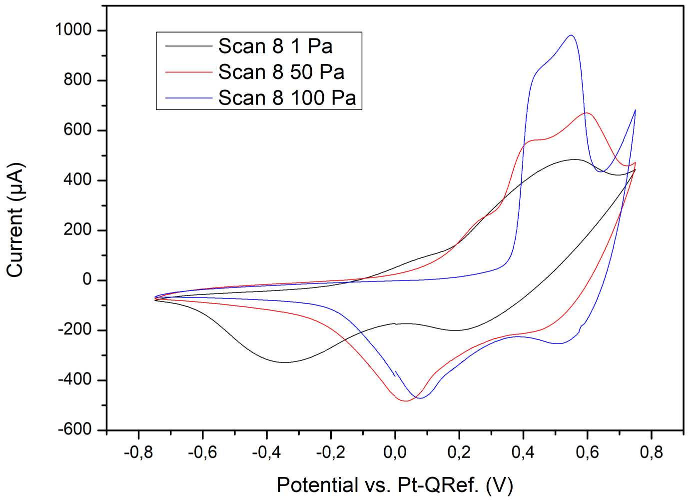

Figure 5.6: Comparison of the eighth CV cycle performed in ZMS electrolyte on ZMO films deposited in 1 Pa, 50 Pa and 100 Pa of oxygen and annealed in air at 500°C for 2 h.

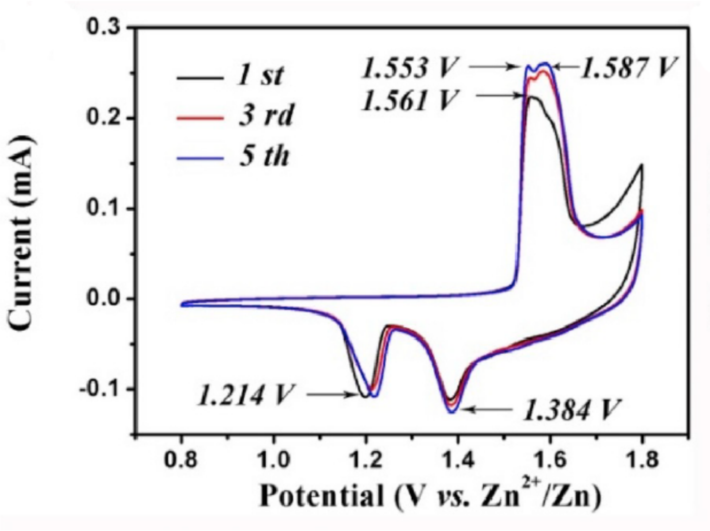

Figure 5.7: CVs curve at a scan rate of 0.1 mV/s of ZMO@PCPs as cathode in aqueous ZIBs in mixed aqueous solution consisting of 1.0 M $ZnSO_4$ and 0.05 M $MnSO_4$ as electrolyte. Taken from [46].

is obtained around 480-500 cm^{-1} and the shoulder of peak P3 ($\sim$ 676 cm^{-1}) increases. Finally, the height intensity ratio between P1 and P3 varies as P3 increases after CVs for samples deposited at 1 Pa and 50 Pa of oxygen.

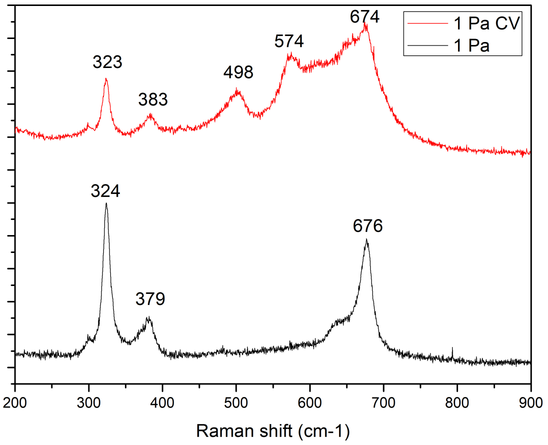

(a)

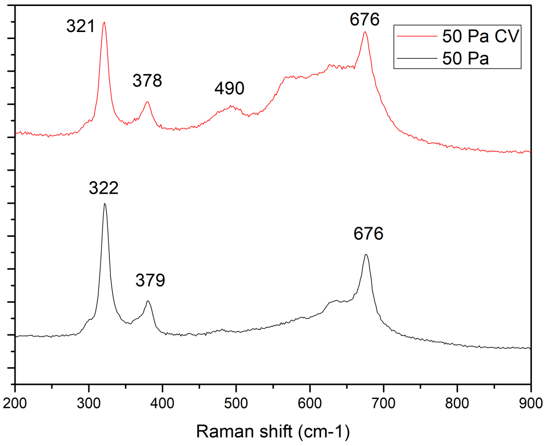

(b)

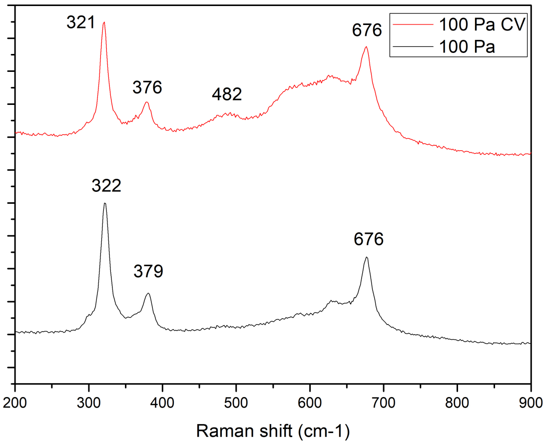

(c)

Figure 5.8: Raman spectra acquired before (black) and after (red) CV (in ZMS) of the samples deposited at 1 Pa, 50 Pa, and 100 Pa of oxygen and annealed in air at 500°C for 2 h, respectively. Excitation laser wavelength: 532 nm.

5.3. Potentiostatic measurements

In order to study the evolution of the Raman spectra of the sample deposited at 100 Pa oxygen during electrochemistry, a constant potential was applied to the film, trying to force one reaction of those hypothesized in Section 1.5.3, such as intercalation and de-intercalation of zinc. The values of the applied potentials were selected according to the CV shown above: +0.6 V was applied to keep the film into the anodic region (oxidation), while a potential of 0 V was applied for the cathodic region (reduction). The time of the potentiostatic (PS) measurement was adjusted such that the measured current reached a zero value, i.e., at the end of the reaction, or until a stable condition was reached.

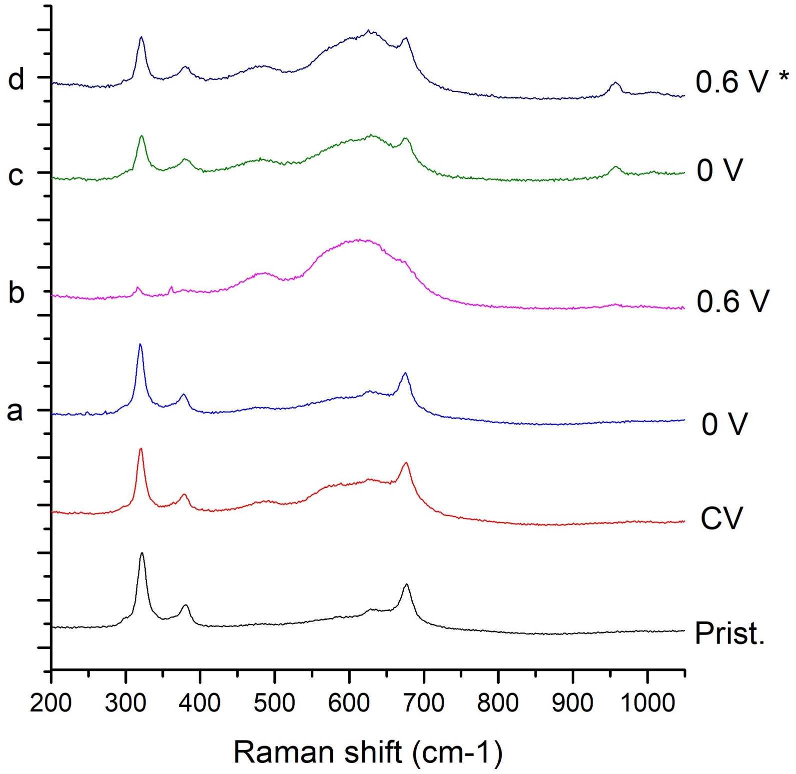

Figure 5.9: Raman spectra of ZMO film deposited in 100 Pa of oxygen and annealed in air at 500°C for 2 h. Spectra were acquired for pristine ZMO, after the CVs, and after four PS tests (a-c in ZMS electrolyte, while d in ZS electrolyte, as indicated by *), applied subsequently on the same sample. Excitation Laser: 532 nm.

Figure 5.9 shows the Raman spectra of the ZMO sample in different potential conditions. The sample after the first PS (in ZMS electrolyte) at 0 V (cathodic polarization) seems to be more similar to the pristine one, as the P3 peak shoulder lowers (in Figure 5.9 the spectrum a). The curve representing the current over time shows a negative current tending to 0, confirming that the film is in the cathodic region. After the anodic polarization (+0.6 V, spectrum b in the Figure 5.9), on the other hand, the two low-frequency peaks P1 and P2 seem to almost disappear, and peak P3 is incorporated into the shoulder, which becomes a large band around 600 cm^{-1}. Referring to the article by Yang et al. [46] (which attributes peaks P1 and P2 to Zn-O vibrations), this behavior could be attributed to the egress of zinc from the material, which results in the fading of the modes associated with it and in the formation of amorphous manganese dioxide. In fact, in the anodic region the reaction would be:

$$ZnMn_2O_4 \rightarrow Zn^{2+} + 2MnO_2 + 2e^- \tag{5.1}$$

with the oxidation state of manganese changing from Mn^{3+} to Mn^{4+}. However, as discussed in the Section 1.5.3, the mechanisms that may occur during the electrochemistry of ZMO are multiple. The article by Soundharrajan et al. [51] suggests that electrodeposition of manganese dioxide is an important process for electrochemistry in ZMS electrolyte. Actually, the weakening of the zinc-associated modes (P1 and P2) of the material could also be attributed to a covering of the film by electro-deposited manganese dioxide and not to the egress of zinc from the ZMO. Another possibility is that the two mechanisms may occur simultaneously. It should be remembered that the possible manganese dioxide electrodeposition reaction, which always occurs in the anodic region (oxidation), thus simultaneously with the zinc deintercalation, is:

$$Mn^{2+}_{(aq)} + 2H_2O \rightarrow MnOOH_{(s)} + 3H^+ + e^- \tag{5.2}$$

$$MnOOH_{(s)} \rightarrow MnO_{2(s)} + H^+ + e^- \tag{5.3}$$

with the manganese oxidizing from Mn^{2+} to Mn^{4+}.[33] The fact that manganese dioxide electrodeposition is involved is suggested by two experimental data: firstly, the PS curve current vs. time at +0.6 V in ZMS shows a current that does not go to zero, but settles to a positive value and remains constant, showing that a reaction is still going on; secondly, a CV on bare FTO in ZMS electrolyte results in electrodeposition (see the Section 5.4). To continue to test the material, check the reversibility of the electrochemical process, and try to figure out what the main mechanism was, two more PS tests were performed. The first (in Figure 5.9 spectrum c), again in ZMS electrolyte, was performed at 0 V to promote the reduction reaction (make the zinc re-intercalate and/or dissolve the electrodeposited MnO_2). As it can be seen from the Raman spectrum, the ZMO peaks reappear, although the shoulder associated with P3 still remains significantly more pronounced than that

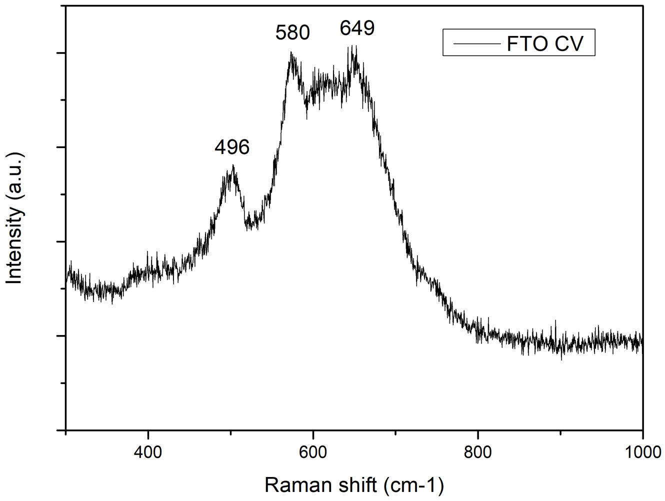

Figure 5.10: Raman spectra of electrodeposited MnO_x on bare FTO after CV in ZMS electrolyte. Excitation Laser: 532 nm.

of the pristine material. This latter effect may be due to either amorphization of the material or persistence of MnO_2 irreversibly deposited on the film.

Finally, the film was subjected to another oxidation step (+0.6 V, spectrum d in the Figure 5.9), but this time in ZS electrolyte, thus eliminating the possibility of manganese dioxide electrodeposition. In this case, the peaks associated with ZMO do not disappear, while the current rapidly drops to zero. The P3 shoulder increases slightly from the previous spectrum, still suggesting a modification of the material.

5.4. CV on bare substrate

Some electrochemical tests were performed on bare FTO-coated glass samples to evaluate the stability of the substrate and the electrodeposition effects of the electrolytes, so as to compare them with the CVs collected on ZMO films. The CVs conducted in different electrolytes (MS, ZMS, and ZS) are presented in Figure 5.11. The CV parameters are the same as those used for the ZMO films seen in Section 5.2. It can be seen in Figure 5.11a that the cycles in the MS electrolyte give rise to electrochemical activity showing one peak in the anodic region and two peaks in the cathodic zone. The electrodeposition of some form of MnO_x can also be seen by naked eye as the formation of an amber-colored film that reversibly, during cycling, deposits and dissolves. CVs using the ZMS electrolyte (Figure 5.11b) also exhibit one peak with a shoulder in the anodic region and two peaks in the cathodic zone, with electrodeposition and dissolution. Even in this case electrodeposition can be seen by naked eye and is confirmed by Raman spectroscopy, Figure 5.10. However, the peaks are centered at more positive potentials, have a different shape, and the currents involved are higher compared to the MS case. Finally, as expected, the sample that is cycled in ZS (Figure 5.11c) shows no electrochemical activity as there is no electrodeposition (no Mn^{2+}).

5.5. Data tentative interpretation

As we have seen, electrodeposition certainly plays a role in the electrochemistry of ZMO in ZMS electrolyte. For this reason, the absence of peaks in the Raman spectrum of ZMO in the film held at +0.6 V potential (see spectrum b in Figure 5.9) may be due only or partly to signal coverage by the electrodeposited manganese dioxide. At the same time, considering the CV due to electrodeposition alone on bare FTO in MS electrolyte (Figure 5.11a), it shows differences from both the CV on FTO in ZMS electrolyte (Figure 5.11b) and the CVs on ZMO deposited at various pressures (Figures 5.3, 5.4, and 5.5). This suggests that the electrochemistry of the material is not due to electrodeposition and dissolution of manganese dioxide alone, otherwise the CVs would all be much more similar. For this reason, I agree with the hypothesis put forward by Soundharrajan et al. [51] who argues, as schematized in the right part of Figure 5.12, that there are three active processes in ZMS electrolyte:

1. Insertion and extraction of Zn^{2+} in the ZMO film;
2. Electrodeposition and dissolution of MnO_2 from Mn^{2+} in the electrolyte;
3. Insertion of zinc into electrodeposited MnO_2.

This explains how CVs in ZMS differ from bare FTO and ZMO films, the latter being reactive beyond electrodeposition. It also explains the difference between CVs on bare FTO performed in ZMS and MS electrolytes, as the third mentioned mechanism can only occur in ZMS. Of course, further tests will be needed to verify that the hypothesis is correct and to understand which mechanism provides the largest contribution in the ZMO films produced by PLD. For example, techniques such as X-ray photoelectron spectroscopy (XPS), extended X-ray absorption fine structure spectroscopy (EXAFS), and Ion beam analysis (IBA) can reveal more information.

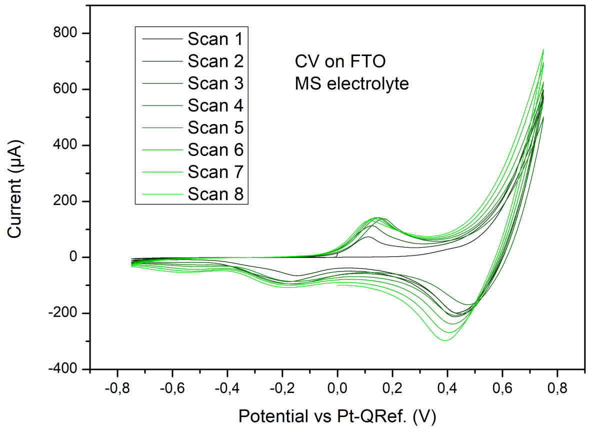

(a)

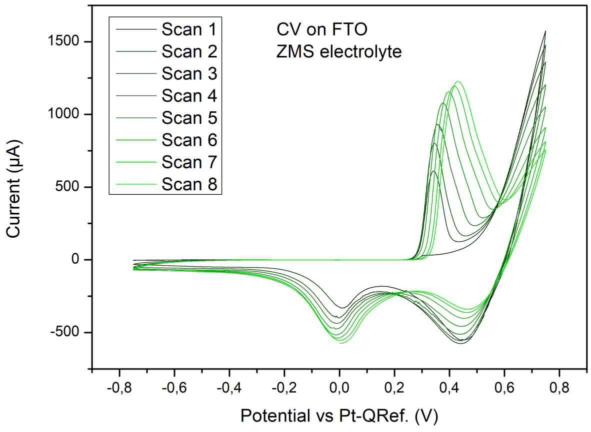

(b)

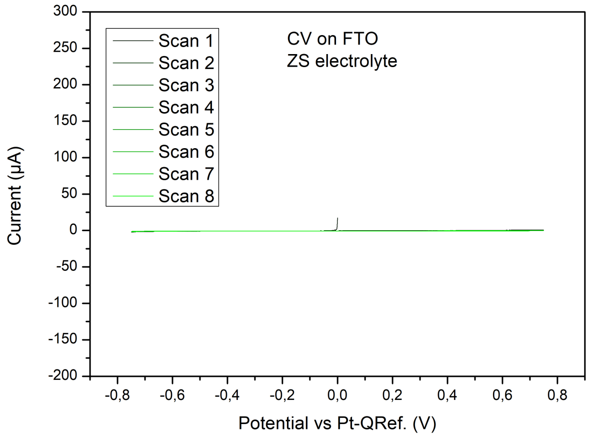

(c)

Figure 5.11: CVs on bare FTO-coated glass performed in different electrolytes: MS, ZMS, and ZS, respectively.

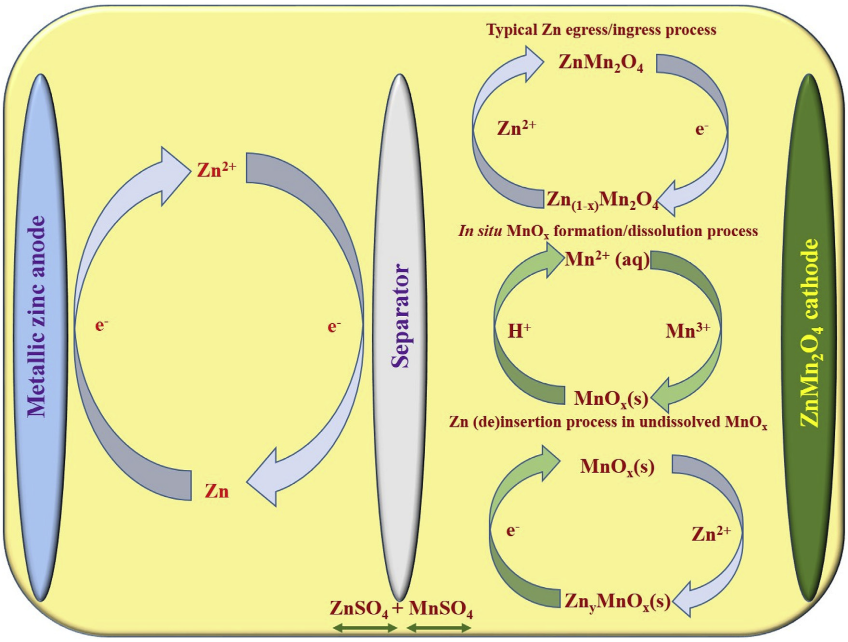

Figure 5.12: Electrochemical reactions inside $ZnMn_2O_4/Zn$ cell in ZMS electrolyte. Taken from [51].

Finally, it should be noted that in the last two spectra taken on the sample deposited at 100 Pa after the PS measurements, there is a peak at about 950 cm^{-1} and one immediately above 1000 cm^{-1} (too small to be visible in Figure 5.9). These peaks are characteristic of ZHS phase[80] (see Section 1.5.3)), a basic zinc sulphate that forms during discharge because of proton insertion in the material and consequent pH increase in the electrolyte. Indeed, SEM images of the sample deposited at 100 Pa after electrochemical tests (Figure 5.13) show scales similar to those presented in the article by Wu et al. [42] due to ZHS deposition. This suggests that the latter process, accompanied by proton insertion, also took place during the electrochemistry of my sample.

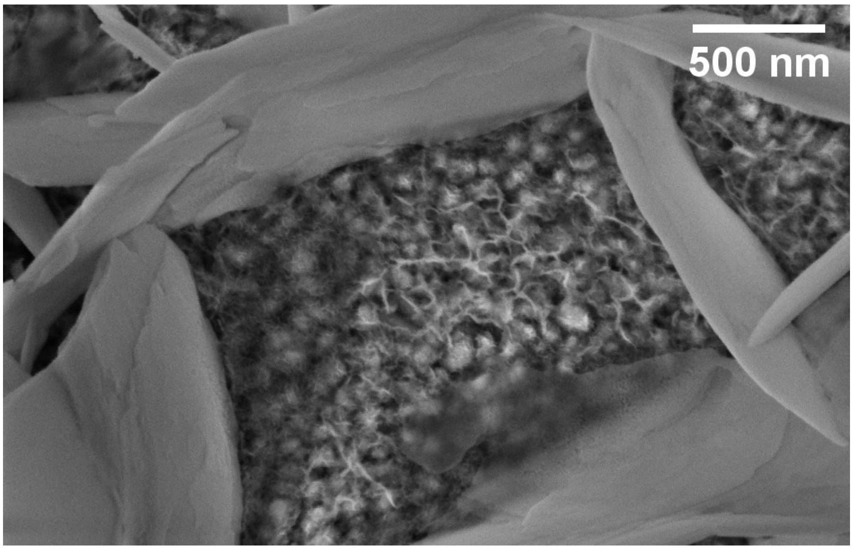

Figure 5.13: SEM image of the sample deposited at 100 Pa of oxygen and annealed at 500°C for 2 h after all the electrochemical tests. The ZHS flakes are visible.

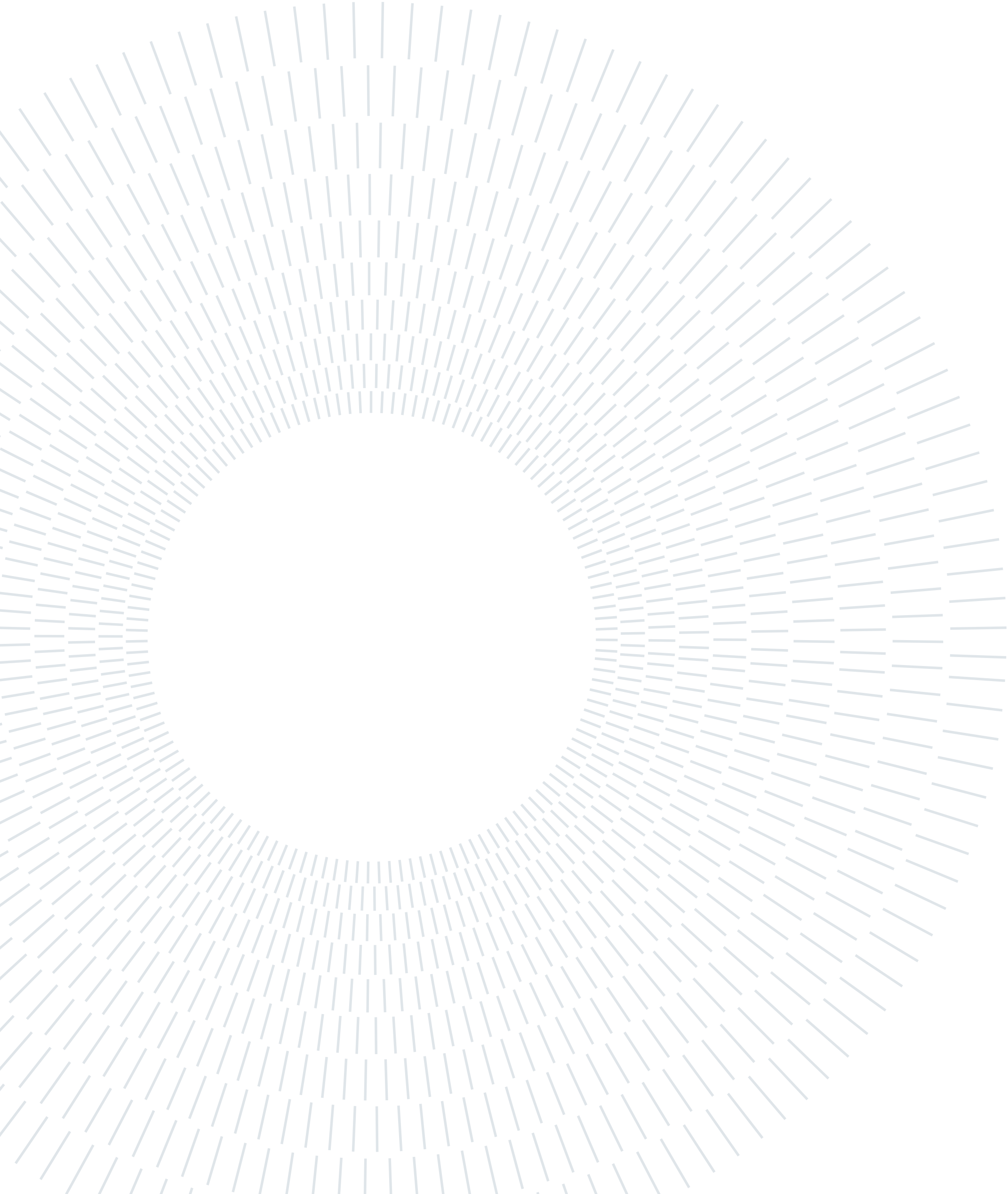

6 | Conclusions and future developments

This thesis has focused on the synthesis and characterization of ZMO thin films. This chapter highlights several achieved objectives and presents future developments and perspectives.

Firstly, the target used for PLD was analysed to understand its composition. ZMO thin films with thicknesses ranging from 250 nm to 3 μm were achieved by changing the deposition conditions and duration. It was shown how the fluence of the laser in PLD affects the deposition rate. Through PLD and the use of different gases, different pressures of the same gas, or vacuum deposition, it was shown how different morphologies and nanoporosities can be obtained, focusing particularly on films deposited in oxygen. I described how different oxygen pressures lead to different stoichiometries of the as-deposited films. In addition, through the use of Raman spectroscopy, it was shown that the deposited ZMO films are amorphous. The goal of this first part of the study was the optimization of PLD parameters to obtain a film with targeted characteristics.

The next step was to heat treat the films. Several tests were performed to optimize annealing conditions in order to crystallize the films and evaluate thermal compatibility with different substrates. It should be emphasized that I succeeded in obtaining crystalline ZMO films by annealing, both in air and in vacuum, and crystallization to the expected spinel phase was confirmed by Raman spectroscopy comparing to the literature's ZMO spectra.
A study of how different annealing temperatures affected the ZMO films was conducted, focusing particularly on annealing in air, confirming that higher annealing temperatures increase the crystalline grain size and improve the crystalline quality of the film.
I next studied how deposition in different oxygen pressures affected the crystallized samples (annealed under the same conditions) by evaluating their stoichiometry, morphology,

and Raman spectra. The analysed samples were deposited in vacuum and at different oxygen pressures (1 Pa, 10 Pa, 30 Pa, 50 Pa, 70 Pa, 100 Pa, and 150 Pa), finding marked differences between the behaviours of films deposited in vacuum and at 1 Pa compared to films deposited at higher oxygen pressures. The morphologies of the films deposited at low pressure tend, even after annealing, to be more compact, while the films deposited at high oxygen pressures (100, 150 Pa) show a crystalline nano-forest morphology. In particular, the latter morphology could be a favorable condition for the ZMO electrochemistry, owing to the large surface area available for electrode-electrolyte interaction and to the space suitable for accommodation of volume changes. By comparing the Raman spectra of samples deposited at different oxygen pressures, a hypothesis was advanced that the deposition pressure has a similar influence as the variation of the zinc content in the nominal manganite formula. Finally, the optical transmittance, absorbance, and reflectance of the samples were measured, and a basic optical characterization was carried out.

Electrochemical tests were initially successful, proving the effectiveness of the experimental setup and showing that the samples were electrochemically active in the expected potential ranges and remained mechanically intact and adhered to the substrate. CVs were acquired for samples deposited at different oxygen pressures and annealed in air at 500°C, showing different electrochemical behaviour from each other, thus confirming the influence of film morphology on performances. Potentiostatic tests were performed on the sample deposited at 100 Pa of oxygen, along with quasi-in-situ Raman measurements. The first information on the possible intercalation and deintercalation of zinc from the ZMO film emerged from Raman spectroscopy performed after each PS measurement. In addition, by running CVs over bare FTO-coated glass, it was verified that using the ZMS electrolyte (containing both Zn and Mn(II) sulphate), electrodeposition of manganese dioxide occurs. My hypothesis is that at least three mechanisms may occur simultaneously during electrochemical cycling on ZMO films: intercalation/deintercalation of Zn^{2+} in the ZMO films, electrodeposition of MnO_2, and insertion of Zn^{2+} into the electrodeposited MnO_2.

The future developments of this work may follow two main paths: 1) the further characterization and production of ZMO films with optimized morphology and composition, and 2) the comprehension of the electrochemical behaviour of the material through extensive electrochemical measurements. Additional perspectives for ZMO films are here listed.
As for short-term developments:

- films can be synthesized using different deposition gases and different gas mixtures, extending the work that was done in this thesis with some deposition tests in argon and argon-oxygen mixtures;

- the effects of vacuum deposition and vacuum annealing can be studied extensively. One can complete the series of vacuum annealing measurements by applying different vacuum annealing temperatures to the deposited samples at all the oxygen pressures discussed in this work;
- the stoichiometric composition of the film can be modified by adding zinc (so modifying the subscript x in the manganite formula $Zn_xMn_{3-x}O_4$) and trying to evaluate the effects of its direct variation on the Raman spectra like the study of Nádherný et al. [76]. Early trials in this field were carried out by adding some pieces of metallic zinc onto the target to increase its content in the film during co-deposition; however, the results were considered too immature to be included in this work;
- ZMO films for electrochemical purposes can be produced on platinum substrate deposited on silicon by PLD, further pursuing the work I have already started, and also, experimentally confirming its compatibility with electrochemical measurements;
- electrochemical measurements can certainly be expanded by testing CVs also on samples deposited at different oxygen pressures with respect to those seen in this work;
- the scan rate used for the CVs presented in this thesis was quite high since they were the very first tests, however, as mentioned in Section 2.5.1, lower scan rates certainly can improve the results. Thus, acquiring CVs with lower scan rates (1-10 mV/s) is certainly an interesting line of work, as well as the extensive test in different electrolytes;
- in-situ measurements could be performed by combining Raman spectroscopy with CV or PS measurements, thus monitoring in real time the material evolution during electrochemical polarization;
- complementary techniques, such as X-Ray Diffraction (XRD), X-ray photoelectron spectroscopy (XPS), and Fourier-transform infrared spectroscopy (FTIR), can be employed before and after electrochemical measurements;
- finally, analyses using other characterization techniques, such as extended X-ray absorption fine structure spectroscopy (EXAFS) and Ion beam analysis (IBA), can help to clarify the redox mechanisms in the samples.

Regarding long-term development, one of the final accomplishments of the study could be the realization of a complete zinc-ion cell (micro-battery) with a ZMO film as the cathode, a Zn metal anode, and an aqueous electrolyte. Eventually, this cell can be used to measure the fundamental battery parameters mentioned in Section 1.1, such as capacity, energy and power density, conversion efficiency, and calendar lifespan.

Concluding, even if a complete understanding of the subject has not been achieved, some critical results have been accomplished and this work can be considered as a starting point for both the further synthesis and characterization of the ZMO films by PLD and the ZMO films electrochemistry research.

Bibliography

[1] J. Garche. *Encyclopedia of Electrochemical Power Sources*, volume 6. 2009. ISBN 9780444527455.

[2] Qi Li, Yang Liu, Shaohua Guo, and Haoshen Zhou. Solar energy storage in the rechargeable batteries. *Nano Today*, 16:46–60, 2017. ISSN 1748-0132. doi: https://doi.org/10.1016/j.nantod.2017.08.007. URL `https://www.sciencedirect.com/science/article/pii/S1748013217302955`.

[3] Tedjani Mesbahi, Ahmed Ouari, Tarak Ghennam, El Madjid Berkouk, Nassim Rizoug, Nadhir Mesbahi, and Moudrik Meradji. A stand-alone wind power supply with a li-ion battery energy storage system. *Renewable and Sustainable Energy Reviews*, 40:204–213, 2014. ISSN 1364-0321. doi: https://doi.org/10.1016/j.rser.2014.07.180. URL `https://www.sciencedirect.com/science/article/pii/S1364032114006327`.

[4] M. Hosenuzzaman, N.A. Rahim, J. Selvaraj, M. Hasanuzzaman, A.B.M.A. Malek, and A. Nahar. Global prospects, progress, policies, and environmental impact of solar photovoltaic power generation. *Renewable and Sustainable Energy Reviews*, 41:284–297, 2015. ISSN 1364-0321. doi: https://doi.org/10.1016/j.rser.2014.08.046. URL `https://www.sciencedirect.com/science/article/pii/S1364032114007229`.

[5] Tarascon J-M. Larcher, D. Towards greener and more sustainable batteries for electrical energy storage. *Nature Chemistry*, 7(1):19 – 29, 2015. doi: 10.1038/nchem.2085.

[6] Niklas Borchers, Simon Clark, Birger Horstmann, Kaushik Jayasayee, Mari Juel, and Philippe Stevens. Innovative zinc-based batteries. *Journal of Power Sources*, 484, 2 2021. ISSN 03787753. doi: 10.1016/j.jpowsour.2020.229309.

[7] Xuming Yang and Andrey L. Rogach. Electrochemical techniques in battery research: A tutorial for nonelectrochemists. *Advanced Energy Materials*, 9, 7 2019. ISSN 16146840. doi: 10.1002/aenm.201900747.

[8] Stephan Leuthner. *Lithium-ion battery overview*. Springer Berlin Heidelberg, 8 2018. ISBN 9783662530719. doi: 10.1007/978-3-662-53071-9_2.

[9] M. Skyllas-Kazacos, C. Menictas, and T. Lim. 12 - redox flow batteries for medium- to large-scale energy storage. In Ziad Melhem, editor, *Electricity Transmission, Distribution and Storage Systems*, Woodhead Publishing Series in Energy, pages 398–441. Woodhead Publishing, 2013. ISBN 978-1-84569-784-6. doi: https://doi.org/10.1533/9780857097378.3.398. URL `https://www.sciencedirect.com/science/article/pii/B9781845697846500123`.

[10] Kai Christian Moeller. *Overview of battery systems.* Springer Berlin Heidelberg, 8 2018. ISBN 9783662530719. doi: 10.1007/978-3-662-53071-9_1.

[11] Arumugam Manthiram. An outlook on lithium ion battery technology. *ACS Central Science*, 3(10):1063–1069, Oct 2017. ISSN 2374-7943. doi: 10.1021/acscentsci.7b00288. URL `https://doi.org/10.1021/acscentsci.7b00288`.

[12] Daniele Di Lecce, Roberta Verrelli, and Jusef Hassoun. Lithium-ion batteries for sustainable energy storage: recent advances towards new cell configurations. *Green Chem.*, 19:3442–3467, 2017. doi: 10.1039/C7GC01328K. URL `http://dx.doi.org/10.1039/C7GC01328K`.

[13] Xin-Bing Cheng, Rui Zhang, Chen-Zi Zhao, and Qiang Zhang. Toward safe lithium metal anode in rechargeable batteries: A review. *Chemical Reviews*, 117(15):10403–10473, 2017. doi: 10.1021/acs.chemrev.7b00115. URL `https://doi.org/10.1021/acs.chemrev.7b00115`. PMID: 28753298.

[14] Fetzer J Klausner M Leuthner S, Kern R. Influence of automotive requirements on test methods for lithium-ion batteries, battery testing for electric mobility; berlin, germany. 2011.

[15] Prekshi Garg, Neha Srivastava, and Prachi Srivastava. Comparative investigation to analyse the critical role of nfe2l2 gene in heavy metal induced toxicity through in silico approaches. *Environmental Health Engineering and Management*, 9(1):33 – 40, 2022. doi: 10.34172/EHEM.2022.05.

[16] Cobalt toxicity in humans—a review of the potential sources and systemic health effects. *Toxicology*, 387:43–56, 2017. ISSN 0300-483X. doi: https://doi.org/10.1016/j.tox.2017.05.015.

[17] Christoph Vaalma, Daniel Buchholz, Marcel Weil, and Stefano Passerini. A cost and resource analysis of sodium-ion batteries. *Nature Reviews Materials*, 3(4):18013, Mar 2018. ISSN 2058-8437. doi: 10.1038/natrevmats.2018.13. URL `https://doi.org/10.1038/natrevmats.2018.13`.

[18] Y. Hou L. Liu-Y. Wu K. Loh ; H. Zhang K. Zhu W. Tang, Y. Zhu. Aqueous rechargeable lithium batteries as an energy storage system of superfast charging. *Energy Environ. Sci.*, 6:20932104, 2013.

[19] John B. Goodenough. Changing outlook for rechargeable batteries. *ACS Catalysis*, 7(2):1132–1135, Feb 2017. doi: 10.1021/acscatal.6b03110. URL `https://doi.org/10.1021/acscatal.6b03110`.

[20] Kan-Sheng Chen, Itamar Balla, Norman S. Luu, and Mark C. Hersam. Emerging opportunities for two-dimensional materials in lithium-ion batteries. *ACS Energy Letters*, 2(9):2026–2034, 2017. doi: 10.1021/acsenergylett.7b00476. URL `https://doi.org/10.1021/acsenergylett.7b00476`.

[21] S. Abada, G. Marlair, A. Lecocq, M. Petit, V. Sauvant-Moynot, and F. Huet. Safety focused modeling of lithium-ion batteries: A review. *Journal of Power Sources*, 306:178–192, 2016. ISSN 0378-7753. doi: https://doi.org/10.1016/j.jpowsour.2015.11.100. URL `https://www.sciencedirect.com/science/article/pii/S037877531530598X`.

[22] Xiaoxiao Jia, Chaofeng Liu, Zachary G. Neale, Jihui Yang, and Guozhong Cao. Active materials for aqueous zinc ion batteries: Synthesis, crystal structure, morphology, and electrochemistry. *Chemical Reviews*, 120:7795–7866, 8 2020. ISSN 15206890. doi: 10.1021/acs.chemrev.9b00628.

[23] Joyce A. Ober. Mineral commodity summaries 2018. Technical report, Reston, VA, 2018. URL `http://pubs.er.usgs.gov/publication/70194932`. Report.

[24] Chengjun Xu, Baohua Li, Hongda Du, and Feiyu Kang. Energetic zinc ion chemistry: The rechargeable zinc ion battery. *Angewandte Chemie International Edition*, 51 (4):933–935, 2012. doi: https://doi.org/10.1002/anie.201106307. URL `https://onlinelibrary.wiley.com/doi/abs/10.1002/anie.201106307`.

[25] Leyuan Zhang, Liang Chen, Xufeng Zhou, and Zhaoping Liu. Towards high-voltage aqueous metal-ion batteries beyond 1.5 v: The zinc/zinc hexacyanoferrate system. *Advanced Energy Materials*, 5(2):1400930, 2015. doi: https://doi.org/10.1002/aenm.201400930. URL `https://onlinelibrary.wiley.com/doi/abs/10.1002/aenm.201400930`.

[26] Xiaoyi Cai, Bao Yu Xia, Joseph Franklin, Baosheng Li, Xin Wang, Zhan Wang, Luwei Chen, Jianyi Lin, Linfei Lai, and Zexiang Shen. Free-standing vertically-aligned nitrogen-doped carbon nanotube arrays/graphene as air-breathing electrodes

for rechargeable zinc–air batteries. *J. Mater. Chem. A*, 5:2488–2495, 2017. doi: 10.1039/C6TA09615H. URL `http://dx.doi.org/10.1039/C6TA09615H`.

[27] Matthew Lim, Timothy Lambert, and Babu Chalamala. Rechargeable alkaline zinc–manganese oxide batteries for grid storage: Mechanisms, challenges and developments. *Materials Science and Engineering: R: Reports*, 143:100593, 01 2021. doi: 10.1016/j.mser.2020.100593.

[28] Ming Song, Hua Tan, Dongliang Chao, and Hong Jin Fan. Recent advances in zn-ion batteries. *Advanced Functional Materials*, 28, 10 2018. ISSN 16163028. doi: 10.1002/adfm.201802564.

[29] Lauren E. Blanc, Dipan Kundu, and Linda F. Nazar. Scientific challenges for the implementation of zn-ion batteries. *Joule*, 4:771–799, 4 2020. ISSN 25424351. doi: 10.1016/j.joule.2020.03.002.

[30] Hongfei Li, Longtao Ma, Cuiping Han, Zifeng Wang, Zhuoxin Liu, Zijie Tang, and Chunyi Zhi. Advanced rechargeable zinc-based batteries: Recent progress and future perspectives. *Nano Energy*, 62:550–587, 8 2019. ISSN 22112855. doi: 10.1016/j.nanoen.2019.05.059.

[31] Kexing Cai, Shao hua Luo, Jie Feng, Jiachen Wang, Yang Zhan, Qing Wang, Yahui Zhang, and Xin Liu. Recent advances on spinel zinc manganate cathode materials for zinc-ion batteries. *Chemical Record*, 22, 1 2022. ISSN 15280691. doi: 10.1002/tcr.202100169.

[32] Boeun Lee, Hae Ri Lee, Haesik Kim, Kyung Yoon Chung, Byung Won Cho, and Si Hyoung Oh. Elucidating the intercalation mechanism of zinc ions into -mno2 for rechargeable zinc batteries. *Chem. Commun.*, 51:9265–9268, 2015. doi: 10.1039/C5CC02585K. URL `http://dx.doi.org/10.1039/C5CC02585K`.

[33] Sa Heum Kim and Seung Mo Oh. Degradation mechanism of layered mno2 cathodes in zn/znso4/mno2 rechargeable cells. *Journal of Power Sources*, 72(2):150–158, 1998. ISSN 0378-7753. doi: https://doi.org/10.1016/S0378-7753(97)02703-1. URL `https://www.sciencedirect.com/science/article/pii/S0378775397027031`.

[34] Arjun Dhiman and Douglas G. Ivey. Electrodeposited manganese oxide on carbon paper for zinc-ion battery cathodes. *Batteries & Supercaps*, 3(3):293–305, 2020. doi: https://doi.org/10.1002/batt.201900150. URL `https://chemistry-europe.onlinelibrary.wiley.com/doi/abs/10.1002/batt.201900150`.

[35] Muhammad H. Alfaruqi, Vinod Mathew, Jihyeon Gim, Sungjin Kim, Jinju Song,

Joseph P. Baboo, Sun H. Choi, and Jaekook Kim. Electrochemically induced structural transformation in a γ-mno2 cathode of a high capacity zinc-ion battery system. *Chemistry of Materials*, 27(10):3609–3620, May 2015. ISSN 0897-4756. doi: 10.1021/cm504717p. URL `https://doi.org/10.1021/cm504717p`.

[36] Ning Zhang, Fangyi Cheng, Yongchang Liu, Qing Zhao, Kaixiang Lei, Chengcheng Chen, Xiaosong Liu, and Jun Chen. Cation-deficient spinel znmn2o4 cathode in zn(cf3so3)2 electrolyte for rechargeable aqueous zn-ion battery. *Journal of the American Chemical Society*, 138:12894–12901, 10 2016. ISSN 15205126. doi: 10.1021/jacs.6b05958.

[37] Dipan Kundu, Brian D. Adams, Victor Duffort, Shahrzad Hosseini Vajargah, and Linda F. Nazar. A high-capacity and long-life aqueous rechargeable zinc battery using a metal oxide intercalation cathode. *Nature Energy*, 1(10):16119, October 2016. doi: 10.1038/nenergy.2016.119.

[38] Singyuk Hou Chongyin Yang-Xiulin Fan Zhaohui Ma Tao Gao Fudong Han Renzong Hu Min Zhu Chunsheng Wang Wei Sun, Fei Wang. Zn/mno2 battery chemistry with h+ and zn2+ coinsertion. *Journal of the American Chemical Society*, 139(29): 9775–9778, Jul 2017. ISSN 0002-7863. doi: 10.1021/jacs.7b04471. URL `https://doi.org/10.1021/jacs.7b04471`.

[39] Yassine Beldjoudi Tae-woo Kwon Dong Jun Kim J. Fraser Stoddart Kwan Woo Nam, Heejin Kim. Redox-active phenanthrenequinone triangles in aqueous rechargeable zinc batteries. *Journal of the American Chemical Society*, 142(5):2541–2548, Feb 2020. ISSN 0002-7863. doi: 10.1021/jacs.9b12436.

[40] Huilin Pan, Yuyan Shao, Pengfei Yan, Yingwen Cheng, Kee Sung Han, Zimin Nie, Chongmin Wang, Jihui Yang, Xiaolin Li, Priyanka Bhattacharya, Karl T. Mueller, and Jun Liu. Reversible aqueous zinc/manganese oxide energy storage from conversion reactions. *Nature Energy*, 1, 2016. doi: 10.1038/nenergy.2016.39. URL `https://www.scopus.com/inward/record.uri?eid=2-s2.0-84988937159&doi=10.1038%2fnenergy.2016.39&partnerID=40&md5=5e67e005fb9d4c6b5e49a851781dd7db`.

[41] Guojin Liang, Funian Mo, Hongfei Li, Zijie Tang, Zhuoxin Liu, Donghong Wang, Qi Yang, Longtao Ma, and Chunyi Zhi. A universal principle to design reversible aqueous batteries based on deposition–dissolution mechanism. *Advanced Energy Materials*, 9(32):1901838, 2019. doi: https://doi.org/10.1002/aenm.201901838. URL `https://onlinelibrary.wiley.com/doi/abs/10.1002/aenm.201901838`.

[42] TzuHo Wu, ChihChen Huang, SinLin Cheng, and ChuenChang Lin. Expanded spinel

znxmn2o4 induced by electrochemical activation of glucose mediated manganese oxide for stable cycle performance in zinc ion batteries. *Journal of Colloid and Interface Science*, 617:274–283, 2022. ISSN 0021-9797. doi: https://doi.org/10.1016/j.jcis.2022.03.017. URL `https://www.sciencedirect.com/science/article/pii/S002197972200399X`.

[43] Krishnan Venkatesh, Balamurugan Muthukutty, Shen-Ming Chen, Chelladurai Karuppiah, Baishnisha Amanulla, Chun-Chen Yang, and Sayee Kannan Ramaraj. Nanomolar level detection of non-steroidal antiandrogen drug flutamide based on znmn2o4 nanoparticles decorated porous reduced graphene oxide nanocomposite electrode. *Journal of Hazardous Materials*, 405:124096, 2020. ISSN 0304-3894. doi: https://doi.org/10.1016/j.jhazmat.2020.124096. URL `https://www.sciencedirect.com/science/article/pii/S0304389420320860`.

[44] Lorenzo Malavasi, Pietro Galinetto, Maria C. Mozzati, Carlo B. Azzoni, and Giorgio Flor. Raman spectroscopy of amn2o4 (a= mn, mg and zn) spinels. *Phys. Chem. Chem. Phys.*, 4:3876–3880, 2002. doi: 10.1039/B203520K. URL `http://dx.doi.org/10.1039/B203520K`.

[45] Michael W. Lufaso and Patrick M. Woodward. Jahn–Teller distortions, cation ordering and octahedral tilting in perovskites. *Acta Crystallographica Section B*, 60 (1):10–20, Feb 2004. doi: 10.1107/S0108768103026661. URL `https://doi.org/10.1107/S0108768103026661`.

[46] Cheng Yang, Meina Han, Huihui Yan, Feng Li, Minjie Shi, and Liping Zhao. Insitu probing phase evolution and electrochemical mechanism of znmn2o4 nanoparticles anchored on porous carbon polyhedrons in high-performance aqueous zn-ion batteries. *Journal of Power Sources*, 452, 3 2020. ISSN 03787753. doi: 10.1016/j.jpowsour.2020.227826.

[47] James C. Knight, Soosairaj Therese, and Arumugam Manthiram. Chemical extraction of zn from znmn2o4-based spinels. *J. Mater. Chem. A*, 3:21077–21082, 2015. doi: 10.1039/C5TA06482A. URL `http://dx.doi.org/10.1039/C5TA06482A`.

[48] Lijing Yan, Xiaomin Zeng, Zeheng Li, Xiangjuan Meng, Di Wei, Tiefeng Liu, Min Ling, Zhan Lin, and Chengdu Liang. An innovation: Dendrite free quinone paired with znmn2o4 for zinc ion storage. *Materials Today Energy*, 13:323–330, 2019. ISSN 2468-6069. doi: https://doi.org/10.1016/j.mtener.2019.06.011. URL `https://www.sciencedirect.com/science/article/pii/S2468606919301340`.

[49] Zhifan Yao, Daoping Cai, Zhixiang Cui, Qianting Wang, and Hongbing Zhan.

Strongly coupled zinc manganate nanodots and graphene composite as an advanced cathode material for aqueous zinc ion batteries. *Ceramics International*, 46(8, Part A):11237–11245, 2020. ISSN 0272-8842. doi: https://doi.org/10.1016/j.ceramint.2020.01.148. URL `https://www.sciencedirect.com/science/article/pii/S0272884220301528`.

[50] Xianwen Wu, Yanhong Xiang, Qingjing Peng, Xiangsi Wu, Yehua Li, Fang Tang, Runci Song, Zhixiong Liu, Zeqiang He, and Xianming Wu. Green-low-cost rechargeable aqueous zinc-ion batteries using hollow porous spinel znmn2o4 as the cathode material. *J. Mater. Chem. A*, 5:17990–17997, 2017. doi: 10.1039/C7TA00100B. URL `http://dx.doi.org/10.1039/C7TA00100B`.

[51] Vaiyapuri Soundharrajan, Balaji Sambandam, Sungjin Kim, Saiful Islam, Jeonggeun Jo, Seokhun Kim, Vinod Mathew, Yang kook Sun, and Jaekook Kim. The dominant role of mn2+ additive on the electrochemical reaction in znmn2o4 cathode for aqueous zinc-ion batteries. *Energy Storage Materials*, 28:407–417, 6 2020. ISSN 24058297. doi: 10.1016/j.ensm.2019.12.021.

[52] Minjie Shi, Bei Wang, Yi Shen, Jintian Jiang, Wenhuan Zhu, Yanjie Su, Mugilan Narayanasamy, Subramania Angaiah, Chao Yan, and Qiang Peng. 3d assembly of mxene-stabilized spinel znmn2o4 for highly durable aqueous zinc-ion batteries. *Chemical Engineering Journal*, 399:125627, 2020. ISSN 1385-8947. doi: https://doi.org/10.1016/j.cej.2020.125627. URL `https://www.sciencedirect.com/science/article/pii/S1385894720317551`.

[53] Linlin Chen, Zhanhong Yang, Haigang Qin, Xiao Zeng, and Jinlei Meng. Advanced electrochemical performance of znmn2o4/n-doped graphene hybrid as cathode material for zinc ion battery. *Journal of Power Sources*, 425:162–169, 2019. ISSN 0378-7753. doi: https://doi.org/10.1016/j.jpowsour.2019.04.010. URL `https://www.sciencedirect.com/science/article/pii/S0378775319303945`.

[54] Shuting Wang, Shipeng Zhang, Xiangrui Chen, Guanghui Yuan, Beibei Wang, Jintao Bai, Hui Wang, and Gang Wang. Double–shell zinc manganate hollow microspheres embedded in carbon networks as cathode materials for high–performance aqueous zinc–ion batteries. *Journal of Colloid and Interface Science*, 580:528–539, 2020. ISSN 0021-9797. doi: https://doi.org/10.1016/j.jcis.2020.07.053. URL `https://www.sciencedirect.com/science/article/pii/S0021979720309310`.

[55] Haozhe Zhang, Jing Wang, Qiyu Liu, Wanyi He, Zhengzhe Lai, Xinyue Zhang, Minghao Yu, Yexiang Tong, and Xihong Lu. Extracting oxygen anions from

znmn2o4: Robust cathode for flexible all-solid-state zn-ion batteries. *Energy Storage Materials*, 21:154–161, 2019. ISSN 2405-8297. doi: https://doi.org/10.1016/j.ensm.2018.12.019. URL `https://www.sciencedirect.com/science/article/pii/S2405829718313527`.

[56] Linlin Chen, Zhanhong Yang, Haigang Qin, Xiao Zeng, Jinlei Meng, and Hongzhe Chen. Graphene-wrapped hollow znmn2o4 microspheres for high-performance cathode materials of aqueous zinc ion batteries. *Electrochimica Acta*, 317:155–163, 2019. ISSN 0013-4686. doi: https://doi.org/10.1016/j.electacta.2019.05.147. URL `https://www.sciencedirect.com/science/article/pii/S0013468619310801`.

[57] Saiful Islam, Muhammad Hilmy Alfaruqi, Dimas Yunianto Putro, Sohyun Park, Seokhun Kim, Seulgi Lee, Mohammad Shamsuddin Ahmed, Vinod Mathew, Yang-Kook Sun, Jang-Yeon Hwang, and Jaekook Kim. In situ oriented mn deficient znmn2o4@c nanoarchitecture for durable rechargeable aqueous zinc-ion batteries. *Advanced Science*, 8(4):2002636, 2021. doi: https://doi.org/10.1002/advs.202002636. URL `https://onlinelibrary.wiley.com/doi/abs/10.1002/advs.202002636`.

[58] Sinian Yang, Manshu Zhang, Xianwen Wu, Xiangsi Wu, Fanghong Zeng, Yuting Li, Shiye Duan, Dihua Fan, Yan Yang, and Xianming Wu. The excellent electrochemical performances of znmn2o4/mn2o3: The composite cathode material for potential aqueous zinc ion batteries. *Journal of Electroanalytical Chemistry*, 832:69–74, 2019. ISSN 1572-6657. doi: https://doi.org/10.1016/j.jelechem.2018.10.051. URL `https://www.sciencedirect.com/science/article/pii/S157266571830715X`.

[59] Yayuan Tao, Zhi Li, Linbin Tang, Xiaoming Pu, Tong Cao, Danhong Cheng, Qunjie Xu, Haimei Liu, YongGang Wang, and Yongyao Xia. Nickel and cobalt co-substituted spinel znmn2o4@n-rgo for increased capacity and stability as a cathode material for rechargeable aqueous zinc-ion battery. *Electrochimica Acta*, 331:135296, 2020. ISSN 0013-4686. doi: https://doi.org/10.1016/j.electacta.2019.135296. URL `https://www.sciencedirect.com/science/article/pii/S0013468619321681`.

[60] Xiaosha Cui, Yaxiong Zhang, Situo Cheng, Yupeng Liu, Zhipeng Shao, Zhenheng Sun, Yin Wu, Hongzhou Guo, Jiecai Fu, and Erqing Xie. Achieving high-rate and durable aqueous rechargeable zn-ion batteries by enhancing the successive electrochemical conversion reactions. *Journal of Colloid and Interface Science*, 620:127–134, 2022. ISSN 0021-9797. doi: https://doi.org/10.1016/j.jcis.2022.04.004. URL `https://www.sciencedirect.com/science/article/pii/S0021979722005513`.

[61] Megan B. Sassin, Maya E. Helms, Joseph F. Parker, Christopher N. Chervin, Ryan H.

Deblock, Jesse S. Ko, Debra R. Rolison, and Jeffrey W. Long. Elucidating zinc-ion battery mechanisms in freestanding carbon electrode architectures decorated with nanocrystalline znmn2o4. *Materials Advances*, 2:2730–2738, 4 2021. ISSN 26335409. doi: 10.1039/d1ma00159k.

[62] Christian M. Julien and Alain Mauger. Pulsed laser deposited films for microbatteries. *Coatings*, 9, 6 2019. ISSN 20796412. doi: 10.3390/COATINGS9060386.

[63] Simona Garattoni. Synthesis of titanium nitride thin films with tunable optical and electrical properties. Master's thesis, School of Industrial and Information Engineering, Politecnico di Milano, 2019.

[64] Angela De Bonis and Roberto Teghil. Ultra-short pulsed laser deposition of oxides, borides and carbides of transition elements. *Coatings*, 10(5), 2020. ISSN 2079-6412. doi: 10.3390/coatings10050501. URL `https://www.mdpi.com/2079-6412/10/5/501`.

[65] Cristina Mancarella. Development of plasmonic gold nanostructures with tunable optical and electrical properties. Master's thesis, School of Industrial and Information Engineering, Politecnico di Milano, 2019.

[66] A. Pazzaglia. Produzione e caratterizzazione di bersagli multistrato per l'accelerazione di ioni mediante laser superintensi. Master's thesis, School of Industrial and Information Engineering, Politecnico di Milano, 2015.

[67] Jeffrey B. Bindell. *SEM. Scanning Electron Microscopy.* Butterworth-Heinemann, 1992.

[68] Winson C.H. Kuo, Martha Briceno, and Dogan Ozkaya. Characterisation of catalysts using secondary and backscattered electron in-lens detectors. *Platinum Metals Review*, 58:106–110, 2014. ISSN 14710676. doi: 10.1595/147106714X680113.

[69] R. H. Geiss. *EDS. Energy-Dispersive X-Ray Spectroscopy.* Butterworth-Heinemann, 1992.

[70] Andrea Macrelli. Development of paper-based sers sensors for the detection of drugs. Master's thesis, School of Industrial and Information Engineering, Politecnico di Milano, 2019-2020.

[71] A. LiBassi. *X-ray and Light Scattering from Nanostructured Thin Films.* PhD thesis, University of Durham (UK), 2000.

[72] P. Bruesch. *Phonons: theory and experiments II*, chapter 3. Springer.

[73] Michael W. Swift, James W. Swift, and Yue Qi. Modeling the electrical double layer at solid-state electrochemical interfaces. *Nature Computational Science*, 1:212–220, 3 2021. ISSN 26628457. doi: 10.1038/s43588-021-00041-y.

[74] V. Russo, M. Ghidelli, P. Gondoni, C. S. Casari, and A. Li Bassi. Multi-wavelength raman scattering of nanostructured al-doped zinc oxide. *Journal of Applied Physics*, 115, 2 2014. ISSN 10897550. doi: 10.1063/1.4866322.

[75] Simone Bernardini, Fabio Bellatreccia, Annalaura Casanova Municchia, Giancarlo Della Ventura, and Armida Sodo. Raman spectra of natural manganese oxides. *Journal of Raman Spectroscopy*, 50(6):873–888, 2019. doi: https://doi.org/10.1002/jrs.5583. URL `https://analyticalsciencejournals.onlinelibrary.wiley.com/doi/abs/10.1002/jrs.5583`.

[76] Ladislav Nádherný, Miroslav Maryško, David Sedmidubský, and Christine Martin. Structural and magnetic properties of znxmn3-xo4 spinels. *Journal of Magnetism and Magnetic Materials*, 413:89–96, 9 2016. ISSN 03048853. doi: 10.1016/j.jmmm.2016.04.029.

[77] Qurat-ul-ain Javed, Fengping Wang, Arbab Mohammad Toufiq, M. Yasir Rafiq, M. Zubair Iqbal, and M. Arshad Kamran. Preparation, characterizations and optical property of single crystalline znmn2o4 nanoflowers via template-free hydrothermal synthesis. *Journal of Nanoscience and Nanotechnology*, 13(4), 2013.

[78] Mostafa Y. Nassar, Ehab A. Abdelrahman, Ahmed A. Aly, and Talaat Y. Mohamed. A facile synthesis of mordenite zeolite nanostructures for efficient bleaching of crude soybean oil and removal of methylene blue dye from aqueous media. *Journal of Molecular Liquids*, 248:302–313, 2017. ISSN 0167-7322. doi: https://doi.org/10.1016/j.molliq.2017.10.061. URL `https://www.sciencedirect.com/science/article/pii/S0167732217319852`.

[79] Juan Pablo Morán-Lázaro, Erwin Said Guillen-López, Florentino López-Urias, Emilio Muñoz-Sandoval, Oscar Blanco-Alonso, Héctor Guillén-Bonilla, Alex Guillén-Bonilla, Verónica María Rodríguez-Betancourtt, Marciano Sanchez-Tizapa, and María De la Luz Olvera-Amador. Synthesis of znmn2o4 nanoparticles by a microwave-assisted colloidal method and their evaluation as a gas sensor of propane and carbon monoxide. *Sensors*, 18(3), 2018. ISSN 1424-8220. doi: 10.3390/s18030701. URL `https://www.mdpi.com/1424-8220/18/3/701`.

[80] Jie Yang, Jianyun Cao, Yudong Peng, Wenji Yang, Suelen Barg, Zhu Liu, Ian A. Kinloch, Mark A. Bissett, and Robert A. W. Dryfe. Unravelling the mechanism

of rechargeable aqueous zn–mno2 batteries: Implementation of charging process by electrodeposition of mno2. *ChemSusChem*, 13(16):4103–4110, 2020. doi: https://doi.org/10.1002/cssc.202001216. URL `https://chemistry-europe.onlinelibrary.wiley.com/doi/abs/10.1002/cssc.202001216`.

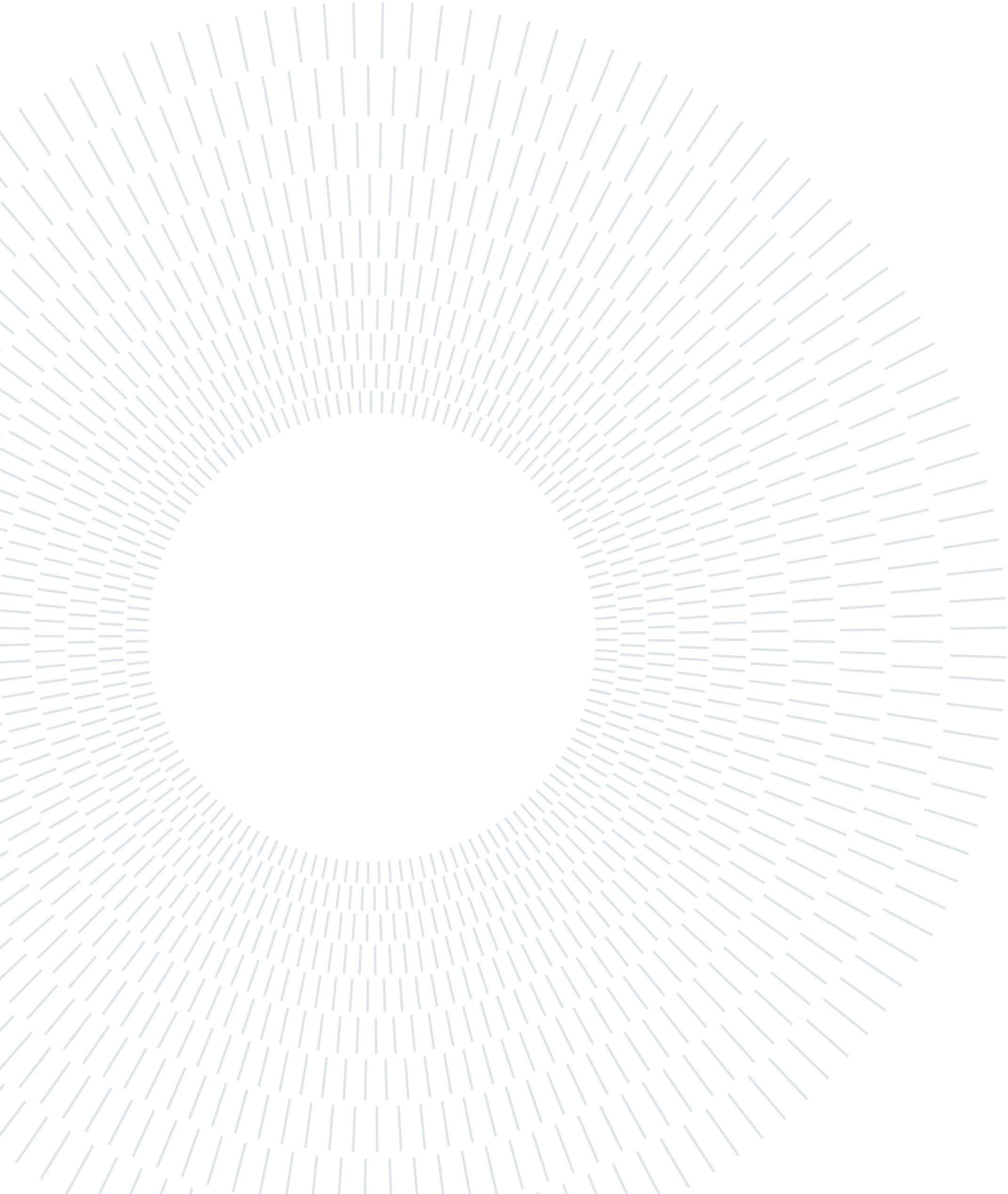

List of Figures

List of Tables

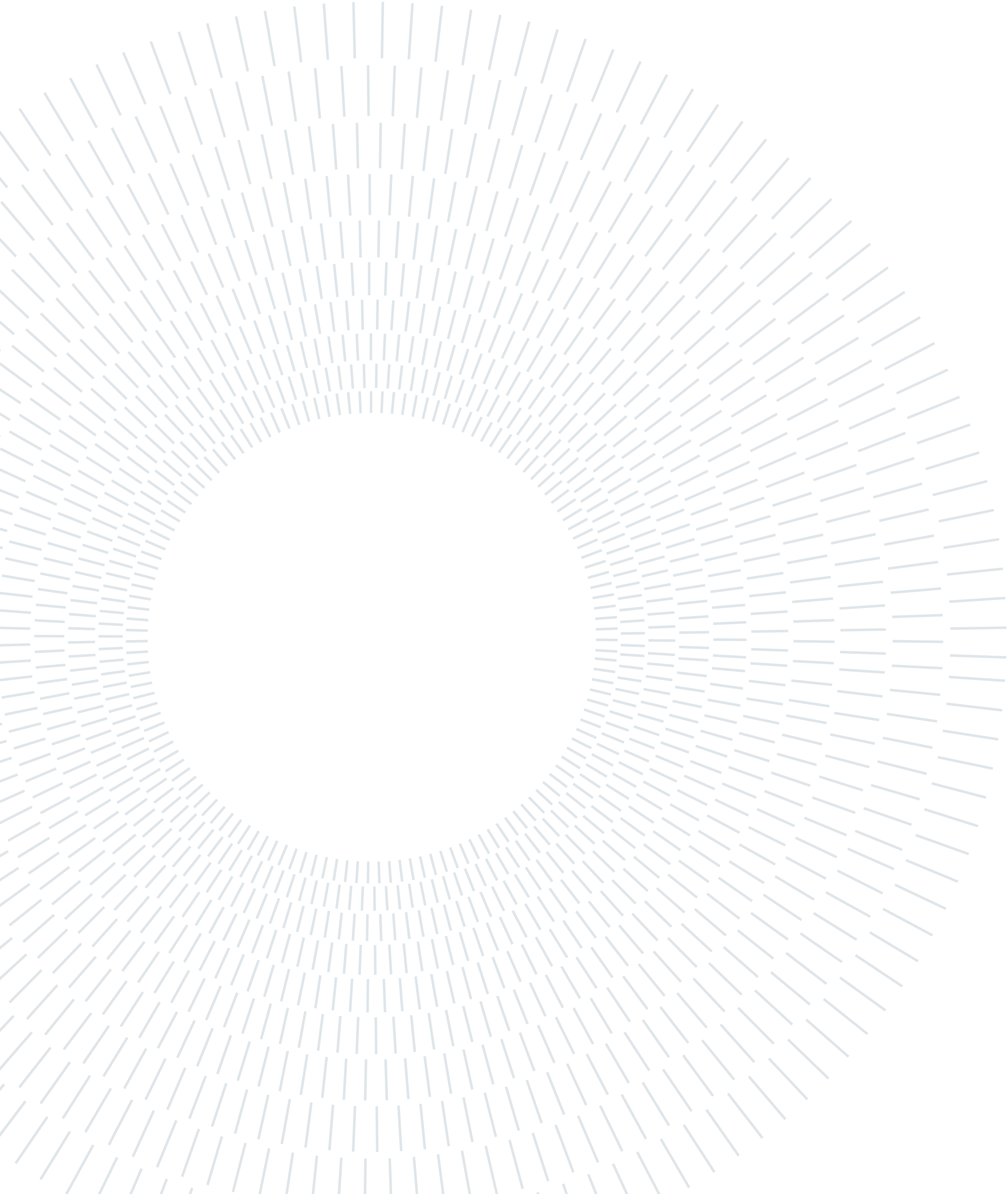

Acknowledgements

Innanzitutto, ci tengo a ringraziare coloro che mi hanno permesso di fare questa esperienza di tesi. Ringrazio il Professor Li Bassi, per la sua dedizione e precisione, per avermi seguito e consigliato in questi mesi durante il mio lavoro. Ringrazio il mio tutor Andrea Macrelli, grazie mille per avermi seguito passo passo insegnandomi moltissime cose, con infinita pazienza. Ringrazio il Professor Bozzini per l'aiuto che ci ha fornito nell'entrare nel mondo (per me nuovo) dell'elettrochimica. Ringrazio Lorenzo Bussetti, Claudia Filoni, Rossella Yivlialin, Marco Menegazzo e tutto lo staff del SoLINano per averci assistito nelle misure elettrochimiche. Infine, ringrazio tutti i membri del NanoLab per avermi accolto in questi mesi.

Ringrazio mia madre, Simona, e mio padre, Francesco, per avermi supportato in questi anni di studio, sia economicamente, ma soprattutto con affetto. Mamma e papà, grazie per avermi dato l'opportunità di crescere ed avermi aiutato a superare le difficoltà. E sì... grazie anche per avermi ascoltato ripetere milioni di volte delle formule per voi incomprensibili, con papà che prova sempre a capire e mamma che rinuncia in partenza.

Ringrazio le mie sorelle Cecilia e Chiara e mio fratello Tommaso, per avermi tranquillizzato prima di un esame, o avermi aiutato a tradurre qualcosa in inglese e, al di là dell'università, vi ringrazio per tutte le cose che abbiamo sempre condiviso e per aver da sempre riempito le mie giornate con la vostra presenza.

Ai miei nonni Gina, Rosi, Mario e Gennaro, che sono le mie radici. Grazie per avermi insegnato ad amare il mare, a ridere, per avermi tramandato l'amore per la scienza e l'importanza degli amici.

Ai miei migliori amici Luca e Mattia. Grazie per esserci stati sempre, anche nei momenti più pesanti, portando sempre con voi la vostra leggerezza e tenerezza. Grazie per ascoltarmi sempre, anche quando dico cose stupide. Il vostro sostegno mi ha permesso di fare una facoltà così impegnativa, sapendo che avevo sempre la vostra compagnia per staccare dalla serietà dal Politecnico.

Grazie ai miei amici di lunga data: Alessia, Andrea, Carlo, Ilaria, Lorenzo, Monica e Stefano. Abbiamo passato così tanto tempo insieme, che siete per me una seconda famiglia.

Ringrazio Adhara, Beatrice, Carola, Francesca, Silvia e Stefano anche con voi si avvicinano i dieci anni di amicizia, e per me questi traguardi sono i più importanti.
Ringrazio i miei compagni della triennale: Giovanni, Elena, Elisabetta, Jacopo, Matteo, Ruggiero e Silvia.
E Antonella e Silvia, che hanno condiviso con me il percorso della magistrale in nucleare.
Ringrazio la mia numerosa famiglia: le mie zie e i miei zii, Francesca, Paolo, Marina, Antonio, Laura e Dino, e i miei numerosissimi cugini.
Ringrazio i miei zii e cugini, anche se non di sangue, Silvia, Alberto, Stefano, Roberto e Davide.
Ringrazio infine la mia Prof, Daniela Di Vaio, per aver sempre creduto in me.

Ringrazio di cuore tutti voi, perché in fondo ognuno di voi, con i vostri insegnamenti e la vostra vicinanza, mi ha plasmato in ciò che sono ora. Questo momento quindi non è solo un obiettivo raggiunto da parte mia, ma è anche vostro. Grazie, un enorme abbraccio.